Abstract

The Shot Noise Thermometer

Lafe Frederick Spietz

2006

This thesis describes the development and testing of the shot noise thermometer, or SNT, a new kind of noise thermometer based on the combined thermal and shot noise of a tunnel junction in the non-superconducting state. In the shot noise thermometer, the noise power from a tunnel junction is measured as a function of the DC voltage across the junction, and the temperature is determined from the voltage dependence of the noise. This voltage dependence follows directly from the Fermi statistics of electrons in a metal, and is independent of the gain or noise temperature of the microwave amplifiers and detector used to measure the noise. Since the shot noise thermometer requires no calibration from an external temperature standard, it is a primary thermometer. In this thesis I demonstrate the operation of the shot noise thermometer over four orders of magnitude in temperature, from the base temperature of a dilution refrigerator to room temperature. Because of its wide range and the fact that it requires no outside calibration (it is a primary thermometer), the SNT is useful as a thermometer for general use in dilution refrigerators. In addition, the shot noise thermometer has sufficient accuracy to be useful as a potential temperature standard. This thesis discusses both of these applications as well as basic physics questions about the operation of the SNT and prospects for future development of the SNT technology.

The Shot Noise Thermometer

A Dissertation

Presented to the Faculty of the Graduate School

of

Yale University

in Candidacy for the Degree of

Doctor of Philosophy

by

Lafe Frederick Spietz

Dissertation Director: Professor Robert J. Schoelkopf

May 2006

Acknowledgements

There are far more people who deserve recognition here than there is room for in this section. I would first of all like to thank my parents for giving me such a strong start and teaching me how to learn. I would like to thank my early scientific mentors, in chronological order: Novera Spector, David Spector, Lynn Spietz, Richard Carstensen, Barry Olikola, Daniel Hoyt. Dan Hoyt deserves special thanks for providing excellent mentorship and for essentially teaching experimental physics at the graduate level during high school. My college research advisors, John McCuan and Alex Zettl also deserve special mention for guiding me on the path towards graduate research. I also would like to thank Tom Anglin and Jeanine Crutchfield for teaching me how to work. I thank Rob Schoelkopf, my thesis advisor, for literally taking me in off the street when I needed a job, and giving me the chance to do exciting research and be part of an awesome lab. Rob is an endless source of good ideas, a great mentor, and the best groundloop hunter I've ever even heard of. It has been a privilege to learn physics from him for the last six and a half years. I would also like to thank Michel Devoret for being an incredible mentor and source of great ideas during my time at Yale. I also thank Dan Prober both for his role as my teacher and committee member and for the leadership role he has played in building the fourth floor of Becton into the research powerhouse that it presently is, not to mention his role is encouraging me to come work at Yale when I first wandered in off the street. Two post docs who deserve special mention on the fourth floor are Irfan Siddiqi and Konrad Lehnert, both of whom served roles somewhere between older brothers and colleagues during grad school, and gave advice of use far beyond just science when I needed it most. I thank the excellent non-academic staff both on the fourth floor and in the various other offices and machine shops who make this whole place function smoothly, often going way above and beyond the call of duty to fight the rest of the bureaucracy to make things work. Also, I thank Wes Tew for providing useful metrological and thermometric knowledge, as well as extensive assistance in designing our high accuracy experiments. I would also like to thank all my awesome friends at Yale, in Berkeley,

and from around Connecticut and Alaska and the rest of the world who have provided inspiration and friendship. Finally, I thank Rachel, without whom this work would have been neither started nor finished.

Contents

List of Figures

List of Tables

List of Symbols and Abbreviations

A	Area
α	Normalized signal amplitude eV/hf, ratio of differential noise powers
B	Bandwidth
β	Nonlinearity constant
C	Capacitance
C_Σ	Sum Capacitance
CBT	Coulomb Blockade Thermometer
coth	Hyperbolic cotangent
d	Tunnel barrier thickness, thickness of capacitor
D^*	Diffusion constant
DC	Direct Current
D_n	Eigenvalues of the scattering matrix
$\Delta\phi$	Difference in work functions between a pair of metals
δ	Skin depth
e	The charge on the electron, $1.60217653(14) \times 10^{-19}$ C
E	Energy
e,f,g	Second fundamental form
E,F,G	First fundamental form
E_C	Charging Energy

ϵ_0	Electric constant
ϵ_{Ox}	Relative dielectric constant
f	Frequency (measured in Hz)
f(E)	Fermi function
F	Fano factor
FCC	Federal Communications Commission
Φ_0	Work function
$\bar{\phi}$	Average work function
G	Gain
G(V)	Conductance (measured in siemens)
GPIB	General Purpose Interface Bus
γ	Propagation constant
Γ	RF reflection coefficient
h	Plank's Constant
$\hbar$	Plank's Constant divided by 2π
HEMT	High Electron Mobility Transistor
I	Current
IETS	Inelastic Electron Tunneling Spectroscopy
ITS-90	International Temperature Scale of 1990
J_n	Nth Bessel function of the first kind
k_B	Boltzmann constant, $1.3806505(24) \times 10^{-23}$ J/K
κ	Thermal conductivity
k_1,k_2	Principal curvatures
$\mathcal{L}$	Lorenz number $\pi^2 k_B^2/3e^2$
λ	Resistance per unit length

λ_F	Fermi wavelength
m	Mass
MOS	Metal Oxide Semiconductor
N	Gauss map,number of points
N(x)	Arbitrary noise signal
NIST	National Institute of Standards and Technology
NRAO	National Radio Astronomy Observatory
OFHC	Oxygen Free High Conductivity
ω	Angular frequency (measured in radians per second)
P_L	RF Power delivered to a load
p(x)	Normalized noise
PLTS-2000	Provisional Low Temperature Scale of 2000
ppm	Parts per million
ppb	Pars per billion
r	Standard deviation of normalized Guassian voltage noise
$R_\square$	R square
R_K	Resistance quantum h/e^2
RIRT	Rhodium Iron Resistance Thermometer
S	Scattering matrix
S_I	Current spectral density (measured in A^2/Hz)
S_V	Voltage spectral density (measured in V^2/Hz)
SEM	Scanning Electron Microscope
SI	Systeme International
sinh	Hyperbolic sine
SNT	Shot Noise Thermometer

SPRT	Standard Platinum Resistance Thermometer
SQUID	Superconducting Quantum Interference Device
σ	Standard deviation, conductance per unit length of a tunnel barrier between two films, conductivity
t	Complex transmission coefficient, time, and dimensionless temperature fit parameter
T	Temperature
T_N	Noise Temperature
τ	Integration Time
V	Voltage
WKB	Wentzel-Kramers-Brillouin
x	Normalized voltage eV/k_BT, also position
x_1, x_2	Principal directions
χ^2	Chi squared function
Z	Impedance
$\Psi(x)$	Schrödinger wave function

Chapter 1

Introduction

1.1 General Thermometry

Temperature is an important quantity in every field of science and technology. The thermometry needs of scientists and engineers are as diverse as the fields they work in, but there are some figures of merit that are always desirable for thermometers. The ideal thermometer would be small, cheap, easy to use, accurate, fast, primary, and operate over a wide range in temperature. In practice, different applications will have differing demands from the above list, as well as differing levels of difficulty in achieving those characteristics.

A primary thermometer is one which relies on some physical law to determine temperature, independent of any external calibrations. A thermometer such as a thermistor in which the variable measured is compared to a lookup table from previously measured data to determine temperature is called a secondary thermometer. This distinction is important for several reasons. Secondary thermometers can be subject to drift, which may be undetectable. If a resistance thermometer drifts during the time between initial calibration and the present experiment, the experimenter will have no way to distinguish between a truly changed temperature and a calibration drift, without repeating the initial calibration measurement. A secondary thermometer can also be subject to changes with variables such as magnetic field or pressure which make calibration more complicated or impossible over a range of situations. Furthermore, a secondary thermometer always relies on a primary thermometer for its initial calibration. Without some kind of primary temperature measurement, there is nothing to connect the variable measured in a secondary thermometer with the real physical quantity of temperature.

The distinction between primary and secondary thermometers is particularly important in sit-

uations where calibration is difficult or when drift is severe due to the environment the sensor is in. The nuclear power industry is an example of a field in which secondary thermometry presents a serious problem. Sensors in nuclear power plants are subject to radiation which can change the calibration on short time scales, and which also makes replacement of sensors difficult and expensive. It is essential in this circumstance to have the ability to calibrate the thermometry in situ to minimize cost and down time. Low temperature physics measurements also benefit greatly from primary thermometry for similar reasons.

A further distinction can be made in the types of temperature measurements between thermodynamic temperature measurements and non-thermodynamic temperature measurements. A thermodynamic temperature measurement uses some fundamental thermodynamic law to determine temperature. Generally, this law comes directly from the statistical mechanics of the Maxwell-Boltzmann gas, the Bose gas, or the Fermi gas. Examples of thermodynamic thermometry include radiation thermometry, noise thermometry, and ideal gas thermometry. While secondary thermometers are never thermodynamic, it is also possible to have a primary thermometer which is not thermodynamic. The classic examples of this are the the platinum thermometer and the ^{3}He melting curve. As will become clear in the discussion below on temperature metrology, these thermometers are considered to be primary, although they are not related to temperature by any thermodynamic law. This is because they have been incorporated into the legal definition of temperature. Thus, they are only primary because people have chosen to make them so. Thermodynamic temperature measurement is always an essential component of temperature scales, and plays a fundamental role in all temperature measurement, as well as in the concept of what temperature means.

One final point about general thermometry worth making is the distinction between precision and accuracy. Precision is simply the number of digits to which a quantity may be repeatably measured. Accuracy is degree to which a measured quantity matches the correct value of the quantity being measured. For example, it is easy to measure the resistance of a resistance thermometer to six digits of precision with a typical multimeter while still only having only 10 % accuracy, limited by the calibration.

1.2 Cryogenic Thermometry

Thermometry becomes progressively more difficult as experiments get colder, particularly in the temperatures below 4 K, the boiling point of liquid helium. In this temperature range, all substances

other than helium are frozen solid, and many electronic devices either stop working altogether due to freezing out of carriers, or cease to be dependent on temperature and hence become useless as thermometers. At cryogenic temperatures, maintaining good thermal contact between a temperature sensor and the system being measured can also be challenging, since phonons are mostly frozen out and electronic thermal conductance of metals decreases with temperature. The needed dynamic range is also higher than in any other lab thermometry problem. A typical low temperature physics experiment might well involve testing devices at 300 K, then cooling down to below 30 mK, requiring thermometry capable of operating over more than four decades in temperature. Cryogenic systems generally use several different types of sensor to cover the different ranges, with the number and quality of alternatives dwindling rapidly as the lowest temperatures are approached.

The most common sensors in use in cryogenic apparatus are resistance thermometers. Resistance thermometers are simply devices whose resistance has some known dependence on temperature. In general, this resistance is not accurately predictable based on any physical law, and determination of temperature is based on some external calibration. The most widely used sensors in the range from room temperature to about 1 K are the rhodium iron and Cernox (a trademark of Lakeshore Cryotronics) resistance thermometers. These sensors are relatively cheap, and can be measured easily using a standard resistance bridge or even a multimeter. Over most of the range from 400 K down to 1 K, the Rhodium Iron sensor has a resistance that is close to linear in temperature, and it is extremely precise and repeatable. Because the Rhodium Iron is typically only a few ohms, it is possible to read out the resistance quickly. Another low impedance sensor that operates over a similar range is the Standard Platinum Resistance Thermometer (SPRT). While not as commonly used in low temperature measurements, the SPRT is an essential tool both in temperature metrology and in industry.

In the range below 1 K the most commonly used sensor is the ruthenium oxide resistance thermometer. This thermometer is based on a film which has an inverse exponential dependence on temperature. Ruthenium oxide sensors generally have tens of kΩ of resistance at a few kelvin and hundreds of kΩ of resistance at 10 mK, with maximum sensitivity at the lowest temperatures, and sensitivity which approaches zero at a few kelvin. The ruthenium oxide thermometer drifts over time, with the effect of the drift being maximal at the lowest temperatures. Also, in order to avoid self-heating, the voltages applied to the sensor must be extremely small, making the wiring challenging.

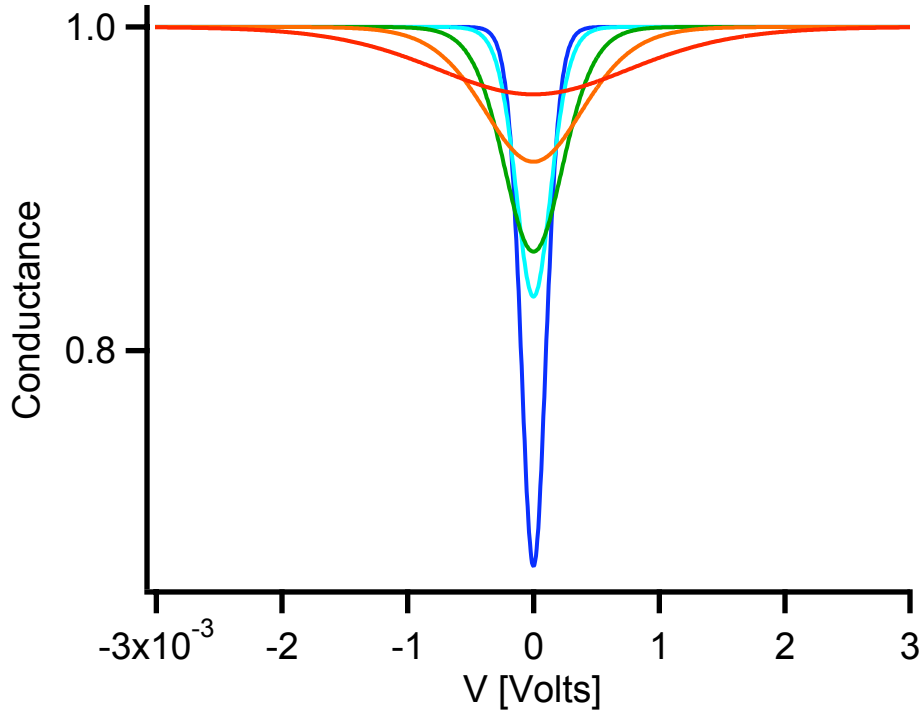

Figure 1.1: Illustration of Coulomb Blockade Thermometer conductance curves. The curves shown here are theoretical curves based on published CBT papers[53]. Different temperatures are represented by the colors of the rainbow, with blue indicating cold and red indicating hot. As temperature increases, the width of the peak increases linearly. The full width half maximum voltage $V_{1/2}$ satisfies the relation $eV_{1/2}/2k_BT = 5.439$.

In addition to the standard resistance thermometers that are typically installed in commercial cryogenic systems, there exist a variety of other cryogenic thermometers, some of which are available commercially and some of which are more experimental. These include the nuclear orientation thermometer, the Coulomb Blockade Thermometer (CBT), the helium-3 melting pressure thermometer, and Johnson noise thermometry.

The nuclear orientation thermometer is the most frequently used technology for calibrating commercial ruthenium oxide thermometers, and is used by companies that sell cryostats to demonstrate the base temperature of their systems at installation.

The Coulomb Blockade Thermometer is a primary electronic thermometer based on the Coulomb blockade of tunnel junctions at low temperatures [53, 36, 41]. In the CBT, the conductance of an array of high impedance tunnel junctions is measured as a function of voltage. This yields a peak the width of which relates temperature directly to voltage using only fundamental constants (see

Figure 1.1). The normalized conductance of the CBT is given as follows:

$$\frac{G(V)}{G(0)} = 1 - \frac{E_c}{k_B T} \frac{\frac{x}{2}\sinh\frac{x}{2} - 4\sinh^2\frac{x}{4}}{8\sinh^4\frac{x}{8}}, \tag{1.1}$$

where x is the normalized voltage eV/k_BT and E_c is the charging energy $e^2/2C_\Sigma$. The CBT is independent of magnetic field, and does not need to be re-calibrated since it is primary [54]. The CBT has been developed into a commercial product by Nanoway Oy, a Finnish company. The main difficulties of the CBT come from its range and the drift of the tunnel junctions. Although the CBT is primary in principle, its operation depends on the junctions in the array being of equal resistance. As the devices age, the resistances of the junctions age differently from each other, which leads to errors. This limits the ultimate accuracy of the CBT. Also, the charging energy of the CBT corresponds to a characteristic temperature, above which the sensitivity drops off to zero. A set of different CBT sensors is required to cover the range from 25 mK to a few kelvin, and between room temperature and a few kelvin the CBT may be used as a secondary thermometer based on the temperature dependence of the conductance of tunnel junctions. Finally, because the entire junction array is subject to heating, and because the hot electrons must diffuse out through the array to equilibrate with the leads, there is a temperature profile in the junction array which is less uniform at the lower temperatures [37]. This temperature profile eventually leads to a saturation of the measurable temperature at around 25 mK. Since many commercially available dilution refrigerators in common use today have base temperatures as low as 10 mK, the CBT range does not cover the whole useful temperature range.

The helium-3 melting pressure thermometer operates over the range from about 1 mK to 1 K. It is based on measuring the melting pressure of a cell filled with helium-3, typically a few tens of atmospheres. The curve that describes the pressure of the phase change of helium-3 as a function of temperature is highly repeatable, and this is another example of a thermometer that is primary but not thermodynamic (because it is part of an international temperature scale). The melting pressure thermometer can be quite accurate, but in addition to its limited range it requires a significant amount of gas handling hardware to operate, and as of the writing of this thesis has not been incorporated into any commercial product. Figure 1.4 shows a melting pressure curve. Note that this curve is non-monotonic, and that the pressures involved are over 30 atmospheres. These two facts add to the practical challenge of melting pressure thermometry.

Finally, Johnson noise thermometry is a method that is extremely useful in temperature metrol-

ogy and certain specialized experiments, although it is traditionally not used as a practical thermometer. In noise thermometry, the electrical noise of a linear resistor is measured, from which the temperature may be calculated. This is a thermodynamic temperature measurement, and hence is extremely useful in relating practical temperature scales to thermodynamic temperature. Johnson noise thermometry has been demonstrated from below 1 mK to over 1000 K. As I will discuss in greater detail below, Johnson noise thermometry is extremely useful, but is made technically difficult by the small signals involved. These small signals force the experimenter to use very high gain amplifiers, which must be calibrated to the level of accuracy of the temperature measurement. This is only possible if the bandwidth of the amplifiers is limited to audio frequencies, which inhibits the speed with which temperature may be measured. Several schemes have been devised to overcome the difficulties of Johnson noise thermometry, but none have brought the method to the point where it can be used as a practical thermometer for general use at low temperatures. The Shot Noise Thermometer brings noise thermometry within reach as a practical thermometry method.

1.3 Temperature Metrology

Metrology is the science of measurement, and is concerned with the setting of international standards for units and constants. These standards are maintained by national metrology labs run by governments around the world, and are agreed upon by international treaty. The highest level of standard is the Systeme International (SI), which sets official definitions for the physical units. In temperature, there are two levels of standard: the SI kelvin and the international standards known as the International Temperature Scale of 1990 (ITS-90) [57, 28] and the Provisional Low Temperature Scale of 2000 (PLTS 2000) [65].

The SI kelvin is defined as 1/273.16 of the triple point of water. The triple point of water is the temperature at which water can simultaneously exist in the gas, liquid and solid states (see Figure 1.2). As long as the correct isotope content of pure water is used and the triple point cell is constructed correctly, the triple point of water provides a fixed temperature that is repeatable to a fraction of a part per million. These cells are commercially available, and are straightforward to use.

This unit is different from some of the other SI units in that it gives no information on how to find temperature, other than at exactly 273.16 K. If one measures time using a cesium atomic clock, one knows the time in SI seconds, but there is no specification in the SI kelvin on how to

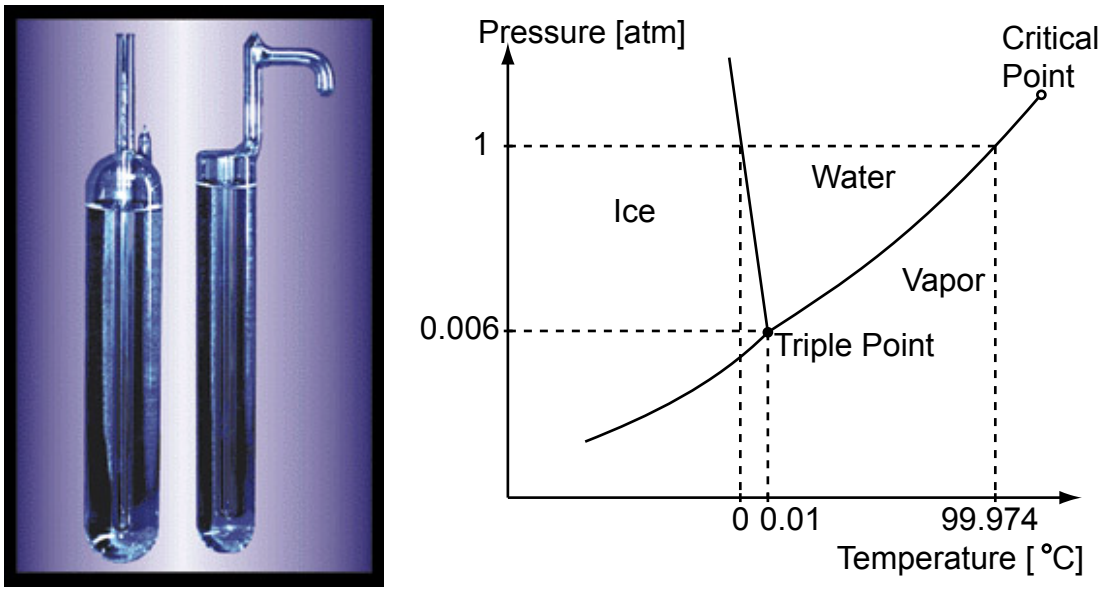

Figure 1.2: Left inset shows a photograph of a commercial water triple point cell from Pond Engineering. Right inset shows the phase diagram of water (not to scale).

find the SI temperature at, for instance, 4 K. To fill this gap, the ITS-90 and PLTS 2000 provide a set of fixed points and thermometry methods that together make up an international standard for the kelvin. This is clearly a weakness in the definition of the kelvin. By fixing the speed of light, metrologists have made a very simple definition of the meter based on the second. Similarly, if the proposals to fix either Plank's constant or Avogadro's number are carried out, the kilogram could be defined in a straightforward way from other units [43]. An ideal for the future of temperature metrology would be to similarly fix Boltzmann's constant and define the SI kelvin from energy. The shot noise thermometer provides a potential path for such a redefinition of the SI kelvin by relating temperature to voltage, as does the Josephson voltage noise source presently being developed at NIST [6, 5, 44, 46, 45].

In the present system, however, determination of temperatures other than the triple point of water is done by use of the ITS-90 and PLTS-2000 scales. ITS-90 is a scale that covers the range from 0.65 K to well over 1000 K, and is a mixture of different thermometry methods and fixed points (see Figure 1.3). In the range from 0.65 K to 5.0 K, the vapor pressure of helium is used to partially define the standard. Overlapping that, from 3.0 K to the triple point of neon 24.5561 K is the constant volume gas thermometer, based on the ideal gas law $PV = Nk_BT$. In the range from

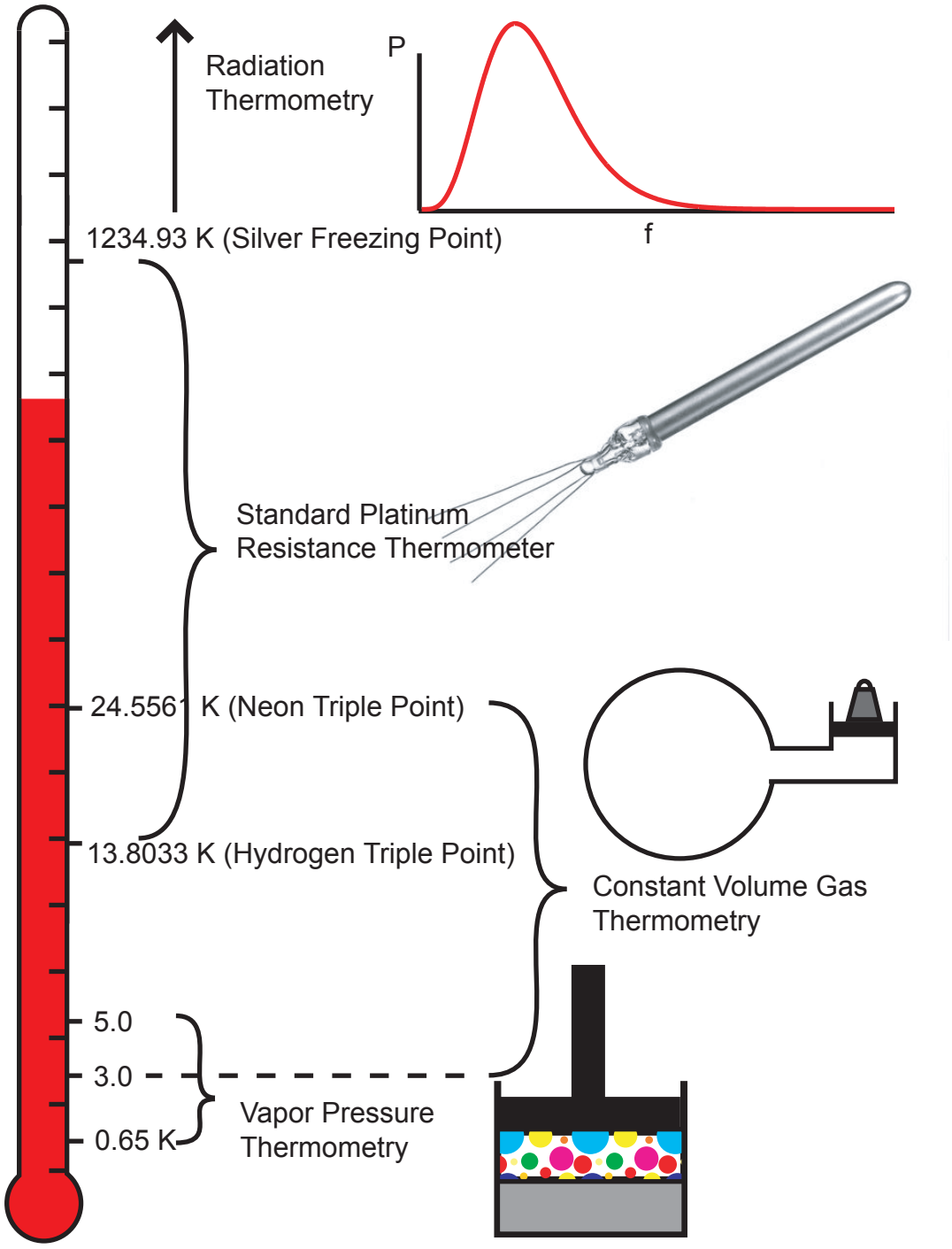

Figure 1.3: Cartoon showing the different types of thermometry used over different temperature ranges in the ITS-90 (not to scale). Above the freezing point of silver, radiation thermometry is used. From that point down to the triple point of hydrogen, the platinum resistance thermometer is used, which overlaps the constant volume gas thermometer, which in turn overlaps the vapor pressure thermometer which goes to the low end of the scale, 0.65 K.

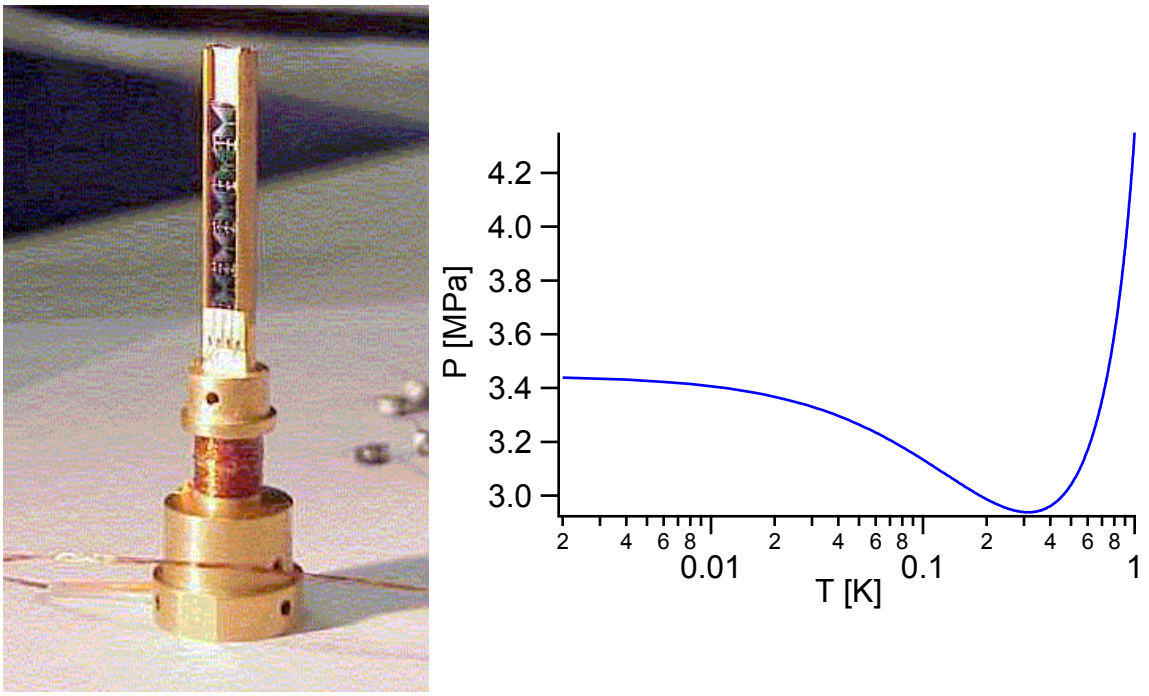

Figure 1.4: Elements of the PLTS 2000. the left inset shows a set of superconding fixed points. The right inset shows the melting curve of helium-3. Note that there is a point of zero sensitivity at about 0.3 K, and that the sensitivity also approaches zero at low temperatures.

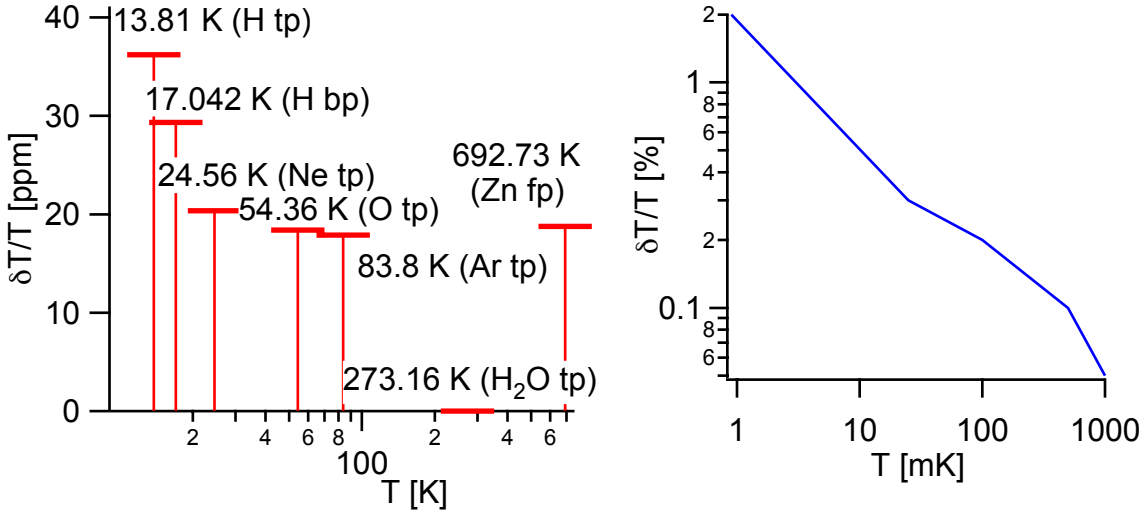

Figure 1.5: Thermodynamic uncertainties of the ITS 90 and PLTS 2000. The left inset shows the uncertainties of some selected fixed points in the ITS 90 and the right shows the overall thermodynamic uncertainty in the PLTS 2000 scale.

the triple point of hydrogen, 13.8033 K, to the freezing point of silver, 1234.93 K, the standard is the Standard Platinum Resistance Thermometer (SPRT). The PLTS-2000 is a scale that covers 0.9 mK to 1 K, and is based on the helium-3 melting pressure curve and superconducting fixed points.

It is important to remember that both of these scales define temperature that is distinct both from the SI kelvin and from thermodynamic temperature. The various fixed points and thermometers in these scales have a finite uncertainty in thermodynamic temperature. These uncertainties (see Figure 1.5) provide a goal for the would-be temperature metrologist to try to surpass in order to improve on the present scales.

1.4 Noise Thermometry

Any linear resistor in thermal equilibrium generates electrical noise that is proportional to temperature. For a resistor R and temperature T, the current spectral density of the noise is

$$S_I = \frac{4k_B T}{R}, \tag{1.2}$$

where k_B is Boltzmann's constant. Johnson noise thermometry consists of measuring the noise power from a resistor, and computing the temperature from the above equation. R may be determined to

the part per million level relatively easily, so the uncertainty of the measurement is dominated by the uncertainty with which S_I is determined.

Because typical noise voltages are so small, high gain amplifiers must be used to get a signal that is measurable by a square law detector or digitizer. These amplifiers will always have a finite bandwidth, and some kind of frequency dependent gain. They also will always add some noise to the measurement. Characterizing the gain by the function G(f) and the noise by the noise temperature function $T_N(f)$, one can write the measured noise power P as

$$P = \int G(f)[T + T_N(f)]df, \tag{1.3}$$

where the sensor resistance and Boltzmann's constant have been absorbed into the gain function. By integrating the added system noise temperature T_N over frequency and separating a single gain G, which absorbs the single bandwidth B, the above equation may be rewritten as

$$P = G(T + T_N). \tag{1.4}$$

For a noise measurement of this type, the statistical uncertainty in the measured power P is determined by the Dicke radiometer formula [18] as follows:

$$\frac{\sigma_P}{P} = \frac{1}{\sqrt{B\tau}}, \tag{1.5}$$

where τ is the integration time of the measurement. Furthermore, the fractional statistical uncertainty in the *temperature* measurement may be written as

$$\frac{\sigma_T}{T} = \frac{T + T_N}{T\sqrt{B\tau}}. \tag{1.6}$$

Note that as the noise temperature T_N becomes large compared to the physical temperature, that the fractional uncertainty goes up, and that the required integration time goes up with the square of noise temperature. Also, the smaller the bandwidth of the measurement, the longer the experimenter must wait to get a given statistical uncertainty. Because the difficulty of knowing accurately the gain and noise of an amplifier increases with frequency, traditional Johnson noise measurements are limited in the bandwidths they can use, and generally do not have a higher bandwidth than about 100 kHz. Johnson noise measurements must also compensate for drifts in the parameters of the amplifiers. The last three quarters of a century of development of noise thermometry since Johnson and Nyquist first described the phenomenon has largely consisted of devising creative ways to mitigate these problems.

One such scheme is to use the resistively shunted SQUID, or R-SQUID to relate noise power to frequency, thus removing the need for high accuracy knowledge of the amplifier gain [35, 59]. Another is the work presently in progress to calibrate the amplifiers in a noise measurement using a standard noise source of known power spectral density based on an AC Josephson standard voltage source. This method has recently yielded promising results in the 100 part per million range of accuracy, and could possibly be improved significantly from that.

The traditional way of removing amplifier drifts is the noise correlator, which is a circuit that switches between a sensor at a known temperature and the sensor at the temperature being measured and correlates the noise.

Taken together, the body of noise thermometry work presents an extremely impressive combination of range, accuracy and versatility. What is missing from the existing work, however, is a system that is easy enough to use that it could serve as a practical thermometer for non-metrologists. There also exists no noise thermometer with more than 100 part per million absolute accuracy. The work described in this thesis is both a more practical thermometer for general use than previous noise thermometers and admits the possibility of very high accuracy noise thermometry.

1.5 The Shot Noise Thermometer

The shot noise thermometer [72] uses the voltage dependence of the noise from a tunnel junction to relate temperature to DC voltage. In order to understand the functioning of the SNT it is necessary to discus the physics of current and noise in tunnel junctions.

All tunnel junctions in this thesis are assumed to be in the non-superconducting state. Such a tunnel junction can be modeled as a pair of ideal Fermi reservoirs separated by a tall, thin energy barrier (see Figure 1.6). The tunneling rate from a given energy level in one metal into the other metal can be evaluated by Fermi's golden rule. The tunneling rates are given by

$$\Gamma_{r\rightarrow l(l\rightarrow r)} = \frac{2\pi}{\hbar}\int |\langle l|M(E)|r\rangle|^2 D^2(E) f_{r(l)}(E)[1-f_{l(r)}(E)]dE, \tag{1.7}$$

where $\langle l|M(E)|r\rangle$ is the tunneling matrix element from the left to the right side of the junction, D(E) is the density of states, and $f_l(E)$ and $f_r(E)$ are Fermi functions used to count the empty and filled states on the left and right reservoirs, respectively. For a sufficiently tall, thin barrier, the tunneling amplitude and the density of states near the Fermi energy can be considered to be independent of energy. The occupation probability of any given state in one of the metals is given

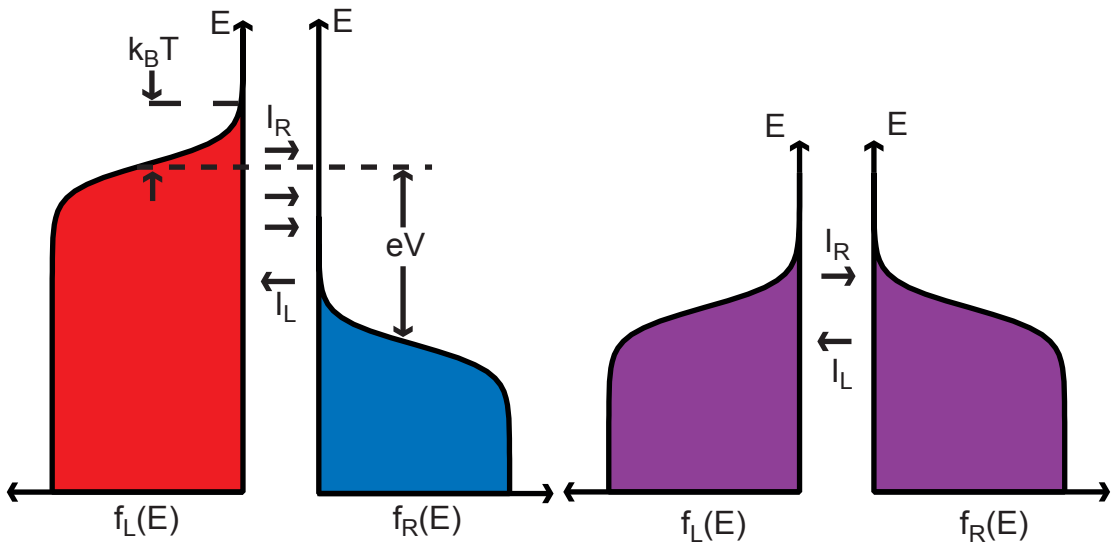

Figure 1.6: The left inset shows Fermi functions for a junction with finite bias applied, and the right inset shows the Fermi functions for a juntion in equilibrium.

by a Fermi function. Thus, under the conditions that $[eV_{bias,k_BT}] << E_{barrier}$, all the terms can be moved outside of the integral except the Fermi functions. the current through the junction can be found by taking the difference of these two rates to get

$$I = I_r - I_l = \frac{2\pi e}{\hbar}|\langle l|M(E_F)|r\rangle|^2 D(E_F)^2 \int [f_r(E) - f_l(E)]dE = V/R. \tag{1.8}$$

In other words, under these conditions, the junction is just an ohmic resistor with no temperature dependence.

To find the current spectral density of the noise, the sum instead of the difference of the rates is computed. Evaluation of the integral gives the result [58, 62]

$$S_I(V) = \frac{2}{R}\int \{f_r(E)[1 - f_l(E)] + f_l(E)[1 - f_r(E)]\}dE = \frac{2eV}{R}\coth\left(\frac{eV}{2k_BT}\right) = 2eI\coth\left(\frac{eV}{2k_BT}\right). \tag{1.9}$$

Unlike the current, this expression has a temperature-dependent scale that follows directly from the Fermi-Dirac distribution. A derivation that shows how to evaluate the above integral is given in an appendix to this thesis. Evaluating Equation 1.8 at zero voltage bias yields the Johnson noise result $S_I = 4k_BT/R$, as required by the fluctuation-dissipation theorem, whereas in the limit $eV >> k_BT$ equation 1.8 reduces to $S_I = 2eI$, the standard shot noise result (see Figure 1.7). This expression can be seen as analogous to the ideal gas law of gasses described by Maxwell-Boltzmann statistics.

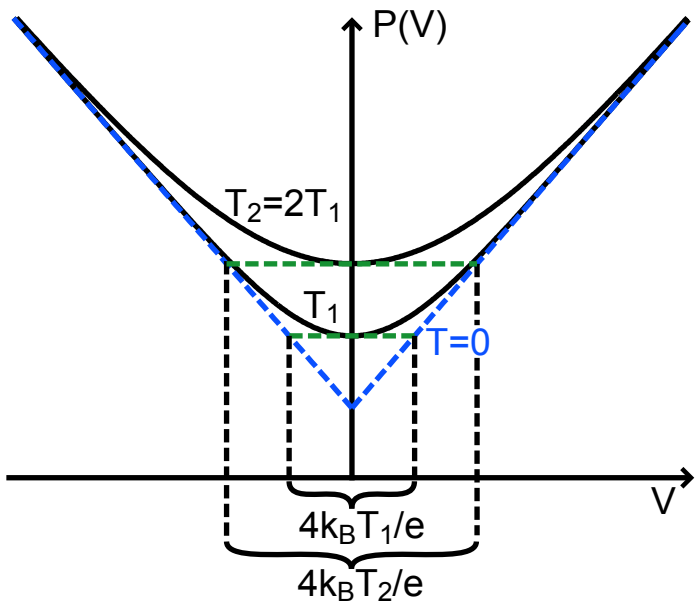

Figure 1.7: Theoretical plots of the noise from a tunnel junction as a function of voltage for two different temperatures. The green dotted line indicates the Johnson noise level at each temperature, and the blue dotted line indicates the shot noise limit at zero temperature, which the other curves approach asymptotically for large voltage. The temperature is determined from the width of the curves as shown.

Thus the SNT may be seen as a sort of "ideal electron gas thermometer", with Maxwell-Boltzmann statistics replaced by Fermi statistics.

By measuring the noise as a function of voltage, the temperature can be determined from the voltage scaling of this transition independent of the gain or noise of the amplifier chain and detector. This frees the SNT from the major limitation of traditional Johnson noise thermometry: the need to calibrate gain, noise temperature and bandwidth to high accuracy. The elimination of the need for absolute accuracy in the amplifier chain calibrations allows much more freedom in the selection of components. In particular, the kHz bandwidth amplifiers typically used in noise thermometry experiments may be replaced by microwave amplifiers with hundreds of MHz of bandwidth, allowing for a much faster readout.

For the tunnel junction, equation 1.3 may be re-written as

$$P(V,T) = G\left[T_N + \frac{eV}{2k_B}\coth\left(\frac{eV}{2k_BT}\right)\right]. \tag{1.10}$$

Noise power data as a function of voltage can be fit to this expression, with the temperature T, the noise temperature T_N, and the gain G as fit parameters. This method yields a value for temperature

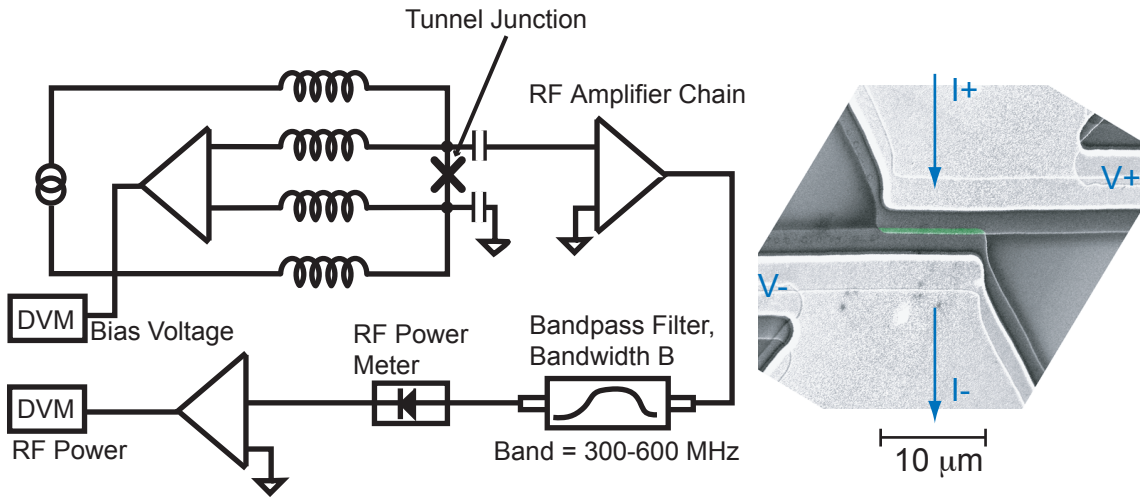

Figure 1.8: Schematic diagram of SNT layout. All DC leads are inductively coupled, and both the RF signal line and RF ground are capacitively coupled. Right inset shows an scanning electron micrograph of a typical SNT junction. The green highlighted section is the junction itself, and the brightest areas are where a thick copper layer covers the two aluminum layers. The blue arrows indicate how DC current flows.

that is independent of the value and frequency dependence of the noise and gain of the amplifier. Any effect such as finite coupling of radio frequency signal power into the amplifier chain or attenuation of cables leaves the fit temperature unchanged unless the effect is dependent on DC bias voltage. Note also that the slope of the shot noise is unimportant as long as it is linear. Thus even for a system such as a mesoscopic wire which displays shot noise with some slope lower than the full $2eI$ result, the thermometry experiment will yield the same result.

It should be mentioned that the idea of calibrating an amplifier using shot noise is not new. Several papers have been published describing shot noise calibration of amplifiers [74], including one paper describing the use of shot noise calibrations to aid in noise thermometry [30] as well as a patent by the same authors [50]. None of these works describe use of a normal metal tunnel junction to relate temperature to DC voltage using the noise, which is where the originality of the SNT lies.

The shot noise data are taken by sweeping the current bias through a normal metal tunnel junction while measuring the voltage with voltage leads very close to the junction and simultaneously measuring the RF noise power. The simultaneous RF and DC measurement is accomplished with

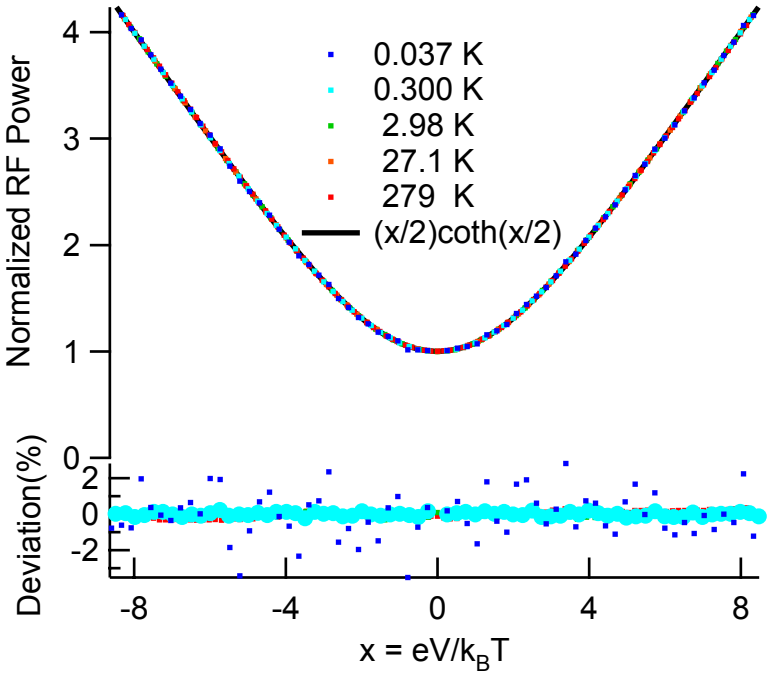

Figure 1.9: Normalized noise plots. These plots are all of data at different temperatures, where voltage has been normalized to temperature and noise has been normalized to the equilibrium noise. This shows that, up to the temperature-dependent scaling factor, the noise always obeys the same analytic expression.

a four wire bias tee circuit constructed from surface mount inductors and capacitors mounted on the same board as the tunnel junction (see Figure 1.8). The tunnel junctions used in this work are Al-AlOx-Al junctions, made with the Dolan bridge double angle technique, some optical and some with electron beam lithography. A magnetic field is applied to drive the junctions normal in all experiments done below 1 K. There are four inductively coupled leads to allow for accurate DC measurements, and both the signal and ground side of the RF port are coupled via capacitors. The RF chain consists of a low noise high electron mobility transistor (HEMT) amplifier siting in the liquid helium bath for the first stage, followed by a series of room temperature amplifiers, with a diode at the end that converts RF power to a DC voltage which is recorded by a digital voltmeter. Amplifier drifts are removed using a digital lock-in technique in which voltage is alternated between some finite bias and zero, and only differences in noise are recorded.

The majority of the data presented in this work are sets of 40-100 points, over the range from $-10k_BT/e$ to $+10k_BT/e$, because these are good parameters for testing the accuracy of the junction

physics. Figure 1.9 shows noise data at a variety of temperatures, normalized to show the universality of the shape of the noise curve. A typical optimized SNT measurement with cryogenic HEMT amplifiers has a temperature resolution of between 5 and 10 mK/$\sqrt{\text{Hz}}$, meaning that to get a 10% temperature reading at 10 mK takes about a minute and a half. With lower noise temperature amplifiers, this could well be pushed down by several orders of magnitude, allowing the SNT to be used as a high-speed readout capable of controlling a feedback loop. Such low noise temperature amplifiers could be constructed using DC superconducting quantum interference devices(SQUIDs) with a resonator coupled at the input.

The SNT has been demonstrated to work to within at least 10% over the range of temperature from 300 K to 10 mK, with as high as 0.3% absolute accuracy and 50 part per million precision in the range from 5 K to 15 K (see Figure 1.10). The agreement of noise data with theory was also verified to the 50 ppm level. The utility of the SNT was demonstrated by writing a LABView program that read out temperature automatically in a strip chart format, and by using the SNT to verify the base temperature of a new dilution refrigerator. The voltage setting and data interpolation done by this program could easily be coded into a microcontroller, allowing for a compact and affordable independent readout of the SNT to be constructed. This combination of simple readout and wide range could make the SNT an extremely useful tool for the low temperature physicist, and would make a highly useful commercial product. The relevance of the SNT for practical thermometry has also generated some interest in the popular and scientific press [3, 13, 14, 27].

The demonstrated accuracy of the SNT is already high enough to strongly suggest that it could play a role in temperature metrology below 1 K. While the same statement is not yet true of the work above 1 K, it seems possible that with further investigations into the systematic effects described in this thesis the accuracy could be improved sufficiently to make the SNT metrologically useful in a higher range.

1.6 Physics Affecting SNT Accuracy

An important effect in the operation of the SNT at the lowest temperatures is the frequency dependence of the noise. As temperature becomes comparable to or smaller than hf/k_B, where f is the measurement frequency, the zero point fluctuations become increasingly relevant, and the expression

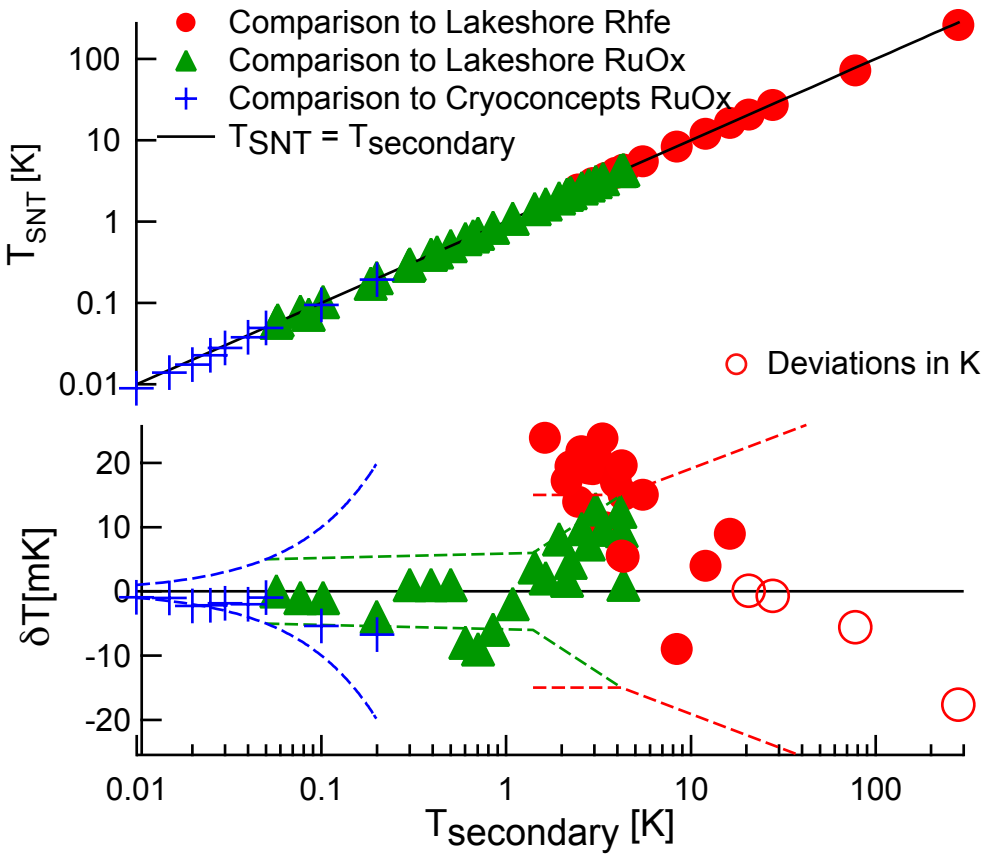

Figure 1.10: Comparison of SNT temperature measurements with various secondary thermometers. The top graph shows SNT temperature plotted against secondary thermometer temperature, and the bottom graph shows the deviation in milikelvin, except for the red open circles at the high end of the temperature scale, which are in kelvin. Red markers represent comparisons to a calibrated Lakeshore rhodium iron thermometer and green markers represent comparisons made to a calibrated Lakeshore ruthenium oxide thermometer, both compared in the Heliox pumped helium-3 cryostat. Blue markers are data taken in the Cryoconcepts dilution refrigerator and compared with the Cryoconcepts ruthenium oxide thermometer, with appropriate quantum corrections described later. Dotted lines indicate stated calibration uncertainties of the three thermometers, color coded for each thermometer.

for equilibrium noise above is replaced with the expression

$$S_I(f) = \frac{2hf}{R} \coth\left(\frac{hf}{2k_BT}\right). \tag{1.11}$$

This expression is totally general to all equilibrium noise measurements. In a tunnel junction at finite bias, however, when frequency is taken into account, the full expression for the noise is

$$S_I(f,V,T) = \frac{2k_BT}{R}\left[\frac{eV+hf}{2k_BT}\coth\left(\frac{eV+hf}{2k_BT}\right) + \frac{eV-hf}{2k_BT}\coth\left(\frac{eV-hf}{2k_BT}\right)\right]. \tag{1.12}$$

As the thermal energy lowers relative to the measurement photon energy, the noise at zero bias raises relative to the zero frequency Johnson noise result, raising the apparent temperature based on a naive zero frequency fit. Using the correct finite frequency noise form given above gives an accurate fit temperature, however. The effect of finite frequency on the noise curve can be seen in the normalized curves shown in Chapter 8. Even in the limit of hf being much larger than k_BT, the shot noise thermometer will still give an accurate fit of temperature. In this limit, the noise from the junction will be totally independent of bias voltage for very low bias voltages, and will transition smoothly to the linear shot noise limit for eV > hf. This transition will take place at approximately $V = hf/e$, and the curvature of this transition contains information about the temperature. A fit of noise data for a large enough voltage range will still yield accurate temperature readings.

By measuring the gain as a function of frequency using a spectrum analyzer, I was able to generate a fit function that was a weighted average of the finite frequency noise expression at several frequencies. The SNT data were then fit with this expression to extract the temperature. The fit temperatures were also calculated using the zero frequency expression, which diverged from the finite frequency result for low temperature. With these frequency effects taken correctly into account, the agreement of the SNT to a ruthenium oxide thermometer calibrated at 10% accuracy has been verified down to 10 mK. Further comparisons with higher accuracy thermometers in this range would be extremely useful, and will hopefully be done in the near future in European metrology labs.

The ultimate limitations in accuracy in the SNT, particularly at the higher temperatures are the various ways in which the junction parameters change with bias voltage. The above discussion of the physics of junctions is a good approximation at low bias voltages, but is not by any means complete. As the voltage across the junction increases, the shape of the tunnel barrier changes, which changes the tunneling matrix elements and causes the conductance to depend on voltage. This effect leads to an increase in conductance from the zero bias value and hence an increase in current from the value

expected in a linear device. The nonlinearity of the current directly affects the noise, and means that the expression $S_I(V) = 2eI(V)$ cannot be replaced by $S_I(V) = 2eV/R$ as above. It is believed that as long as tunneling is elastic that this expression for shot noise spectral density applies for nonlinear devices. Also, the changing impedance of the device leads to a changing coupling of the current noise to power on the 50 Ω load of the RF circuit. This effect is quite subtle, and can lead to very complex corrections when multiple reflections of the various noise signals in the system are taken into account. It is possible, however, to largely eliminate the complexities of the RF coupling effects by careful impedance matching of the device and careful selection of measurement frequencies.

In addition to the nonlinearity described above, there are some other, less well understood effects which are observable in the tunnel junctions studied here. First of all, as the voltages get large enough to excite vibrational modes in the alumina barrier, inelastic tunneling events affect the current. These manifest themselves as kinks in the conductance as a function of voltage, or as peaks in the derivative of conductance. These peaks have been observed in many tunnel junctions, and are well-reported in the literature going back to the 1960's. The study of such peaks is a well-developed field called Inelastic Tunneling Spectroscopy, or IETS. IETS studies of clean aluminum oxide junctions typically show no peaks until 115 mV, which is known to correspond to a Al-O vibrational mode in the barrier. These peaks are only visible below about 80 K. I have observed these peaks, and seen them to be in good agreement with the IETS literature. The effect of these peaks on shot noise is unknown. Inelastic tunneling effects are known to enhance shot noise in quantum dot systems, and it makes sense that the same effect would apply here. I have not been able to convincingly verify this physics in the present study, however. Chapter 2 contains a much more detailed analysis of this issue, and it is an interesting subject for future investigation.

Another far more mysterious effect observed in the tunnel junctions in this study was the zero bias anomaly. The zero bias anomaly I observed manifested itself as a decrease in conductance at zero bias, with the conductance hitting a minimum at about plus or minus 15 mV and then curving up with voltage as one would expect. As with the IETS peaks, this effect is only observable at temperatures below about 80 K. There are some reports in the literature of this zero bias anomaly, but it is not clear that it is theoretically well understood, and not all tunnel junctions show this behavior. It is reported to be due to magnon interactions in the barrier, but there are no papers describing either the theoretical or experimental effect of this physics on shot noise. Once again, this phenomenon has not manifested itself in the noise in an observable form, and I will discuss its

theoretical possibilities in chapter 2.

A deviation from ideal behavior that must be accounted for or carefully kept small is nonlinearity of the RF measurement chain. Amplifiers and detector diodes both display nonlinearity, generally by producing a lower output than would be expected from a linear response. The measurement chain nonlinearity can be tested for by adding attenuators right before the measurement apparatus in question and observing the difference in the shape of the shot noise curve. Nonlinearity may also be measured independently of the shot noise by putting a sine wave into the input of the chain with a step attenuator at the input, and varying the attenuation. This allows for very large powers to be measured, which gets a high signal to noise ratio measurement of the nonlinearity of the measurement as a function of power. From this, a Taylor expansion of the power detecting behavior may be determined from which the low power behavior may be extrapolated. The easiest way to deal with this effect is to simply add enough attenuation at the input of the measurement chain to be sure, based on the above extrapolation, that it will not affect the temperature fit to the desired level of accuracy. This requires that one pay a price in noise temperature and gain of the system, leading to longer data acquisition times, but it is only relevant for metrological accuracies. Another approach for eliminating this systematic effect is to put two junctions in series with a capacitor which are independently biased by separate inductively coupled leads. This "noise bridge" configuration allows total noise power output from the combined system to be held very close to constant, while contours in a two dimensional voltage space are traced out. These contours represent level curves on a square pyramid with rounded edges, and reveal temperature information by their curvature. I have successfully demonstrated this technique, although I have not used it for precision temperature measurement.

A simple, but difficult to detect, systematic comes from the potential for inaccuracies in the DC voltage measurement caused by voltage drop in the film right next to the junction. My junction design involves placing voltage leads as close as possible to the junction, but there can still be as much as a micron of aluminum film through which current must flow after the junction before getting to the point at which voltage is actually measured. Since the SNT relates temperature to voltage, this voltage error translates directly to an error in inferred temperature, and should be a fractionally constant effect with temperature, since a voltage divider causes a fractionally constant effect in measured voltage. This effect should cause measured voltages to be *higher* than real voltages, which should also cause inferred temperatures to be higher than real temperatures. I will show in later

chapters that this is probably an important effect in the highest accuracy measurements.

An effect that I have seen no evidence for but which must affect the SNT operation at some level is self-heating. When a finite voltage bias V is applied to the junction, power V^2/R is injected into the leads, which can cause local heating next to the junction, leading to an error in temperature reading. The effect of this error is not obvious, however. When the junction is at zero bias, there is no heating, and as the bias becomes large compared to k_BT/e the effect of temperature is exponentially suppressed, so the only voltages for which a higher noise is observed are intermediate voltages one or two k_BT/e out from zero. A raising of these noise powers has the effect of sharpening the point of the rounded "V", making a lower apparent temperature as well as changing the shape of the noise curve. Because the thermal conductances expected from the Wiedemann-Franz law at very low temperatures are proportional to temperature and the voltages applied in a given measurement area also proportional to temperature, it can be seen that in this limit the *fractional* effect of heating is constant. I calculate the effects of heating in this thesis, and believe based both on calculations and on observations that this is not a significant effect.

A variety of more exotic systematic errors could affect the ultimate accuracy of the SNT, and will be discussed in some detail in later chapters and are not worth elaborating on in this introductory chapter. These include the possibility that the surface mount components have some voltage dependence, the voltage dependence of substrate loss, the accuracy of the Fermi function for describing the occupancies of states in the metals, Coulomb blockade, jitter in the voltage bias that smears out the SNT curve, and real temperature differences between different parts of the cryostat.

1.7 Overview of this Thesis

This thesis describes the development of the shot noise thermometer both as a practical tool for the low temperature physicist and as a potential new temperature standard for metrology. In addition to the obvious purpose of satisfying the requirements for the PhD, it is intended to serve as a guide and reference for experimenters who wish to work further on development of the SNT in the future. Finally, it is hoped that the introduction in this chapter is sufficient to give lab managers the ability to judge the SNT as technology and make decisions regarding its use. The design philosophy of this document is to start out with a purely theoretical discussion and to move the text in an increasingly applied direction as it progresses, ending with a discussion of potential applications from an engineering standpoint.

The second chapter of this thesis describes general theory of the system. This includes the physics of noise from tunnel junctions, an overview of shot noise, and investigations of the various nonlinear processes observed in tunnel junctions. This is the chapter in which the physics of the metal electrodes is discussed, and possible effects on the noise are explored. The third chapter includes various physical phenomena that can effect the SNT operation such as heating and voltage drops before the voltage leads.

At the heart of all SNT measurements is the need to determine fit parameters from a set of data by comparing that data to a nonlinear function. In order to understand both the statistical and systematic errors in this determination, a detailed analysis of the fitting procedure is necessary. The fifth chapter describes this analysis and explains how it can be used to find the optimal choice of voltage points to acquire as well as the effect of various nonlinearities on temperature accuracy.

The sixth chapter describes the fabrication processes used in this work, sketches some of the difficulties involved in the fabrication, and describes what could be done in the future for improvement. The detailed recipes are included in the appendicies.

The seventh chapter describes the various apparatus used for these measurements as well as the apparatus that should be further developed for the SNT to become more practical for general use. This includes the description of our "copper tapeworm" twisted pair filter cable, a description of the various sample holders and circuit boards used, and the various wiring and software that were used.

The eighth chapter presents the measurements, with detailed plots of relevant data and descriptions of exactly what was measured an how. The ninth chapter outlines all the potential applications I see for the SNT in the future and describes what is needed to get those applications reduced to practice. Finally, chapter ten is a conclusion with an overview of what has been accomplished and what still needs to be done.

Chapter 2

Theory of Steady State Current in Tunnel Junctions

2.1 Introduction

In order to account for all the SNT systematic effects it is necessary to understand all the ways in which the physics of tunnel junctions deviate from the simple linear model presented in the previous chapter. The purpose of this section is to provide a survey of the theory of DC transport in tunnel junctions both as a general reference and to guide the reader through the various references to these effects in later chapters. In the interests of providing background and reference material, a historical overview of tunneling with first be given, followed by a discussion of nonlinearities caused by the zero bias anomaly, the Coulomb blockade, and inelastic effects in the tunnel barrier.

2.2 Tunneling and Tunnel Junctions: Historical Overview

Quantum mechanical tunneling is the process of a particle traveling from one state or position to another in a way that would be classically prohibited. According to the wave mechanical theory of quantum mechanics formulated in the 1920's, particles may be described by wave functions. These wave functions may have non-zero value even in classically forbidden regions of space, i.e. where there is a potential barrier of greater energy than the kinetic energy of the particle. If the barrier is of finite thickness, this penetration of the wave function leads to a non-zero probability that the particle will "tunnel" from one side of the barrier.

Some of the earliest triumphs of wave mechanics were applications of the concept of tunneling to various physical problems [20]. The first such application came in the beginning of 1928

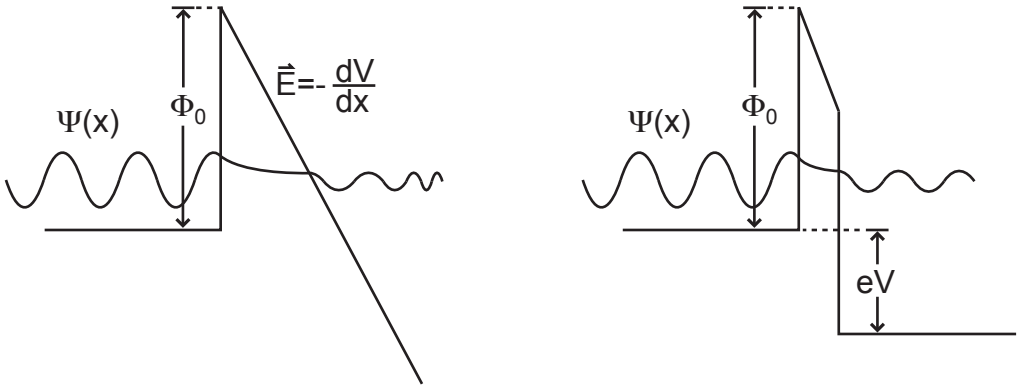

Figure 2.1: Left inset shows the Fowler-Nordheim model of an electron tunneling out of a cold metal under a high electric field. Right inset shows the trapezoidal barrier model of a tunnel junction under voltage bias. Both diagrams show the qualitative behavior of the wave function of a particle as it tunnels through the barrier.

when Oppenheimer used tunneling to explain the ionization of atomic hydrogen [52]. Also in 1928, Gamow [25] explained alpha decay using tunneling, and Fowler and Nordheim [22] explained the emission of electrons from cold cathodes using tunneling. The left inset on Figure 2.1 shows the Folwer-Nordheim model that describes an electron escaping from a metal under an electric field. This theory used a simple one dimensional wave mechanical model to predict correctly and quantitatively the exponential dependence of the tunnel current on electric field. In 1930, Frenkel [23] first described theoretically the tunneling of electrons through an insulating barrier separating two pieces of metal. Frenkel's analysis was based on a rectangular potential barrier, the transmission coefficient of which had previously been computed. His treatment dealt with the case very near zero voltage where the current is linear with voltage, and described qualitatively the idea of using two different metals separated by a tunnel barrier as a rectifier. In the Frenkel treament, as in all treatments in this section, the tunnel junction is considered to be a vast array of single-particle one dimensional problems in parallel for simplicity.

In 1951, Holm applied the WKB approximation to the problem of a trapezoidal barrier, as shown in Figure 2.1 [29]. The WKB approximation continues to be a commonly used method for analyzing the transmission through a tunnel barrier. The WKB approximation [42] gives the transmission coefficient D of a particle of mass m and kinetic energy E_x through a barrier of thickness d defined

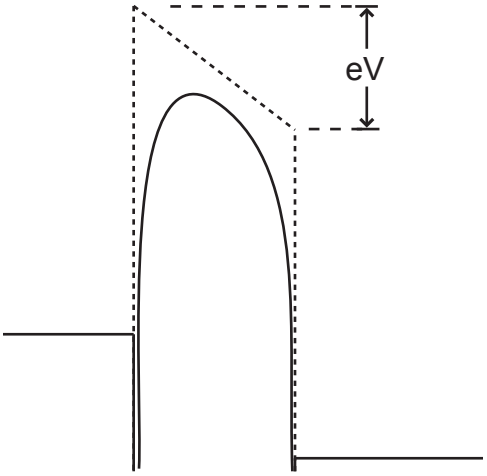

Figure 2.2: Qualitative sketch of barrier modifications due to image forces. Dotted line shows unmodified trapezoidal barrier with a bias voltage V applied. Solid line indicates modified barrier shape.

by the potential $\phi(x)$ as

$$P(E_x) = \exp\left[-\frac{2}{\hbar}\int_0^d \sqrt{2m(\phi(x) - E_x)}dx\right]. \tag{2.1}$$

This formula is of use for barriers of arbitrary shape. Real tunnel barriers are not the perfect trapezoids depicted in Figure 2.1. The image forces of charges near the barrier lead to a rounding of the barrier shape as shown in Figure 2.2. This effect was taken into account in the more detailed theoretical analysis performed by Simmons in 1963 [71], in which the image forces were computed in order to correct the barrier shape, and tunnel currents were found from the WKB approximation.

In 1961, Fisher and Giaever [21] measured the electrical characteristics of a set of tunnel junctions that they made out of evaporated metal films separated by an aluminum oxide tunnel barrier, similar to the devices described in this work. In 1962, Josephson described theoretically the existence of a current between two superconductors separated by an insulating barrier at zero voltage bias [33, 34]. In 1974, Josephson, Esaki and Giaever shared the Nobel prize in physics for their contributions to tunneling. The following decades led to both scientific developments in tunnel junction studies and various tunnel junction based technologies such as tunnel diodes and Josephson mixers.

The next major historical development of relevance to this dissertation is the Dolan bridge fabrication method [26, 47]. This method, described in detail in the fabrication section, consists of using some form of suspended bridge to evaporate two layers of metal from different angles without breaking the vacuum in an evaporator, so that small junctions with thin oxides may be fabricated

easily. This innovation in fabrication has led to many further development in tunnel junction based technology, including the single electron transistor and other Coulomb blockade based technologies.

2.3 Nonlinearities due to Barrier Shape and Density of States

As was mentioned in section 2.1, a changing voltage leads to a change in the shape of the tunnel barrier, which leads to a change in conductance. By evaluating the transmission coefficient of a trapezoidal barrier as shown above using the WKB approximation, the conductance is found to be parabolic in voltage, to first order. In the junctions measured in this work, there is a slight asymmetry in the metal films which leads to an offset of a few millivolts in the conductance parabola. For biases of a few tens of millivolts or less and for temperatures above about 80 K, this is a good approximation.

In Brinkman, Dynes and Rowell's 1970 paper [9], a very useful set of expressions are derived for the approximate behavior of tunnel junctions under an applied bias. In this section, I will follow their treatment closely, and state their main results. In their analysis, the current density was evaluated as

$$j = \frac{4\pi e}{\hbar} \sum_{k_t} \int_{-\infty}^{\infty} \rho_1(E)\rho_2(E - eV)P(E_x)[f(E) - f(E - eV)]dE_x, \tag{2.2}$$

where E is the total energy, k_t is the transverse momentum, $P(E_x)$ is the probability that an electron with kinetic energy E_x will tunnel, ρ_1 and ρ_2 are the densities of states of the metals on the two sides of the junction, and f is a Fermi function. In the above treatment, the temperature is taken to be zero, and the probability of barrier penetration is taken to be the WKB result from equation 2.1. When all the pre-factors are factored out, the normalized conductance found from this analysis can be expanded as a Taylor series to get the following simplified expression:

$$\frac{G(V)}{G(0)} = 1 - \left(\frac{V_0}{V^*}\right)^2 + \left(\frac{V - V_0}{V^*}\right)^2, \tag{2.3}$$

where G(V) is the conductance as a function of voltage and G(0) is the conductance at zero bias. V_0 and V^* are defined as

$$V_0 = \frac{\Delta\phi}{6\pi}\frac{\lambda_F}{d} \tag{2.4}$$

and

$$V^* = \frac{\sqrt{2}}{\pi}\frac{\lambda_F}{d}\bar{\phi}, \tag{2.5}$$

and d, $\bar{\phi}$ and $\Delta\phi$ are the barrier thickness, the average barrier height in volts and the difference in work function in volts, respectively, and λ_F is the Fermi wavelength defined by

$$\lambda_F = \frac{2\pi\hbar}{\sqrt{2me\bar{\phi}}}. \tag{2.6}$$

This analysis also leads to the expression for the zero bias conductance

$$G(0) = \left(316\frac{\sqrt{\bar{\phi}}}{d}\right)\exp\left(-1.025d\sqrt{\bar{\phi}}\right), \tag{2.7}$$

where G is measured in $\Omega^{-1}\mu m^{-2}$, d is measured in Ångstroms, and $\bar{\phi}$ is measured in electron volts. Equation 2.3 states that a difference in the work functions of the two metals leads to a voltage offset in the minimum of the conductance. This offset is

$$V_{min} = 0.649\frac{\Delta\phi}{d\sqrt{\bar{\phi}}}, \tag{2.8}$$

where $\bar{\phi}$ and $\Delta\phi$ are in volts and d is in Ångstroms. With these approximations, it is possible to roughly estimate the parameters of a tunnel junction. This can be useful to make sure that junction behavior is plausible, but must be taken with some skepticism since there are in general very large errors in the pre-factor of the conductance due the the nonuniformity of the barrier as a function of position in the plane of the junction.

Figure 2.3 shows a typical normalized conductance curve for a 90 Ω junction at room temperature, along with a parabolic fit. From the curvature of the conductance, one may estimate that for a barrier thickness of about 11 Å the effective potential barrier is about 0.6 V high. This is significantly lower than the expected work function. This could in part be due to neglecting the effect of the reduced effective mass of the electron in aluminum oxide.

Typical junctions in this work had an average resistance area product of approximately 300 $\Omega\mu m^2$. At the microscopic level, this is generally assumed to be not a uniform oxide of that resistance area product, but rather a vast array of single channel "hotspots", where the barrier is thinner, surrounded by regions where the transmission probability is much lower. The detailed microscopic structure of this behavior is not well understood.

While barrier shape change is the dominant effect in a wide range of tunnel junction measurements, the energy dependence of the density of states should also have some effect on the voltage dependence of the conductivity. I have not observed this as an experimental effect which may be distinguished from other nonlinearities, although this is the totally dominant effect when one or

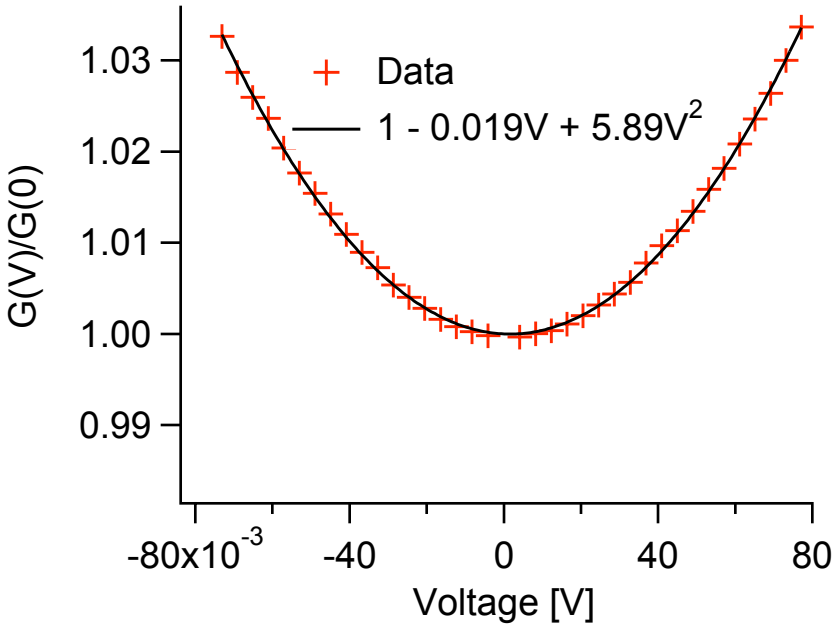

Figure 2.3: Parabolic conductance. Conductance data of a typical SNT junction at room temperature fit to a parabola. These fit parameters correspond to characteristic voltage values $V^* = 0.412$ V and $V_0 = 0.0016$ V.

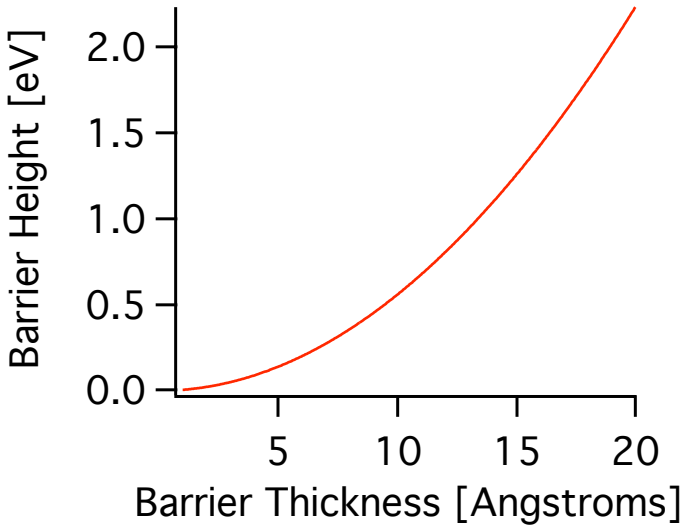

Figure 2.4: Plot of barrier height versus thickness, computed from Equations 2.3 and 2.4, assuming the measured nonlinearity.

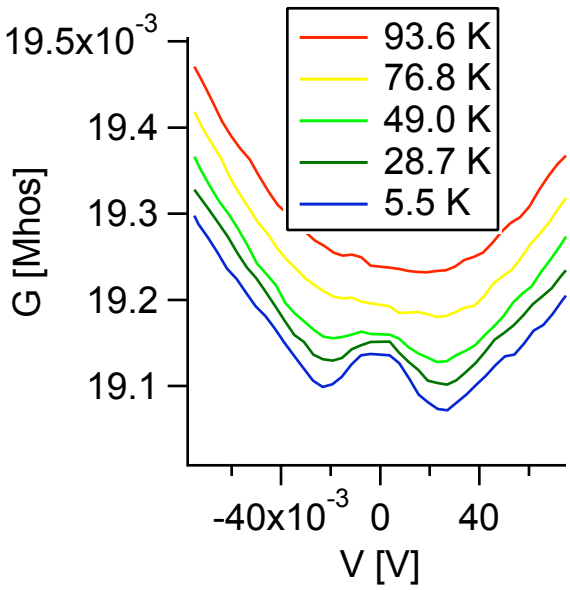

Figure 2.5: Conductance data at different temperatures. These data show the behavior of the zero bias anomaly described below.

more of the electrodes is a superconductor. The important distinguishing fact about the nonlinearities discussed in this section is that, while the current through the junction may be a difficult to predict function dependent on unmeasurable microscopic parameters, it is always elastic, at least in theory. As I will discuss in the next chapter, this is important for the theory of the shot noise of such junctions.

2.4 The Zero Bias Anomaly

The term "zero bias anomaly" has been used to refer to a variety of physical phenomena. I use the term to refer to a specific feature in the conductance of the junctions I measured that appears at temperatures of a few tens of kelvin and below. This feature appears as a depression of the conductance, which is almost symmetric in voltage, and peaks at about plus and minus 25 mV. While I was not able to conclusively verify the origin of this feature, it appears to be similar to features seen in the literature of tunnel junction studies from the 1960's which called it a zero bias anomaly. In this section I briefly review that literature.

The zero bias anomaly in normal metal junctions was first reported by Wyatt in 1964 [75], and then studied in more detail by Rowell and Shen [63, 69, 70], who investigated the magnetic field and temperature dependence. I was unable to find any reports in the literature of features that

were clearly the same size and shape as those I observed, since none of the reported data in the above papers was for aluminum-aluminum oxide-aluminum tunnel junctions. All the published data I found were of different metals. These data differed from my data in that the shape of the feature right around zero bias was much sharper in the published data, and their conductance minima were at about a third of the bias I observed.

Shortly after the experimental discovery of the zero bias anomaly, attempts were made to explain it theoretically [19, 1, 2, 4, 10]. These models explained the zero bias anomaly by assuming that impurities in the barrier or on the surface of the metal directly in contact with the barrier were interacting with the electrons as the tunneled, altering the conductance. In the treatment by Appelbaum, the data of Shen and Rowell as well as Wyatt able to be fit to a model involving magnetic impurities, which explained the observed magnetic field dependence in the work of Shen and Rowell.

After the initial experimental discoveries and theoretical treatments in the mid to late 1960's, interest in the zero bias anomaly has waned, which explains the lack of data on the system used in this work. Perhaps interest will be renewed with the growth of magnetic tunnel junction technology.

2.5 Electron-Electron Interaction Effects

Electron-electron interactions manifest themselves in several nonlinearities which have been observed in tunnel junctions. The most widely observed and exploited effect is the Coulomb blockade [17, 24]. The effect manifests itself in tunnel junctions in which the capacitance is such that the charging energy

$$E_C = \frac{e^2}{2C} \tag{2.9}$$

is comparable to the energy scale set by the temperature. A typical junction used for single electron transistor measurements has a barrier of about 10 Å of aluminum oxide, which leads to a capacitance of about 1 fF, and a charging energy of about 1 K. The junctions used in this work were approximately 1000 times larger in area, and therefore capacitance, leading to typical charging energies of about 1 mK. Since all the work described here was an order of magnitude or more above that temperature, the Coulomb blockade should not appear in these junctions. Nonetheless, I review the concept here and estimate its effect both to prove that this effect should not matter here and to estimate what its consequences would be at lower temperatures closer to the charging energy.

The Coulomb blockade was first observed [24] in devices with multiple tunnel junctions, in

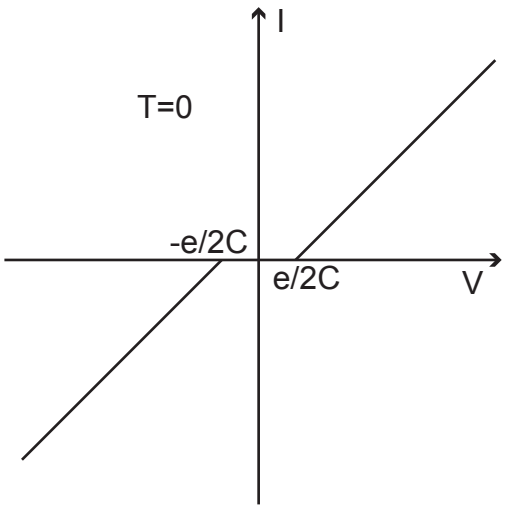

Figure 2.6: Coulomb blockade in naive zero temperature model with infinite impedance voltage leads. For very small tunnel junctions with high impedance leads at very low temperatures, the measured I-V curves look like rounded versions of this conceptual plot.

which the charge on a metal "island", connected to the outside world only by tunnel junctions, was quantized. It has also been observed, however, in single junctions, and this treatment will deal only with the single junction case.

The simplest theoretical description of the Coulomb blockade comes from treating a small tunnel junction at zero temperature as being under a perfect current bias with the voltage across the junction being measured by an infinite impedance voltmeter [17]. In this picture, the change in electrostatic energy associated with a tunnel event may be calculated as

$$\Delta E = \frac{Q^2}{2C} - \frac{(Q-e)^2}{2C} = \frac{e(Q-e/2)}{C}, \tag{2.10}$$

where Q is the charge across the junction capacitance C. This quantity must be positive in order for a tunneling event to take place. This condition will be satisfied only for voltages with absolute value greater than e/2C, and at zero temperature no current will flow for voltages with smaller absolute value. Thus the current is "blockaded" around zero bias by electrostatic interactions, which explains the name "Coulomb blockade".

In practice, this model is naive, and the effect of the Coulomb blockade depends strongly on the impedance of the junction environment. The effect of the environmental impedance has been both described theoretically and observed experimentally [16]. As the environmental impedance gets small compared to the resistance quantum $R_K \approx 26$ kΩ, the Coulomb blockade becomes more

difficult to observe.

Another electron-electron effect that can appear in tunnel junctions is due to the finite time required for the potential along the edge of the junction to equilibrate after an electron tunnels. This effect is described in detail both experimentally and theoretically in a 2001 paper by Pierre et al. [55]. In these experiments, the conductance of a long, skinny tunnel junction with one electrode made out of high resistance film was measured.

In this paper, the fractional change in conductance is calculated to be

$$\frac{\delta G}{G_t} = -\sqrt{2}\frac{R_l}{R_K}\sqrt{\frac{\hbar D^*}{eV}}, \tag{2.11}$$

where R_K is h/e^2, R_l is resistance per unit length, and

$$D^* = \frac{1}{R_\square C_s}, \tag{2.12}$$

where C_s is the capacitance per unit area, and D^* has units of m^2/s. This effect scales with the square root of the resistance per unit length of the wire. The wire in Pierre et al. had a resistance per unit length of about 12 Ω/μm. It is difficult to compare the junctions used in this work since they had such different geometry, but even in the worst case scenario where they are treated as straight wires, and diffusion through the leads is neglected, they have about two orders of magnitude lower resistance, leading to a one order of magnitude smaller fractional effect in the conductance. This represents a worst case scenario, however, since it neglects the two dimensionality of the conduction in the SNT junctions.

2.6 Inelastic Electron Tunneling Spectroscopy

As the bias voltage on a tunnel junction is increased, the tunneling electrons have access to higher and higher energy states in the barrier. A variety of such states may exist at different energies which lead to inelastic tunneling events. These states appear as peaks in the second derivative of current with respect to voltage, and the study of these peaks has become a rich field, called inelastic tunneling spectroscopy, or IETS [38, 31, 39].

Figure 2.7 shows the schematically an inelastic tunneling event. As indicated in Figure 2.8, putting enough bias voltage on the junction to enable these processes leads to an abrupt increase in conductance, or a peak in the derivative of conductance. The width of these peaks can be set either by temperature or the natural line width of whatever state is being probed. When they are temperature limited, the full width at half maximum of the IETS peaks is given by $5.4k_BT/e$.

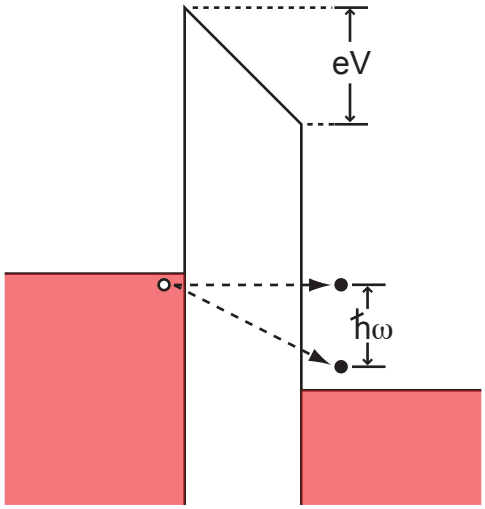

Figure 2.7: Illustration of an inelastic tunneling process. When becomes larger than $\hbar\omega$, a mode in the barrier of frequency ω opens up new channels for conduction which end up $\hbar\omega$ lower than the elastic tunneling state.

The energies probed by IETS are generally in the range from about 0.05 eV to 0.5 eV in energy, which corresponds to infra red radiation, and various molecular vibrational modes. Thus, the states which are probed with IETS are the same as those probed by Raman spectroscopy and infrared absorption spectroscopy. This fact allows observed IETS peaks to be accurately described by correlating them with peaks in other spectroscopic studies.

In a clean aluminum tunnel junction, the only IETS peaks observed are the vibrational modes of OH molecules in the barrier. These modes consist of a bending mode at about 0.12 eV and a stretching mode at about 0.45 eV. In the junctions in this work, I always observed the 0.12 eV bending mode, but avoided the higher voltages since that is near the damage threshold for a typical junction. In published studies, the presence of any type of hydrocarbon contamination in the junction leads to many more peaks. The absence of such peaks indicates that the junctions I used did not have pump oil or other hydrocarbon contamination.

2.7 Conclusions

At a high enough level of accuracy, the effects described in this Chapter should all be important in the operation of the SNT, and are thus worth understanding for any serious continuation of this work. By

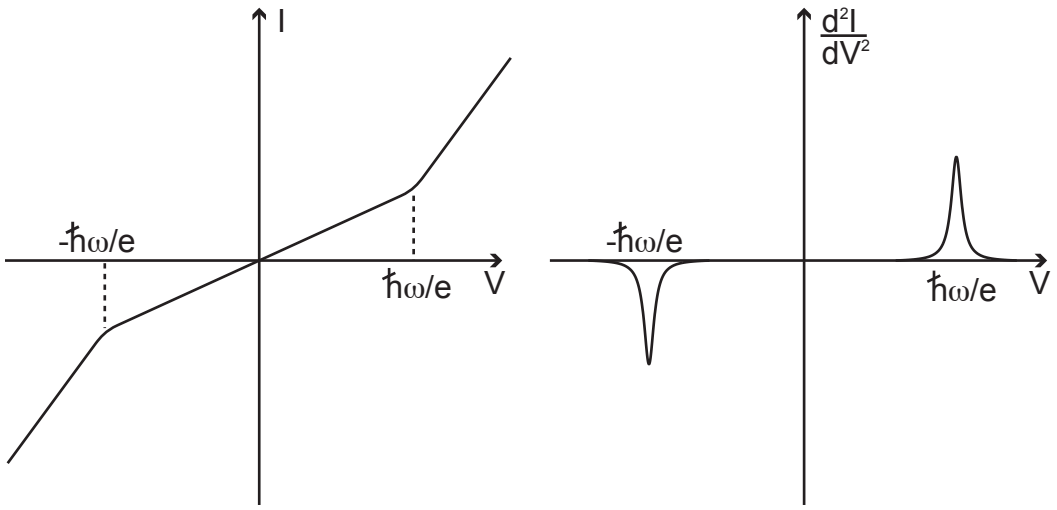

Figure 2.8: Idealized IV curve showing the effect of inelastic tunneling. In this simplified picture, which ignores barrier nonlinearities, the addition of the inelastic tunneling process simply adds a constant offset to the conductance. This addition leads to a peak in the second derivative of current with respect to voltage, plotted on the right inset.

far the most important effect for SNT operation is the parabolic deviation of the conductance, since it is the largest effect. At high temperatures (between 77 K and room temperature), the changing conductance described here is the dominant source of error in SNT temperature measurements, causing errors as large as 10 % at room temperature. This effect continues to be important in the range between 4 K and 77 K, however its importance is diminished at lower temperatures because of the lower bias voltages used at those temperatures. The bias voltages used for SNT measurements are proportional to temperature, and the size of the conductance deviations are proportional to the square of voltage, and hence also the square of temperature. For a typical SNT measurement at 1 K, the deviation in conductance expected from the parabolic nonlinearity described in this Chapter is about 15 parts per million, and another factor of four smaller for every factor of two in temperature below that. The Coulomb blockade is too small to be observable in SNT junctions, due to their large capacitance and low resistance. The effects of the zero bias anomaly and of inelastic tunneling effects from barrier states are more difficult to predict. It is not clear from the theory literature exactly what the effect of these phenomena should be on the noise, and there are no published experimental data on tunnel junctions which answer the question. Experimentally determining the effect of these phenomena on the noise from a tunnel junction will be an important task for any

future experimenter who attempts to improve the uncertainty of the SNT to metrological levels.

Chapter 3

Theory of Noise in Tunnel Junctions

3.1 Introduction

Because the SNT relies on shot noise for its operation, it is important to discuss the general theory of shot noise in order to understand the fundamental ideas behind the SNT, as well as the various corrections that must be made to the basic formulas developed in Chapter 1. In this Chapter, I discuss the theory of shot noise, starting with the a historical introduction which explains the basic concepts and following with a detailed survey of important effects in the shot noise from a tunnel junction that can affect SNT operation. This survey consists primarily of effects that have to do with finite frequency signals either being emitted or absorbed by a tunnel junction and with how the changing conductance effects discussed in the previous chapter affect the noise. The overview of tunnel junction noise theory given in this Chapter will provide the tools necessary to understand the measurements of junction noise described in Chapter 8.

3.2 Shot Noise: Overview

Shot noise is the noise due to the discrete nature of electric current. It is present in any system in which current consists of discrete current pulses carrying individual charges. Shot noise was first discovered in 1918 by Schottky [68], who dubbed it the "schroteffect", or shot effect. It was first observed in vacuum tubes (see Figure 3.1). This section will review briefly the progress that has been made in shot noise since its discovery, and will be largely based on the reviews by Blanter and Büttiker, de Jong and Beenakker, and de Jong's thesis [32, 15, 8].

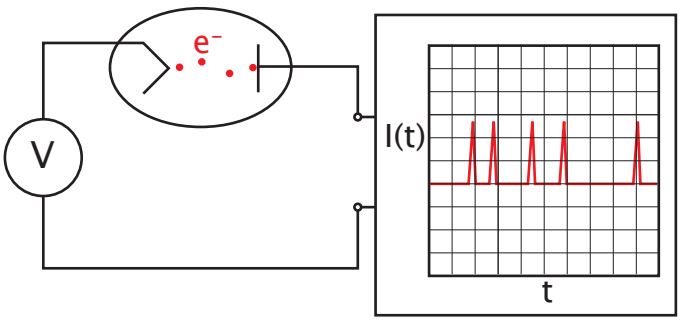

Figure 3.1: Shot noise in a vacuum tube. The central idea of this diagram is that the current in a vacuum tube consists of independent, uncorrelated pulses of current corresponding to each individual electron breaking loose from the cathode. These uncorrelated current pulses display Poisson statistics, and therefore the variance in the current is proportional to the mean of the current.

When the statistics of electron current pulses are totally uncorrelated with each other, the current is a Poisson process. In a Poisson process, the probability that k current pulses occur in a time interval T is

$$P(k,T) = \frac{(aT)^k}{k!}\exp(-aT), \tag{3.1}$$

where a is the average number of current pulses per unit time. With k current pulses per unit time, the average current is

$$\overline{I} = ek, \tag{3.2}$$

where e is the charge on the electron.

Before proceeding further into the analysis of shot noise, it is worth defining the quantity of interest for noise studies. The quantity measured is generally noise *power*, the power delivered by the noise on an RF load. This quantity is proportional to both the current spectral density S_I and the voltage spectral density S_V. These quantities are the Fourier transforms of the current-current and voltage-voltage autocorrelation functions, respectively. The correlation function of a time-dependent variable x(t) is defined for a time τ to be the average over t of the product of the deviation from the mean of x(t) and x(t+τ), $\langle \Delta x(t+\tau)\Delta x(t)\rangle$. Thus the current and voltage spectral densities are

$$S_I(\omega) = 2\int_{-\infty}^{\infty} dt e^{i\omega t}\langle \Delta I(t+\tau)\Delta I(\tau)\rangle \tag{3.3}$$

and

$$S_V(\omega) = 2\int_{-\infty}^{\infty} dt e^{i\omega t}\langle \Delta V(t+\tau)\Delta V(\tau)\rangle. \tag{3.4}$$

In this discussion, the current spectral density will generally be used, with the understanding that the quantity being actually measured is the power in some band defined by a gain function $G(\omega)$:

$$P = Re[Z_{load}] \int_{-\infty}^{\infty} G(\omega) S_I(\omega) d\omega. \tag{3.5}$$

In a device in which the current I consists of a sequence of single electron current pulses the timing of which are described by Poisson statistics, the current spectral density is

$$S_I(\omega) = 2eI. \tag{3.6}$$

If this equation universally described shot noise, the study of shot noise would simply be a very experimentally difficult way to measure exactly the same physics as is accessible in DC transport measurements. The reason that is not the case is that while the above expression assumes that electron transport events are totally uncorrelated, that is in general not true, and the deviations from the above expression allow experimenters to study the correlations of such events. Anti-correlation leads to a suppression of the noise from the Poisson limit, and is the most common in mesoscopic electronics. Correlation leads to noise above the Poisson limit, and is frequently observed in the shot noise of photon sources and is also seen in the electronic shot noise of certain quantum dot systems. The Poisson limit above is also modified in situations where the time scale associated with charge transport events is comparable to that of the frequency of noise being measured. The other information that noise gives access to which is not readily accessible in DC transport measurements is about the value of the charge carriers. This fact has been used to probe the physics of various hybrid systems of superconductors and metals, but are not reviewed here, as they are not directly relevant for the junctions in the shot noise thermometer.

Theoretical shot noise papers generally use a scattering approach to the study of shot noise with the scattering theory approach common in mesoscopic physics. Consider a sample connected to a pair of reservoirs, with the incoming wave modes from the two reservoirs denoted by I_1 and I_2. These modes get scattered to produce outgoing modes O_1 and O_2, defined by the equation

$$\begin{pmatrix} O_1 \\ O_2 \end{pmatrix} = \begin{pmatrix} r & t^\dagger \\ t & r' \end{pmatrix} \begin{pmatrix} I_1 \\ I_2 \end{pmatrix}, \tag{3.7}$$

where the elements of the scattering matrix are, in general, complex. At zero temperature, the Landauer result [40] gives, for the zero temperature conductance,

$$G = \frac{e^2}{h} \mathrm{Tr} t t^\dagger = \frac{e^2}{h} \sum_{n=1}^{N} D_n, \tag{3.8}$$

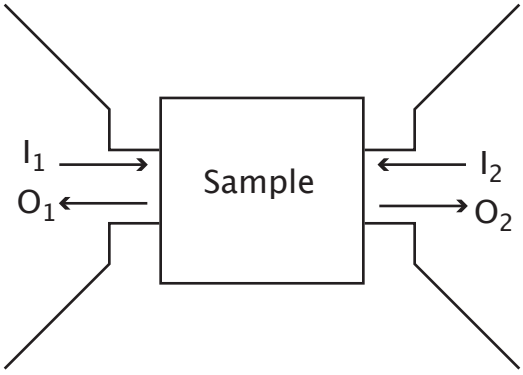

Figure 3.2: Scattering model for transport through a mesoscopic sample. I_1 and I_2 represent the amplitude and phase of electron plane wave modes incident on the sample, and O_1 and O_2 represent outgoing plane wave modes. In general, these are both complex quantities, as are the elements of the scattering matrix that describe the effect of the sample on the incident electrons.

where D_n are the eigenvalues of the scattering matrix at the Fermi energy, and are real numbers. These are the transmission coefficients of the various conduction channels, and e^2/h is the conductance quantum, about 26 kΩ or about 39 μS.

In this discussion I will state the results from this theory which are relevant to experimental shot noise results without derivations. At low frequencies and zero temperature, the shot noise is given by

$$S_I(V) = 2eV\frac{e^2}{h}\sum_{n=1}^{N} D_n(1-D_n). \tag{3.9}$$

At finite temperature, this expression is corrected to

$$S_I(V,T) = 2\frac{e^2}{h}\sum_{n=1}^{N}[2k_BTD_n^2 + D_n(1-D_n)eV\coth(eV/2k_BT)]. \tag{3.10}$$

In the situation where D_n are all very small compared to 1 and k_BT is small compared to eV, the above expressions reduce to the Poisson limit 2eI. However, for channel conductances which are significantly greater than zero, the $(1-D_n)$ term becomes important and shot noise is suppressed from the Poisson limit. The Fano factor is defined to be the ratio of the shot noise to what the shot noise would be in the Poisson limit. For the model discussed above, the Fano factor F is

$$F = \frac{\sum_{n=1}^{N} D_n(1-D_n)}{\sum_{n=1}^{N} D_n}. \tag{3.11}$$

In general, the Fano factor can be less than, greater than, or equal to 1. Several mesoscopic systems displaying sub Poissonian behavior have been investigated both theoretically and experimentally. Among these are the diffusive wire, double barrier structures, chaotic cavities, and quantum point

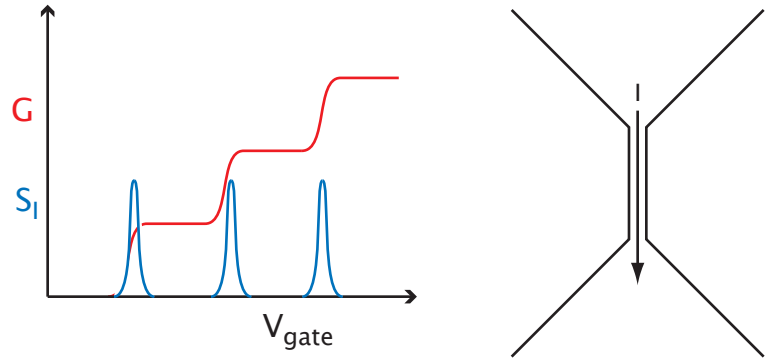

Figure 3.3: Quantum point contact. The right inset shows schematically what a quantum point contact is. By correct use of electrostatic gates over a two dimensional electron gas, a one dimensional conductor can be created, which can have conductance channels that are all the way open, all the way closed, or part way open, depending on the gate voltage. The left inset shows how the changing conductance through these channels affects shot noise. There is only a shot noise signal when at least one channel has a transmission coefficient that is neither zero nor one.

contacts. The simplest of these to understand is the symmetric chaotic cavity. In this system, an electron goes into a cavity, follows a chaotic orbit with no loss in energy, and has a 0.5 probability of coming out of either the input or the output side. Thus, the average transmission coefficient is 1/2, and the Fano factor is $\frac{1}{2}(1-\frac{1}{2}) = \frac{1}{4}$. This 1/4 suppression has been observed experimentally in cavities made from 2D electron gasses in semiconductor systems [49, 48].

The quantum point contact consists of a set of 1D conductance channels in parallel, typically made from a set of gates on top of a 2D electron gas in a semiconductor structure. Generally, there is a gate that controls how many channels are open, and varying this voltage leads to an increasing conductance that goes up in steps equal to the conductance quantum e^2/h. On each conductance plateau, each channel has either D=0 or D=1, and so the shot noise is zero. Only in the intermediate states where a channel is between being totally open or totally closed does any shot noise appear. Thus the shot noise appears a a sequence of peaks which correspond to the gate voltages between conductance plateaus. This has also been measured experimentally, although the full explanation of the experimental data is slightly more complex than the simple model presented here.

In the diffusive wire, the Fano factor is found to be 1/3 using a derivation from random matrix theory which I will not attempt to reproduce here. This result has also been successfully demonstrated in the lab [66], and this system is found to be identical, up to this factor of 1/3 to the tunnel

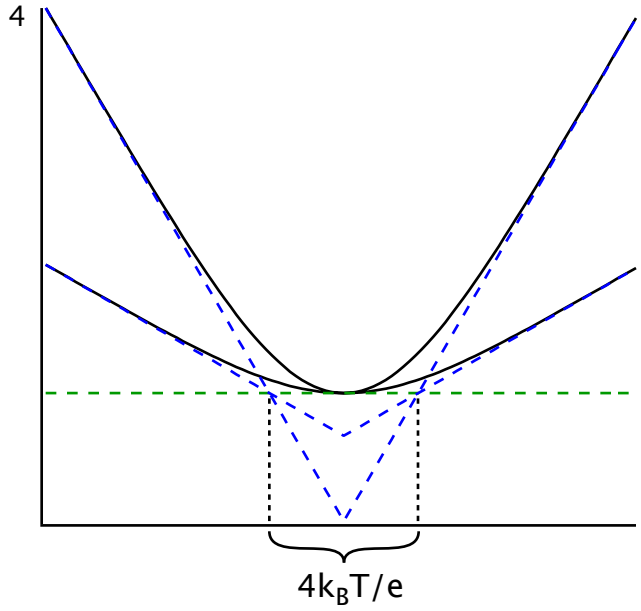

Figure 3.4: This Figure shows a theoretical plot of noise curves from two devices at the same temperature, but with different Fano factors. Note that the voltage scaling factor that determines temperature is totally unaffected by the Fano factor, and so the Fano factor has no effect on the the measured temperature in the shot noise thermometer.

junction, and can also be used as a thermometer (see Figure 3.4). While a suppressed Fano factor has no effect on the performance of the shot noise thermometer, the Fano factor of an SNT junction is in fact very close to 1, since typical transmission coefficients are of the order of 10^{-6}.

While all of the above systems involve suppression of shot noise relative to the Poisson limit, there are some systems in which the shot noise *exceeds* the Poisson limit. The most relevant of these is inelastic tunneling processes, which can also lead to sub-Poissonian noise. The systems which have been studied include various quantum dot systems and various molecular devices, all of which exhibit resonant tunneling.

3.3 Noise of a Tunnel Junction

As described in Chapter 1, the current spectral density of the noise from a tunnel junction with low transmission coefficients and at low frequency is

$$S_I(V) = 2eI \coth\left(\frac{eV}{2k_BT}\right), \tag{3.12}$$

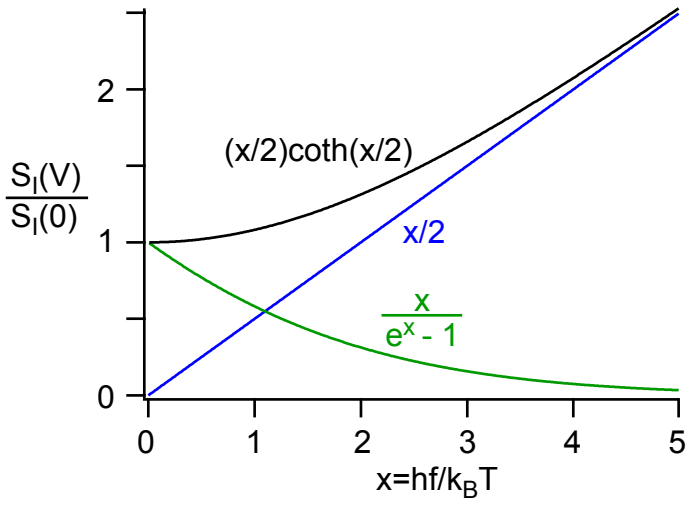

Figure 3.5: Transition of noise from thermal to zero point quantum noise. The green line represents the purely thermal contribution to the noise, which approaches zero at zero temperature or infinite frequency. The blue line represents the zero point noise, and the black line represents the full noise described by Equation 3.13. Note that the full noise is simply the sum of the thermal and zero point components. In this work, the highest value of the normalized variable x that is encountered is approximately 2.5.

where I is the average DC current through the junction, T is the temperature, V is the voltage across the junction, e is the charge on the electron, and k_B is Boltzmann's constant. As mentioned before, the hyperbolic cotangent in this expression comes from the integral of a product of Fermi functions. This integral is worked out in an appendix. The purpose of this section is to go beyond this simple model and deal with special cases, particularly those involving high frequencies.

The above expression is valid for frequencies f for which hf is large compared to k_BT. k_B/h is about 20 GHz/K, so for the measurements done here which were around half a gigahertz, k_BT was equal to hf at about 25 mK. When hf becomes comparable to k_BT, quantum mechanical corrections must be made to the noise. In the case of zero bias voltage, the noise was worked out by Callen and Welton in their original fluctuation dissipation paper [11] to be

$$S_I(f) = \frac{2}{R} hf \coth\left(\frac{hf}{2k_BT}\right). \tag{3.13}$$

Note that in the limit as frequency goes to zero, this reduces to the low frequency result $4k_BT/R$, and that in the high frequency limit, it goes to $2hf/R$. Thus, just as Equation 3.12 above describes a smooth transition from Johnson noise to shot noise, this equation describes a smooth transition from Johnson noise to zero point quantum noise.

Rogovin and Scalapino [62] derived the full expression for the noise from a tunnel junction at both finite voltage and finite frequency to be

$$S_I(f,V,T) = \frac{2k_BT}{R}\left[\frac{eV+hf}{2k_BT}\coth\left(\frac{eV+hf}{2k_BT}\right) + \frac{eV-hf}{2k_BT}\coth\left(\frac{eV-hf}{2k_BT}\right)\right], \tag{3.14}$$

as mentioned in the Introduction. This frequency dependent behavior was observed by Schoelkopf et al. in 1997 [66] in a mesoscopic wire with the 1/3 suppression of the shot noise described above.

At first inspection, it appears that in high frequency limit, the temperature information in the noise is destroyed, since in this limit the zero bias noise has no temperature dependence. One way of thinking of this is that in this limit there is insufficient thermal energy to extract any photons from the junction. When the voltage bias gets to be comparable to hf/e, however, there is a temperature dependence that comes out in a roundedness of the transition to the linear shot noise regime. The width of this transition can be used to relate temperature to voltage just as in the zero frequency limit. Figure 3.6 illustrates this principle, although in practice, temperature is found from a least squares fit, as in the zero frequency case. The details of this fitting process for finite bandwidth are described in Chapter 8. The fractional size of this effect at a fixed frequency is proportional to the inverse square of temperature, and is negligible above one kelvin. This is discussed more quantitatively in Chapter 4.

In all of the above discussion about frequency dependence, I consider the frequency to be a positive number. This is a simplification. The frequency of noise can be considered to have a sign, where positive frequencies correspond to photons being emitted by the system being measured and negative frequencies correspond to photons being absorbed by the system being measured. In general, these positive and negative frequency components are different, and the full two-sided spectrum of the noise from a tunnel junction is given by the following expression:

$$S_I(f) = \frac{1}{R}\left[\frac{hf+eV}{1-e^{-(hf+eV)/k_BT}} + \frac{hf-eV}{1-e^{-(hf-eV)/k_BT}}\right]. \tag{3.15}$$

In practice, the measurements described here all measure the sum of the positive and negative components of the noise. Figure 3.7 shows the noise from a tunnel junction plotted as a function of frequency both for the two sided spectrum and for the symmetric noise experimentally measured, for comparison.

Another important frequency dependent effect in the noise from a tunnel junction is that of irradiating a junction with a tone at a high frequency compared to k_BT/h. In this situation, there

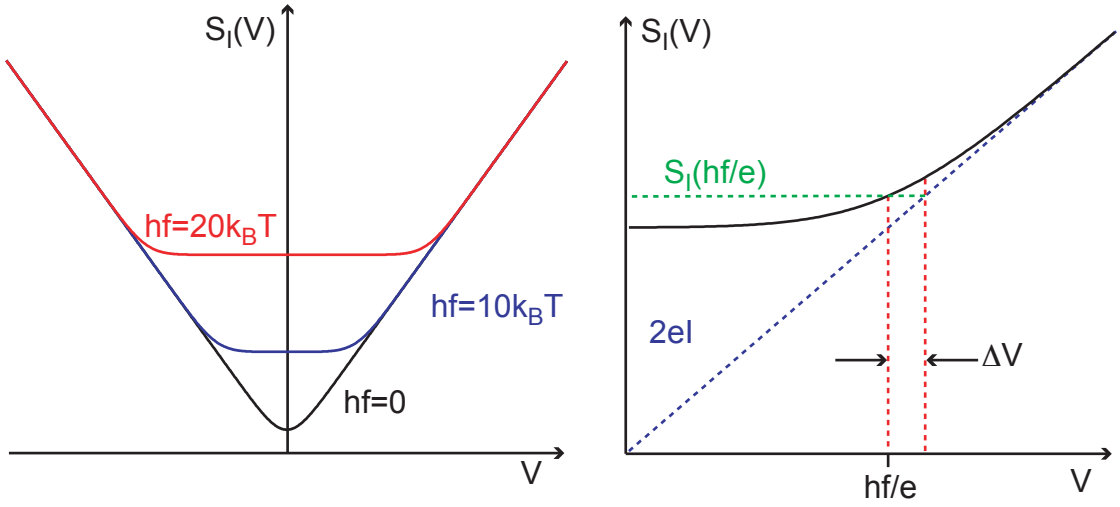

Figure 3.6: Frequency dependence of junction noise. The left inset shows the noise as a function of voltage at different frequencies, and at a single temperature. The right inset shows a detail of temperature-induced curvature in transition from zero point noise to shot noise. This diagram shows how temperature can still be related directly to a DC voltage. The distance in voltage ΔV from $S_I(hf/e)$ to the asymptotic shot noise line is shown above. This voltage difference is given by the formula $\Delta V = \frac{k_B T}{e}\left[1 + \frac{hf}{k_B T}\coth\left(\frac{hf}{k_B T}\right) - \frac{hf}{k_B T}\right]$. Since f can be known with very high accuracy, and since this function is monotonic in T, this is sufficient to relate temperature to voltage. Also, note that for very high frequencies, $\Delta V \approx \frac{k_B T}{e}$, and for very high temperatures $\Delta V \approx \frac{2k_B T}{e}$.

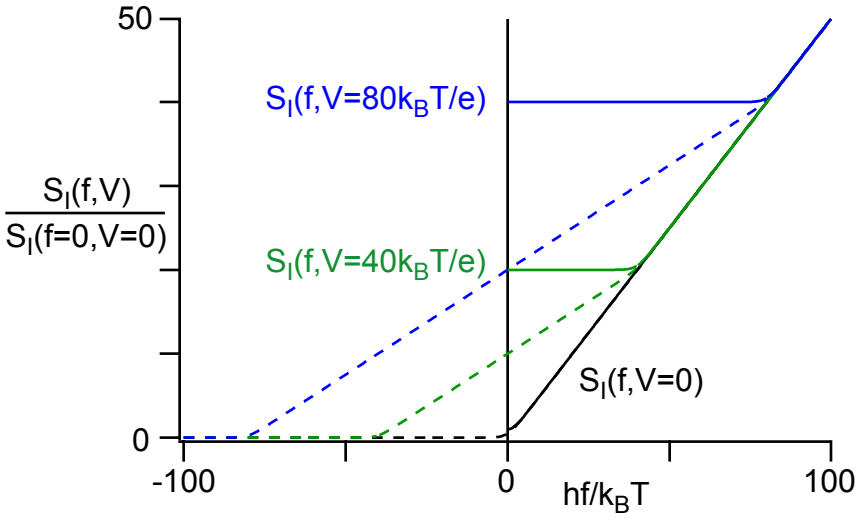

Figure 3.7: Two sided noise. Dotted lines show full two sided spectrum, where the sign of the frequency indicates whether photons are being absorbed or emitted. Solid lines show symmetric noise $S_I^{sym}(f) = S_I(f) + S_I(-f)$, which is the quantity measured experimentally in this work.

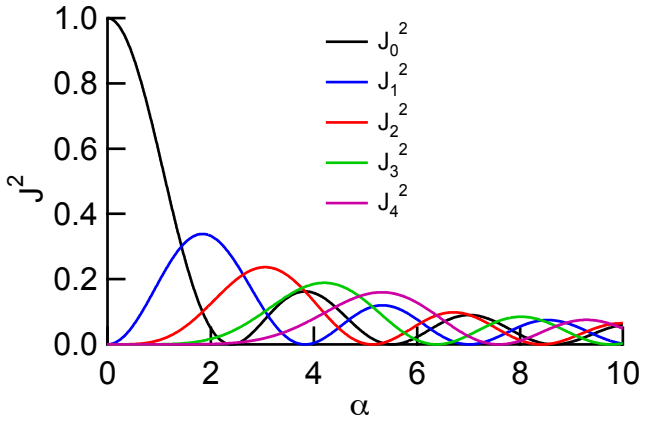

Figure 3.8: Graph showing squared Bessel functions of the first kind. In the measurements done in this work, only the first four of these were necessary due to the relatively low RF powers used.

is once again a difference in the behavior of the noise for voltages above and below hf/e. The full expression for the noise is given by

$$S_I(V,T) = \frac{1}{R}\sum_{\pm}\sum_{n=0}^{\infty} J_n^2(\alpha)\left[(eV \pm nhf)\coth\left(\frac{eV \pm nhf}{2k_BT}\right)\right], \tag{3.16}$$

where J_n^2 is the square of a Bessel function of the first kind, and $\alpha = eV_{ac}/hf$, where V_{ac} is the voltage amplitude of the irradiating signal across the junction.

This was also measured in a mesoscopic wire by Schoelkopf et al [67]. This effect could be useful for calibrating the voltage across the junction, since it relates the true junction voltage to frequency. Having direct access to that voltage could calibrate out the small voltage drops that can occur right next to the junction, as discussed in the systematics Chapter, improving the ultimate accuracy of the SNT.

3.4 Noise of Nonlinear Devices

An important question for the SNT is what exactly happens to the junction shot noise result when I(V) is some nonlinear function. Is it then possible to make the following substitution

$$S_I(V) = \frac{2eV}{R}\coth\left(\frac{eV}{2k_BT}\right) \longrightarrow S_I(V) = 2eI(V)\coth\left(\frac{eV}{2k_BT}\right)? \tag{3.17}$$

If the answer is "yes", then nonlinearities in the current may be corrected in SNT measurements by measuring the DC characteristics with high accuracy and fitting to the corrected expression. The

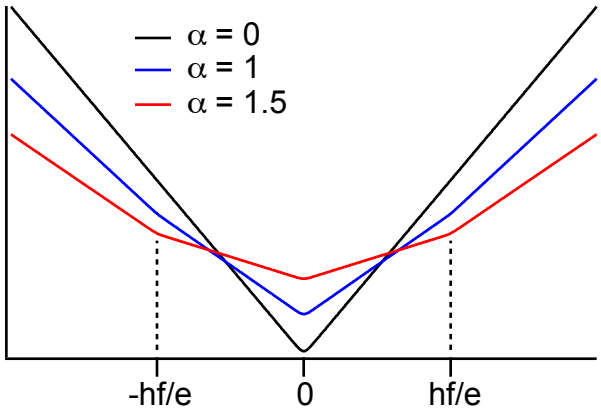

Figure 3.9: Theoretical plot of noise from a junction irradiated with radiation of frequency $100k_BT/h$ at various powers.

answer to this question is not definitively known in general. When the tunneling consists of purely elastic processes, it is believed that the above expression is rigorously true. In the case of inelastic tunneling processes, it is not clear how accurate this expression is for a tunnel junction. I was unable to determine this experimentally in the present work, however this will be an important question for future experimenters to answer if efforts are to be made to do high temperature measurements with metrological accuracy.

3.5 Noise of Coulomb Blockaded Devices

When the Coulomb blockade becomes an important effect in a tunnel junction it can have an effct on the noise. To first order, the only effect of the Coulomb blockade is to change the current I(V), which modifies the shot noise 2eI(V) accordingly. This is already a smaller effect than is observable in the SNT measurements conducted so far, since the Coulomb blockade has not been observed at all in these junctions. A higher order effect would be that because the Coulomb blockade correlates the tunneling of electrons through the junction, it should suppress the shot noise from the Poisson limit 2eI(V). Since neither of these effects is observable at the current levels of precision and temperature ranges, I omit a quantitative discussion of them. This physics may need to be analyzed more closely in the future, however, if the SNT is to be used to do metrological measurements at temperatures below 10 mK.

3.6 Conclusions

This Chapter explored both the general theory of shot noise, and the effects special to tunnel junctions that affect the operation of the SNT. The frequency dependent effects described here have all been observed in this work, and data demonstrating them are presented in Chapter 8. The effects of nonlinear junction conductance on noise are more hypothetical, and no data are presented here to confirm or deny any theories of these effects. This subject will need to be explored further by future experimenters both in order to increase the levels of accuracy of the SNT and because it is of fundamental interest in the understanding of shot noise.

Chapter 4

Systematic Effects

4.1 Introduction

There are two sources of error in error in any measurement: statistical errors, and systematic errors. Systematic errors arise from discrepancies between the theory used to describe an experimental system and the true underlying theory that describes the system. A variety of systematic effects dominate the uncertainty of SNT measurements at most temperatures. By understanding these systematic effects in detail, they may either be eliminated by improving the design of the experiment or corrected for by using a more accurate physical description of the junction noise physics. In this Chapter, I survey the systematic effects which are most important in the operation of the SNT.

4.2 Heating

In this section, heating will be discussed as a zero dimensional problem in which the thermal conduction through a slab of metal that obeys the Wiedemann-Franz law. This law will then be the basis for generalization to higher dimensions using finite element methods.

We start with the equation for heat flux through an area A in a solid:

$$\frac{1}{A}\dot{Q} = -\kappa\frac{dT}{dx}, \tag{4.1}$$

Where κ is the thermal conductivity. Assuming the Wiedemann Franz law, I get $\kappa = \mathcal{L}\sigma T$, where $\mathcal{L} = \frac{\pi^2 k_B^2}{3e^2} = 24.4$ nWΩ/K^2 is the Lorenz number and σ is the electrical conductivity. From this one may re-write the above equation as

$$\frac{1}{A}\dot{Q} = -\mathcal{L}\sigma T\frac{dT}{dx} = -\frac{\mathcal{L}\sigma}{2}\frac{d(T^2)}{dx}. \tag{4.2}$$

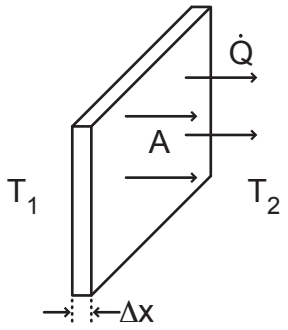

Figure 4.1: Cartoon of slab used to model zero dimensional Wiedemann Franz law.

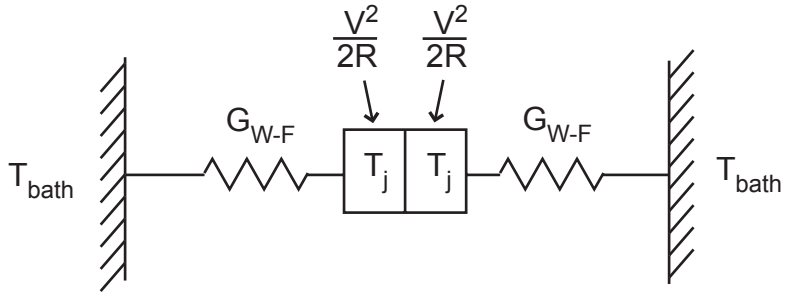

Figure 4.2: Cartoon of thermal circuit for zero dimensional heating model. The junction is assumed to put V^2/R of Joule heating into the leads, with half going into each lead.

Now, consider a thin slab of area A and thickness Δx. The electrical resistance of the slab is $R = \frac{\Delta x}{A\sigma}$, so $\sigma = \frac{\Delta x}{RA}$.The heat flux now takes the form

$$\frac{1}{A}\dot{Q} = -\mathcal{L}\frac{\Delta x}{2RA}\frac{\Delta(T^2)}{\Delta x}, \tag{4.3}$$

which leads to

$$\dot{Q} = \mathcal{L}\frac{1}{2R}(T_1^2 - T_2^2), \tag{4.4}$$

which is the zero dimensional form of the Wiedemann Franz law which I will use here.

The simplest model for lead heating is to consider each lead to be an electrical and thermal resistor with a two temperatures: T_{bath} for the bath and T_j for the junction (see Figure 2.)

The power dissipated from the conduction through the tunnel junction of resistance R_j is

$$\mathcal{L}\frac{1}{2R}(T_j^2 - T_{bath}^2) = \frac{V^2}{2R_j}, \tag{4.5}$$

which leads to the result

$$T_j = \sqrt{\frac{V^2 R_{lead}}{R_j \mathcal{L}} + T_{bath}^2} \tag{4.6}$$

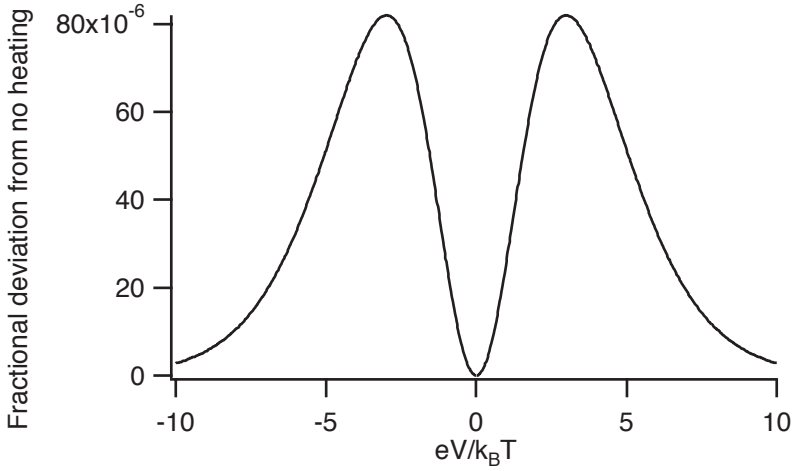

Figure 4.3: Fractional heating with $R_{lead} = 0.01\ \Omega$ and $R_j = 50\ \Omega$ as a function of normalized voltage $x = eV/k_BT$.

for the local temperature at the junction. If we define $x = eV/k_BT_{bath}$ then $V = k_BT_{bath}x/e$, and we may substitute this back in to get

$$T_j = T_{bath}\sqrt{1 + \frac{3R_{lead}}{R_j\pi^2}x^2}. \tag{4.7}$$

From this we may compute the noise from the tunnel junction

$$S = \frac{GxT_{bath}}{2}\coth\left(\frac{xT_{bath}}{2T_j}\right), \tag{4.8}$$

where G is a gain factor, and so the deviation from the unheated noise is

$$\frac{\delta S}{S} = \frac{\coth\left(\frac{x}{2\sqrt{1+\frac{3R_{lead}}{R_j\pi^2}x^2}}\right) - \coth(\frac{x}{2})}{\coth(\frac{x}{2})} \tag{4.9}$$

Figure 4.3 shows a typical example of fractional heating in this model. Note that this result is totally independent of temperature, and assumes that phonons are completely absent from the system. So far, deviations in the noise of the type shown here have not been observed, nor should they be at the present level of precision.

4.3 Voltage Drops

Because the SNT relates temperature to a voltage, any errors in the measured voltage lead directly to errors in the temperature measurement. While I have attempted to place the voltage leads as close

to the junction as possible to minimize voltage drops, there is always a finite voltage drop between the junction and the point at which voltage is measured. These voltage drops come from the finite resistance of the metal films that are used for the wiring. Because they lead to a higher measured voltage than the true voltage across the junction, this effect leads to a temperature reading that is higher than the true temperature. In this section I analyze the various voltage drops and evaluate their effect on temperature measurement.

The two potential problems that arise from this effect are that voltage may not be constant over the extent of the junction, complicating the form of the junction noise, and that the voltages in the two films may be different from one another, and may have some voltage drop that leads to an incorrect voltage measurement. The calculations in this section are somewhat lengthy, so I will state their results here before getting into the highly mathematical details. The first of these problems is at a level of tens of parts per millions or smaller, and should be able to be eliminated completely by improved junction design. The second is estimated to be a very important error, and to cause the SNT to read consistently high. I estimate that the fractional size of the temperature error due to voltage drops is approximately 4×10^{-3} at low temperatures.

It may seem strange that there can be a voltage difference between the films in the voltage leads even though no net current flows through them. This can be understood if one imagines that the films that constitute the voltage leads are separate resistive wires which connect to a distant voltage reservoir consisting of the wire bond pad. Although no *net* current flows down the wires in this situation, there is a voltage drop between the ends of the wires and the wire bond pad because the wires act as a voltage divider for a current loop that goes from one film near the junction out to the bond pad and back through the other film. This concept is illustrated in Figure 4.4

The first problem that must be solved to understand the systems to be considered here is that of how current distributes itself between two metal films separated by a barrier. Let the current in the bottom and top films be I_1 and I_2 respectively, and let I be the total current (see Figure 4.5). Also, let λ_1 and λ_2 be the resistance per unit length in Ohms per meter of the bottom and top films respectively, and let σ be the conductance per unit length between the two films in inverse Ohms per meter. All films are treated as one dimensional, with the finite width of the films to be taken into account later.

As can be seen from inspection of figure 4.5, all the current in the top layer must have flowed across the contact between the films at some point. Thus, at any given point at position x, the total

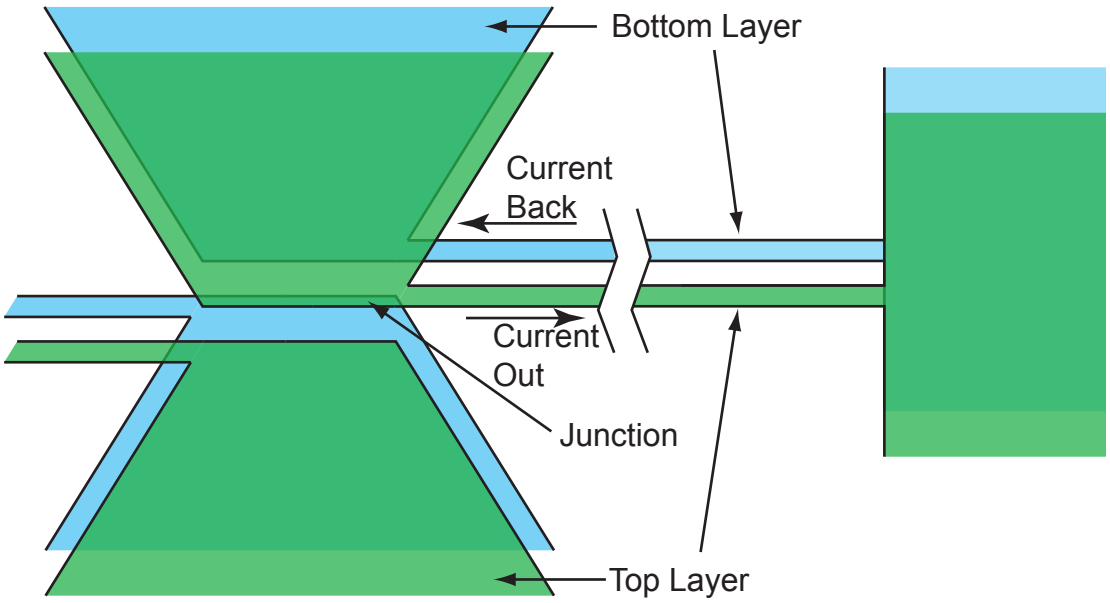

Figure 4.4: This cartoon shows conceptually how there can be a voltage drop in each film in the voltage leads even though there is no net current. This is a simplification, since the device drawn here only has two films, and since they are not in contact at all over the length of the voltage leads. Conceptually, this image is useful, however, since the tunnel barrier effectively separates the different films.

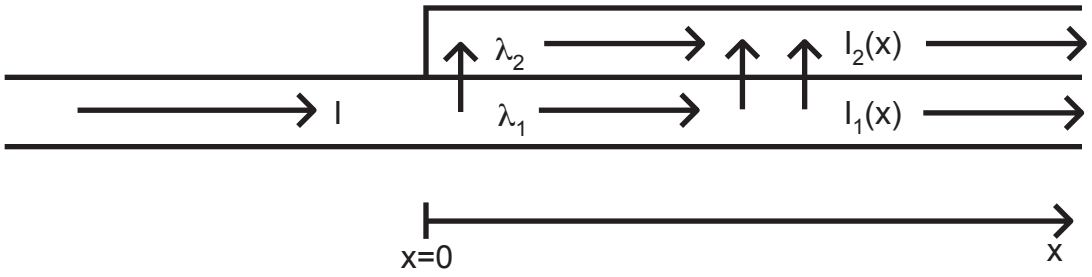

Figure 4.5: Cartoon of current flowing into a pair of metal films. This model is the building block from which the more complex models in this chapter are constructed.

current flowing through the top film may be evaluated by integrating the vertical current through the barrier as follows:

$$I_2 = I_2(0) + \int_0^x \sigma(V_1(x') - V_2(x'))dx', \tag{4.10}$$

where $V_1(x)$ and $V_2(x)$ are the voltages in the bottom and top films respectively at position x. Since the total current must be conserved,

$$I = I_1 + I_2. \tag{4.11}$$

Furthermore, the current at any given point may be evaluated from the voltage gradient as

$$I_{1,2}(x) = -\frac{1}{\lambda_{1,2}}\frac{dV_{1,2}(x)}{dx}. \tag{4.12}$$

Now, differentiating equation 4.12 twice, I arrive at the differential equation

$$\frac{d^2I_2}{dx^2} = \sigma(\lambda_2 I_2 - \lambda_1 I_1). \tag{4.13}$$

Substituting in $I_1 = I - I_2$ from the above equation and simplifying yields

$$\frac{d^2I_2}{dx^2} - \sigma(\lambda_1 + \lambda_2)I_2 + \sigma\lambda_1 I = 0. \tag{4.14}$$

Solutions of this equation are of the form

$$I_2(x) = Ae^{-\sqrt{\sigma(\lambda_1+\lambda_2)}x} + Be^{\sqrt{\sigma(\lambda_1+\lambda_2)}x} + \frac{\lambda_1 I}{\lambda_1 + \lambda_2}. \tag{4.15}$$

From this general solution set, there are two specific boundary conditions that must be applied to understand the voltage drops in the SNT system: those for the junction itself and those for a semi-infinite film on top of an infinite film. I will evaluate the first of these, since it is more general, and the semi-infinte case may be computed as a special case where the junction is infinite in extent.

In the case of the junction of length L, the boundary conditions are that the $I_2(0) = 0$ and $I_2(L) = I$. This pair of boundary conditions leads to the relations $B = Ae^{-\sqrt{\sigma(\lambda_1+\lambda_2)}L}$ and $A+B = -\lambda_1 I/(\lambda_1 + \lambda_2)$, which lead to the general solutions for the currents

$$I_1(x) = \frac{\lambda_1 I}{\lambda_1 + \lambda_2}\left[\frac{\lambda_2}{\lambda_1} + e^{\sqrt{\sigma(\lambda_1+\lambda_2)}x} - \left(\frac{\lambda_2}{\lambda_1} + e^{\sqrt{\sigma(\lambda_1+\lambda_2)}L}\right)\frac{\sinh(\sqrt{\sigma(\lambda_1+\lambda_2)}x)}{\sinh(\sqrt{\sigma(\lambda_1+\lambda_2)}L)}\right] \tag{4.16}$$

and

$$I_2(x) = \frac{\lambda_1 I}{\lambda_1 + \lambda_2}\left[1 - e^{\sqrt{\sigma(\lambda_1+\lambda_2)}x} + \left(\frac{\lambda_2}{\lambda_1} + e^{\sqrt{\sigma(\lambda_1+\lambda_2)}L}\right)\frac{\sinh(\sqrt{\sigma(\lambda_1+\lambda_2)}x)}{\sinh(\sqrt{\sigma(\lambda_1+\lambda_2)}L)}\right]. \tag{4.17}$$

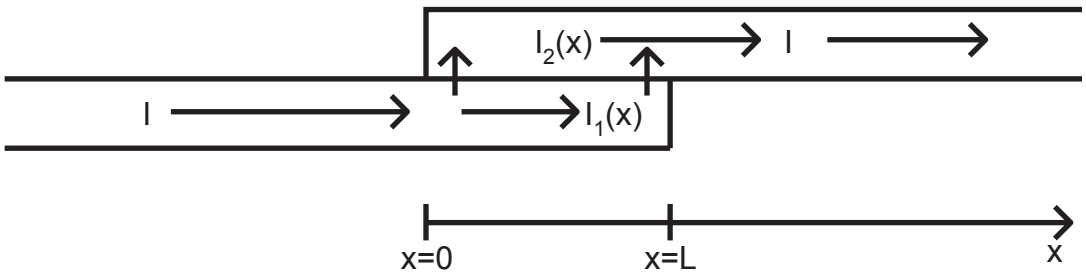

Figure 4.6: Cartoon of current flowing through a junction. In the Dolan Bridge method presently used for junction fabrication, all junctions have this profile at the microscopic level.

Making the assumption that $\lambda_2 = \lambda_1$ gives the simpler expressions

$$I_1(x) = \frac{I}{2}\left[1 + e^{\sqrt{2\sigma\lambda_1}x} - \left(1 + e^{\sqrt{2\sigma\lambda_1}L}\right)\frac{\sinh(\sqrt{2\sigma\lambda_1}x)}{\sinh\left(\sqrt{2\sigma\lambda_1}L\right)}\right] \tag{4.18}$$

and

$$I_2(x) = \frac{I}{2}\left[1 - e^{\sqrt{2\sigma\lambda_1}x} + \left(1 + e^{\sqrt{2\sigma\lambda_1}L}\right)\frac{\sinh(\sqrt{2\sigma\lambda_1}x)}{\sinh\left(\sqrt{2\sigma\lambda_1}L\right)}\right]. \tag{4.19}$$

The case where the top film is semi-infinite is dealt with by letting L go to infinity. In this limit, the currents reduce to

$$I(2) = \frac{\lambda_1 I}{\lambda_1 + \lambda_2}\left(1 - e^{-\sqrt{\sigma(\lambda_1+\lambda_2)}x}\right) \tag{4.20}$$

and

$$I_1(x) = \frac{\lambda_2 I}{\lambda_1 + \lambda_2} + \frac{\lambda_1 I}{\lambda_1 + \lambda_2}e^{-\sqrt{\sigma(\lambda_1+\lambda_2)}x} \tag{4.21}$$

Armed with the full solutions for the currents, I now proceed to compute voltage the as a function of position in the film using the expression

$$V_1(x) = -\lambda_1 \int I_1(x)dx. \tag{4.22}$$

By setting the boundary condition $V_1(0) = 0$, the bottom film voltage is found to be

$$V_1(x) = -I\sqrt{\frac{\lambda}{8\sigma}}\left[x\sqrt{2\sigma\lambda} + e^{\sqrt{2\sigma\lambda}x} - 1 + \left(1 + e^{\sqrt{2\sigma\lambda}L}\right)\frac{1 - \cosh\left(\sqrt{2\sigma\lambda}x\right)}{\sinh\left(\sqrt{2\sigma\lambda}L\right)}\right] \tag{4.23}$$

V_2 may be computed by use of the expression

$$V_2(x) = -\lambda_2 \int I_2(x)dx. \tag{4.24}$$

and the boundary condition

$$I = \sigma \int_0^L [V_1(x) - V_2(x)]dx, \tag{4.25}$$

which yields

$$V_2(x) = -I\sqrt{\frac{\lambda}{8\sigma}}\left[x\sqrt{2\sigma\lambda} - e^{\sqrt{2\sigma\lambda}x} - 1 + \left(1 + e^{\sqrt{2\sigma\lambda}L}\right)\frac{1 + \cosh\left(\sqrt{2\sigma\lambda}x\right)}{\sinh\left(\sqrt{2\sigma\lambda}L\right)}\right] \tag{4.26}$$

I now define lower case normalized voltages $v_{1,2} = \sigma L V_{1,2}/I$ and simplify the expressions containing $\lambda_{1,2}$ to get

$$v_1(x) = -\sqrt{\frac{\sigma\lambda}{8}}L\left[x\sqrt{2\sigma\lambda} + e^{\sqrt{2\sigma\lambda}x} - 1 + \left(1 + e^{\sqrt{2\sigma\lambda}L}\right)\frac{1 - \cosh\left(\sqrt{2\sigma\lambda}x\right)}{\sinh\left(\sqrt{2\sigma\lambda}L\right)}\right] \tag{4.27}$$

and

$$v_2(x) = -\sqrt{\frac{\sigma\lambda}{8}}L\left[x\sqrt{2\sigma\lambda} - e^{\sqrt{2\sigma\lambda}x} - 1 + \left(1 + e^{\sqrt{2\sigma\lambda}L}\right)\frac{1 + \cosh\left(\sqrt{2\sigma\lambda}x\right)}{\sinh\left(\sqrt{2\sigma\lambda}L\right)}\right]. \tag{4.28}$$

These voltages are normalized to the voltage $I/\sigma L$, which is what the voltage would be if $\lambda = 0$. To determine the effect on the SNT of voltage changes in the section of the film in contact with the junction, the relevant quantity to compute is the voltage difference, which is found from the above expressions as follows:

$$v_1(x) - v_2(x) = -\sqrt{\frac{\sigma\lambda}{8}}L\left[2e^{\sqrt{2\sigma\lambda}x} - 2\left(1 + e^{\sqrt{2\sigma\lambda}L}\right)\frac{\cosh\left(\sqrt{2\sigma\lambda}x\right)}{\sinh\left(\sqrt{2\sigma\lambda}L\right)}\right] \tag{4.29}$$

For a realistic junction, $L = 0.5$ μm, $\sigma = 0.04\ \Omega^{-1}\mu\text{m}^{-1}$, and $\lambda = 0.02\ \Omega^{-1}\mu\text{m}^{-1}$. Figure 4.7 shows a plot of $(v_1(x) - v_2(x)) - 1$, which shows the fractional size of this effect. For these values it is in the tens of parts per million level. Thus, in order to get the SNT to an accuracy of single digits of parts per million or better the films must be cleaner or thicker or both. Note that using superconducting leads is not an option, since the noise behavior of a superconducting tunnel junction is totally different and is no longer suitable for thermometry. In order for the maximum deviation of the voltage will be below the part per million level λ must be less than $0.0004\ \Omega^{-1}\mu\text{m}^{-1}$, which corresponds to an $R_\square$ of less than $0.004\ \Omega/\square$. With the SNT device geometry used in this work, this implies an R_{square} for the film of less than $0.004\ \Omega/\square$. Figure 4.8 shows the maximum deviation in the voltage, which is found by taking the difference between the voltage at the middle and at the end, as a function of λ. It should be possible to achieve the needed boundary conditions for sub part per million voltage deviations by fabricating thick trilayer junctions.

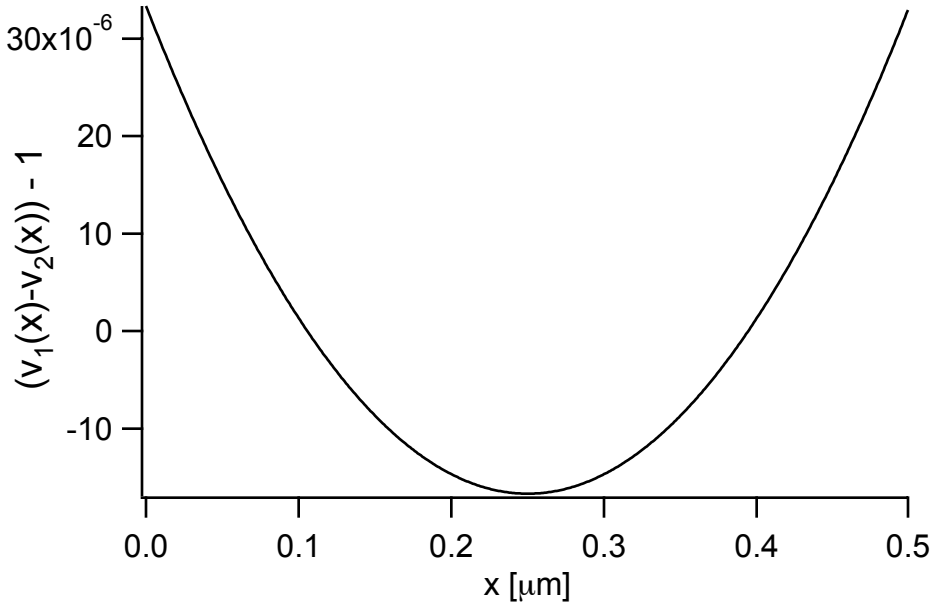

Figure 4.7: Normalized voltage difference across junction as a function of position, for estimated parameters of a typical SNT junction. In the present experiments, this level of voltage deviation is totally insignificant, however, it will need to be reduced if the SNT is ever to be improved to the part per million level.

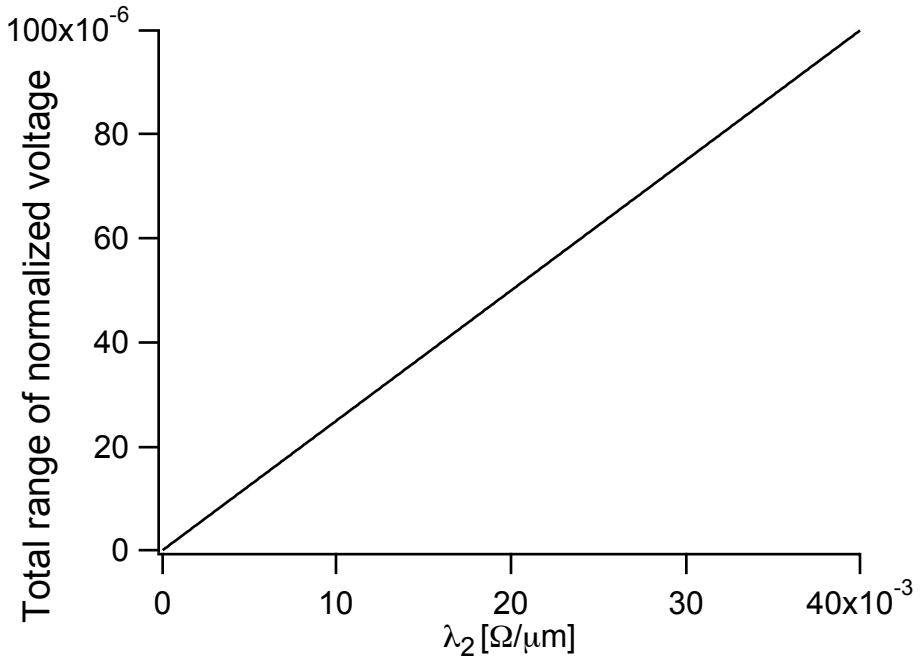

Figure 4.8: Normalized voltage difference between the center and the end of the junction as a function of λ. This shows how making better films would decrease the voltage deviations. As will be shown in the analysis of voltage drops in the voltage leads, there are other more compelling reasons to improve film quality.

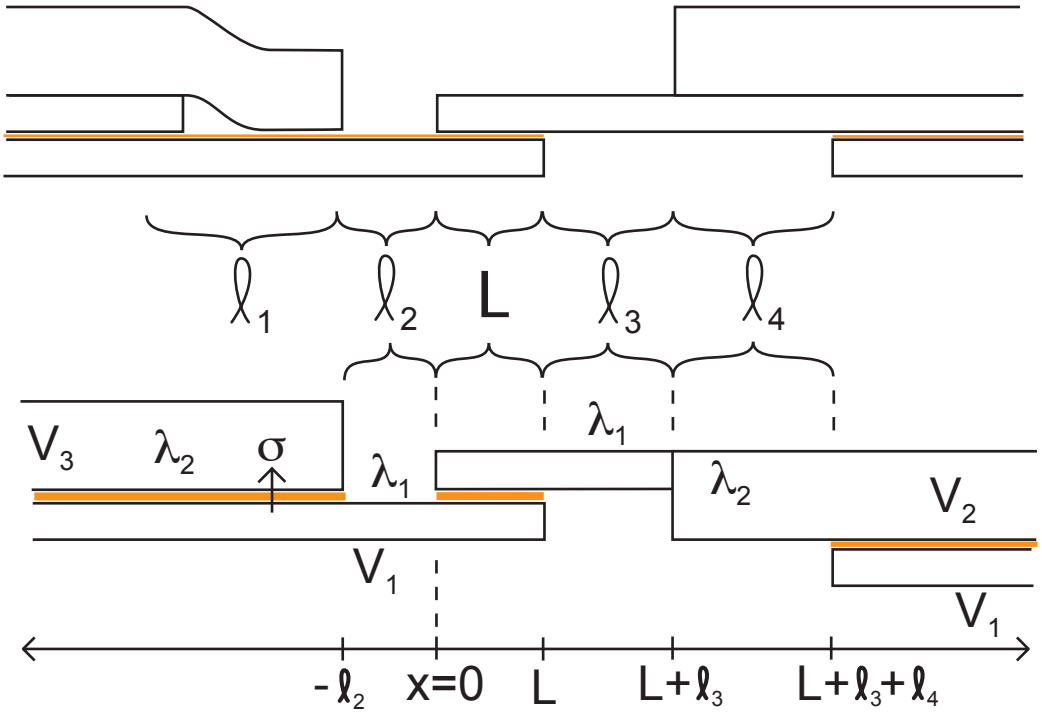

Figure 4.9: Cartoon of full model used to analyze voltage drops in junction. Note that I have made the approximations that the films not separated by an insulating barrier are in perfect contact and that the two aluminum films are identical.

The other, more important effect of voltage drops is from the sections of the films leading away from the junctions. To analyze this situation, I consider the system shown in Figure 4.9, with the simplifications indicated in the figure. This system may then be analyzed using repeated applications of the general solutions for a pair of films found above.

By using the boundary conditions that all voltages must be equal at infinity and applying the formulas found above, the voltages in the lower model in Figure 4.9 are found to be

$$v_1(x) = \begin{cases} \frac{\lambda_1\lambda_2\sigma L}{\lambda_1+\lambda_2}\left[-(x+l_2)+\frac{\lambda_1}{\lambda_2}\frac{1}{\sqrt{\sigma(\lambda_1+\lambda_2)}}\left(1-e^{\sqrt{\sigma(\lambda_1+\lambda_2)}(x+l_2)}\right)\right]+\lambda_1 l_2\sigma L, \\ \qquad\qquad \text{for} \quad x<-l_2 \\ -\lambda_1\sigma L x, \\ \qquad\qquad \text{for} \quad -l<x<0 \\ -\sqrt{\frac{\lambda_1\sigma}{8}}L\left[x\sqrt{2\sigma\lambda_1}+e^{\sqrt{2\sigma\lambda_1}x}-1+\left(1+e^{\sqrt{2\sigma\lambda_1}L}\right)\frac{1-\cosh\left(\sqrt{2\sigma\lambda_1}x\right)}{\sinh\left(\sqrt{2\sigma\lambda_1}L\right)}\right], \\ \qquad\qquad \text{for} \quad 0<x<L \\ v_2(L+l_3+l_4)-\frac{\lambda_1\lambda_2\sigma L}{\lambda_1+\lambda_2}\left[x-L-l_3-l_4+\frac{\left(\frac{\lambda_2}{\lambda_1}+e^{-\sqrt{\sigma(\lambda_1+\lambda_2)}(x-L-l_3-l_4)}\right)}{\sqrt{\sigma(\lambda_1+\lambda_2)}}\right] \\ \qquad\qquad \text{for} \quad L+l_3+l_4<x \end{cases} \tag{4.30}$$

$$v_2(x) = \begin{cases} -\sqrt{\frac{\lambda_1\sigma}{8}}L\left[x\sqrt{2\sigma\lambda_1} - e^{\sqrt{2\sigma\lambda_1}x} - 1 + \left(1+e^{\sqrt{2\sigma\lambda_1}L}\right)\frac{1+\cosh\left(\sqrt{2\sigma\lambda_1}x\right)}{\sinh\left(\sqrt{2\sigma\lambda_1}L\right)}\right], \\ \qquad\qquad\qquad\qquad \text{for} \quad 0 < x < L \\ v_2(L) - (x-L)\lambda_1\sigma L \\ \qquad\qquad\qquad\qquad \text{for} \quad L < x < L + l_3 \\ v_2(L+l_3) - (x-l_3-L)\lambda_2\sigma L \\ \qquad\qquad\qquad\qquad \text{for} \quad L + l_3 < x < L + l_3 + l_4 \\ v_2(L+l_3+l_4) - \frac{\lambda_1\lambda_2\sigma L}{\lambda_2+\lambda_1}\left[x - L - l_3 - l_4 + \frac{\lambda_2}{\lambda_1}\frac{\left(1-e^{-\sqrt{\sigma(\lambda_1+\lambda_2)}(x-L-l_3-l_4)}\right)}{\sqrt{\sigma(\lambda_1+\lambda_2)}}\right] \\ \qquad\qquad\qquad\qquad \text{for} \quad L + l_3 + l_4 < x \end{cases} \tag{4.31}$$

$$v_3(x) = \frac{\lambda_1\lambda_2\sigma L}{\lambda_1+\lambda_2}\left[-(x+l_2) + \frac{1}{\sqrt{\sigma(\lambda_1+\lambda_2)}}\left(\frac{\lambda_1}{\lambda_2} + e^{\sqrt{\sigma(\lambda_1+\lambda_2)}(x+l_2)}\right)\right] + \lambda_1 l_2\sigma L \qquad \text{for } x < -l_2. \tag{4.32}$$

I have made the approximation that the intermediate film has little effect on the voltage on the left hand side, and that the conductance between adjacent layers with no insulating barrier is infinite. To get realistic estimates of the voltages, I can examine atomic force microscope images of the junctions to get the various dimensions, and use various $R_\square$ measurements made on films from the evaporator in which these devices were made.

Once the voltages in the various films are computed, the voltages that are measured by the voltage leads may be estimated. To find these voltages, the above analysis of voltage as a function of position is repeated for a pair of films through which zero total current flows. If the resistance per unit length of the bottom film is λ_1 and the top film is λ_2, and if the voltages in the films are $V_1(x)$ and $V_2(x)$, and the voltages at the end are defined to be $V_1(0) = 0$ and $V_2(0) = V_0$ then the voltages are

$$V_1(x) = \frac{V_0\lambda_1}{\lambda_1+\lambda_2}\left(1 - e^{\sqrt{\sigma(\lambda_1+\lambda_2)x}}\right) \tag{4.33}$$

and

$$V_2(x) = \frac{V_0\lambda_1}{\lambda_1+\lambda_2}\left(1 + e^{\sqrt{\sigma(\lambda_1+\lambda_2)x}}\right). \tag{4.34}$$

Since the voltage leads are hundreds of micrometers long, the voltages converge to the value $V_0\lambda_1/(\lambda_1+\lambda_2)$.

The deviation of the measured voltage from the actual voltage on the device may now be estimated using these formulas and results. The asymptotic voltage drop on the left hand side is very close to the full voltage difference shown on the left hand side of Figure 4.11, since the film in contact with the junction represents the higher resistance film in this case. On the right hand

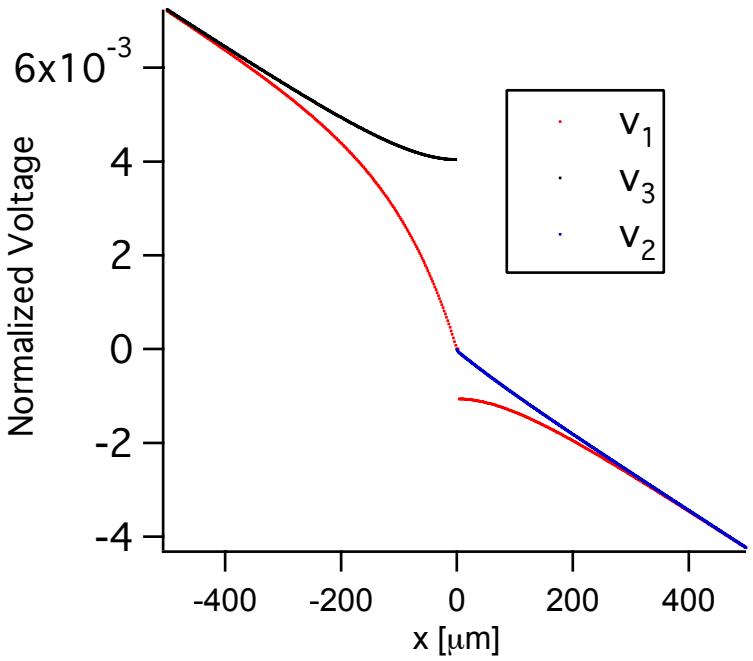

Figure 4.10: Normalized voltages over a large range, assuming that the leads are of constant width and infinite length. An offset of 1 has been subtracted from one side in order to show all voltages on the same scale.

side, the opposite is true, and the asymptotic voltage at the junction. A good approximation is thus to take the total added voltage drop to be the voltage drop computed for the left hand side near the junction, which is about 4×10^{-3}. This fractional error in voltage will remain constant as long as the properties of the films remain constant. The estimates used here assume the measured film properties of the aluminum films from below 4 kelvin, however these films have been measured to have approximately 4 times higher resistance at room temperature, which should increase the size of this effect. These estimates are approximate, and the appropriate course of action for future work is to simply change the design of the junctions to eliminate this as an error. This could be accomplished with the use of trilayer junction technology.

4.4 Effect of Noise on the Voltage Bias

If there is noise on the bias voltage across the junction, it can smear out the shape of the noise curve, leading to high temperature readings. In this section I analyze in detail the effect of a given amount of Gaussian noise on the bias voltage, as well as that of a sinusoidal oscillation. While the

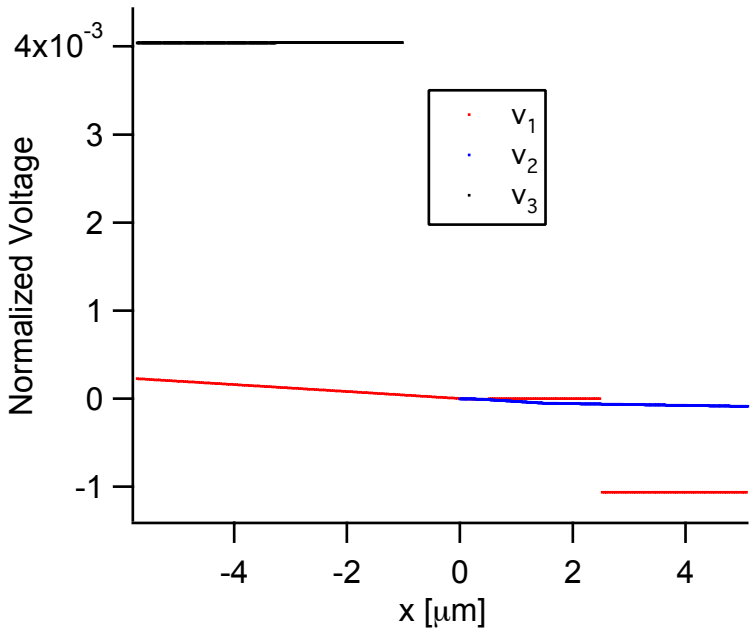

Figure 4.11: Normalized voltages over a small range, assuming that the leads are of constant width and infinite length. This is a voltage zoom of the plot shown in Figure 4.10.

effect of noise from the environment on SNT measurements can be eliminated by careful filtering, it is worth noting that the environmental noise can have a more profound effect on the third moment of the current, as was recently described by work by Reulet et al. [60, 61].

I first assume that the voltage bias has some noise described by the probability density function

$$f(V) = \frac{1}{\sigma\sqrt{2\pi}} e^{-\frac{(V-V_0)^2}{2\sigma^2}}, \tag{4.35}$$

where V_0 is the intended bias voltage. If the noise curve to be measured in the presence of a perfect bias would be

$$\frac{2eV}{R} \coth\left(\frac{eV}{2k_BT}\right), \tag{4.36}$$

then the actual measured noise curve is

$$S_I(V_0,\sigma) = \int_{-\infty}^{\infty} \frac{1}{\sigma\sqrt{2\pi}} e^{-\frac{(V-V_0)^2}{2\sigma^2}} \frac{2eV}{R} \coth\left(\frac{eV}{2k_BT}\right) dV. \tag{4.37}$$

I now convert this to normalized units, using the normalized variables $x = eV/k_BT$, $r = e\sigma/k_BT$ and $s = RS_I/4k_BT$, and get normalized noise of

$$s(x) = \int_{-\infty}^{\infty} \frac{1}{r\sqrt{2\pi}} e^{\frac{(x'-x)^2}{2r^2}} \left(\frac{x'}{2}\right) \coth\left(\frac{x'}{2}\right) dx', \tag{4.38}$$

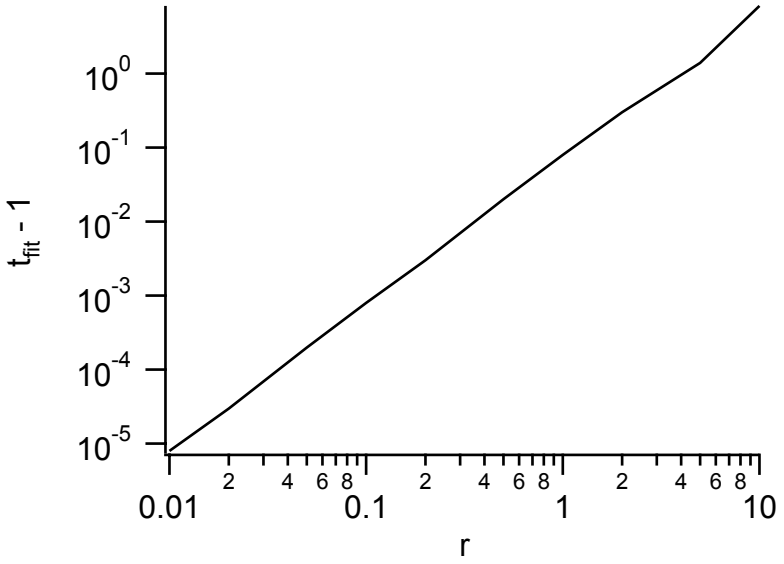

Figure 4.12: Plot of fractional temperature error caused by gaussian noise on the voltage bias as a function of normalized standard deviation r.

The Gaussian has no effect on the linear regime of the noise curve, and exponentially suppressed effect on the normalized voltages far from the intended bias. Thus it is sufficient to analyze only normalized voltages between -10 and 10 and to only integrate from $x - 10r$ to $x + 10r$. With this analysis, I compare the measured normalized noise as a function of normalized voltage for various normalized bias noise amplitudes r, by evaluating the integrals numerically using Igor Pro. This function can then be fit to the function

$$s(x, G, t) = G\frac{x}{2t}\coth\left(\frac{x}{2t}\right). \tag{4.39}$$

The deviation of the fit parameter t from is equal to the fractional error in the temperature caused by excess Gaussian noise of standard deviation r. Figure 4.12 shows a plot of this deviation as a function of r.

If the main source of voltage noise on the junction at temperature T_{cold} is the Johnson noise from a bias resistor or resistance R at temperature T_{hot}, than the normalized bias noise r is

$$r = 2e\sqrt{\frac{RBT_{hot}}{k_B T_{cold}^2}}. \tag{4.40}$$

Thus, for a 100 Ohm bias resistor at 4 K an experiment at 10 mK, and a bandwidth of 1 MHz, r = 0.17, and the fractional effect on the noise should be approximately a part in 10^3. Assuming the

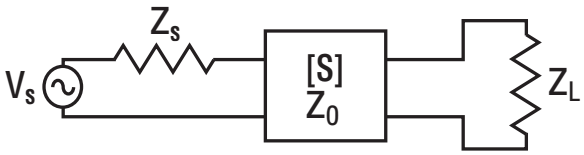

Figure 4.13: This figure illustrates the model used here, and it shows the variables in the analysis below. The S-matrix shown is considered to be a black box whose parameters do not depend on voltage.

same bias resistors, r is proportional to the inverse of the sample temperature, so for 500 mK, r = 0.0034 and the fractional effect on the temperature fit is less than a part per million. This shows the importance of filtering for the SNT. The filter used to eliminate excess noise from the SNT is described in Chapter 7.

4.5 Changing Impedance of the RF Measurement Circuit

in this discussion, the junction is considered to be a noise signal V_S in series with a changing impedance Z_S coupled to a load impedance through some network characterized by the S-matrix S, as shown in Figure 4.13. The S-matrix is considered to be a black box for the purpose of this discussion, and is including the various surface mount components, wire bonds, and wiring which connect the RF line to the junction.

Pozar [56] derives an equation for the power P_L delivered by the source voltage V_S to the load Z_L:

$$P_L = \frac{|V_S|^2}{8Z_0}\frac{|S_{21}|^2(1-|\Gamma_L|^2)|1-\Gamma_S|^2}{|1-S_{22}\Gamma_L|^2|1-\Gamma_S\Gamma_{in}|^2}, \tag{4.41}$$

Where $\Gamma_L = \frac{Z_L-Z_0}{Z_L+Z_0}$, $\Gamma_S = \frac{Z_S-Z_0}{Z_S+Z_0}$, $\Gamma_{in} = \frac{Z_{in}-Z_0}{Z_{in}+Z_0}$, and Z_{in} and Z_0 are the input impedance of [S] and the reference impedance of [S] respectively. Since Z_0 is fixed, only Γ_S in the above expression depends on the changing impedance $Z_S = R_{junction}$, and so one may combine all other terms into the overall frequency dependent gain term G(f). So, if the junction makes V_S noise voltage, the power delivered to the load is

$$P_L = G(f)|V_S|^2\frac{|1-\Gamma_S(V)|^2}{|1-\Gamma_{in}\Gamma_S(V)|^2}. \tag{4.42}$$

Since Z_S can be measured accurately via DC measurements, Γ_S is known. For any given frequency, then, there is a single fit parameter Γ_{in}, which is independent of voltage and which must

be determined. Perhaps this can be extracted as a fit parameter for a given fixed frequency by just feeding it into a least squares fit. Also, in the limit as Γ_{in} goes to zero, the voltage dependent gain simplifies to a known expression $|1-\Gamma_S(V)|^2$. Hence the best strategy is to just make this term as small as possible by picking the right frequency.

Computing the voltage dependence of the power coupling from the junction is only half of what is needed to correct for the changing impedance Z_S. The other problem is to account for the changing added noise that gets reflected off of the device. There are two factors that add to the noise temperature that depend on device impedance. The first is the noise from Z_L that gets reflected back, through [S], off of the device, and back through [S] to the load. This involves some noise temperature for Z_L that gets multiplied by a gain which we can measure by sending a signal into the circulator and measuring what comes back as a function of frequency. This type of noise should be easy to characterize, since the gain is measurable and the noise temperature is easy to estimate, or can be a constant fit parameter. The other type of noise that depends on the junction impedance is noise from the lossy elements of [S] which reflects off of the junction, goes back through [S] and gets coupled onto Z_L. This term is extremely difficult to measure or compute. Probably the best strategy for dealing with this term is to try to minimize loss between the device and the circulator, and try to find ways to just get it below some threshold below which it doesn't matter.

So now an expression for the total noise power coupled onto Z_L can be written as

$$P_L = G(f)|V_S|^2 \frac{|1-\Gamma_S(V)|^2}{|1-\Gamma_{in}\Gamma_S(V)|^2} + H(f,V)T_N^{Z_L} + I(f,V)T_N^{[S]}, \tag{4.43}$$

where $T_N^{Z_L}$ is the noise temperature of the load impedance, $T_N^{[S]}$ is the noise temperature of the lossy elements in [S], and H and I are gains. One may assume that $I(f,V)T_N^{[S]}$ is small enough to neglect, and measure H by sending signals down the third port of the circulator.

Now, note that $|V_S(V)|^2 = S_I(V)R_J^2(V)$, and the tic-toc power may be defined as

$$\begin{aligned} p_L(V) &= P_L(V) - P_L(0) \\ &= G(f)\left[S_I(V)R_J^2(V)\frac{|1-\Gamma_S(V)|^2}{|1-\Gamma_{in}(f)\Gamma_S(V)|^2} - 4k_BTR_J(0)\frac{|1-\Gamma_S(0)|^2}{|1-\Gamma_{in}(f)\Gamma_S(0)|^2}\right] \\ &+ T_N^{Z_L}(H(f,V)-H(f,0)). \end{aligned} \tag{4.44}$$

Up to a constant factor that gets absorbed into $T_N^{Z_L}$ one can measure $(H(f,V)-H(f,0))$ by feeding a signal into the third port of the circulator. Other than that, the only new fit parameter is

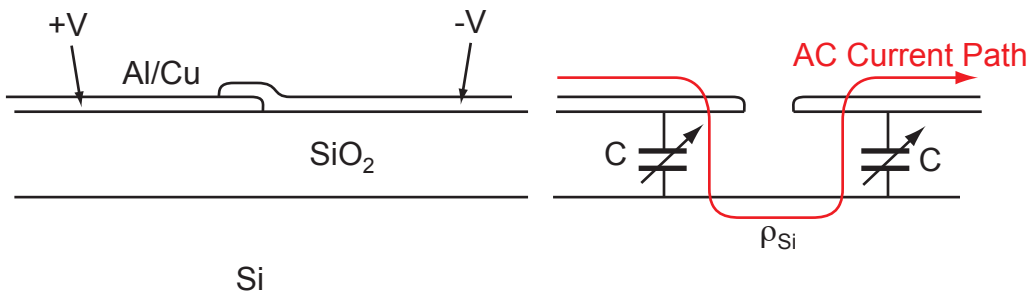

Figure 4.14: Schematic diagram showing how the SNT junction acts as a metal-oxide-semiconductor capacitor. The left inset shows the real geometry of an SNT junction and the right inset shows how this acts as a variable AC shunt.

$\Gamma_{in}(f)$. Thus, an algorithm has been found for fitting data with a varying impedance junction.

4.6 Variable Substrate Leakage

At high bias and high temperatures, it is possible for the silicon in the substrate to have radio frequency losses that are gated by the junction leads, leading to a voltage-dependent effect in the noise.

The metal of the voltage and current leads, the oxide coating on the silicon and the bulk silicon below form a metal oxide semiconductor (MOS) capacitor, which has been studied in detail because of its relevance to the MOS field effect transistor. As with all systematic effects in the SNT, it is not the size of the effect that is of concern, but rather the fractional *change* with voltage of the effect. In this system, that change comes from the changing capacitance between the silicon substrate and the metal leads. The RF noise being measured can be coupled through these capacitors from one lead into the substrate and back into the other lead, creating a voltage-dependent shunt path around the junction. Johnson noise from the substrate may also be coupled in via these capacitors with a similar voltage dependence.

In practice, it is possible to use high enough resistivity silicon for the substrate to make this a negligible effect. In this section I will both describe a simple model and experiments with support this claim.

The capacitance of a metal-oxide semiconductor structure such as the one described here is the series combination of the oxide capacitance and the capacitance of the depletion region. It is the

latter of these that depends on voltage. From page 54 of reference [51], the total capacitance per unit area is

$$C = \frac{C_0}{\sqrt{1 + \frac{2C_0^2 V_g}{eN_A \epsilon_s \epsilon_0}}}, \tag{4.45}$$

where C_0 is the capacitance per unit area of the oxide, V_g is the bias voltage applied, e is the charge on an electron, N_A is the acceptor density, ϵ_s is the relative dielectric constant of silicon, and ϵ is the permittivity of free space. The capacitance per unit area of the oxide is

$$C_0 = \frac{\epsilon_{Ox}\epsilon_0}{d}, \tag{4.46}$$

where d and ϵ_{Ox} are the thickness and relative dielectric constant, respectively, of the oxide. For a typical wafer, the oxide is about a half a micron thick, and the relative dielectric constant of SiO_2 is about 3, so $C_0 \approx 50$ μF/m^2. For a typical acceptor concentration of 10^{21} m^{-3} and a typical resistivity of 1 kΩ-cm, the total capacitance per unit area is approximately $C \approx 50$ μF/m$^2(1 - 0.03V_g)$. Since the maximum voltage ever needed for the SNT at room temperature is about 0.25 V, the maximum fractional deviation of the shunt capacitance is less than 1 percent. Thus as long as the shunt path passes less than 1 percent of the total noise current, the total fractional size of the effect is less than a part in 10^4 at room temperature at the maximum voltage range. This is much lower than the present level of fractional uncertainty of the SNT at room temperature. In the range where more accurate SNT work has been done, below 30 K, the voltages are a factor of 10 smaller and the resistivity of the silicon becomes very large as carriers are frozen out. Also, the high accuracy work I did in this work was all with wafers with greater than 20 kΩ-cm resistivity, adding bringing the fractional effect down by more than another order of magnitude. Thus even if there were a few percent current shunt at room temperature, below 30 K the total fractional change in noise current due to the MOS capacitor should be at the sub-ppm level.

In addition to the above plausibility argument, I have measured the RF throughput of a sample with no DC connection as a function of DC bias voltage over a large range in voltage. An optical image of the device used is shown in figure 4.15. I wire bonded the leads of this device to microstrip lines which were coupled to coaxial cables connected to a network analyzer and varied the bias on the junction using a commercial bias tee. The results of that measurement are shown in figure 4.16. This measurement was done with the lower resistivity wafers, which are approximately 1 KΩ-cm resistivity. When the throughput in the the above plot is converted to linear units and fit to a line through zero bias, the throughput is found to be about 350 ppm + 1.8 ppm(V_{bias}), meaning that

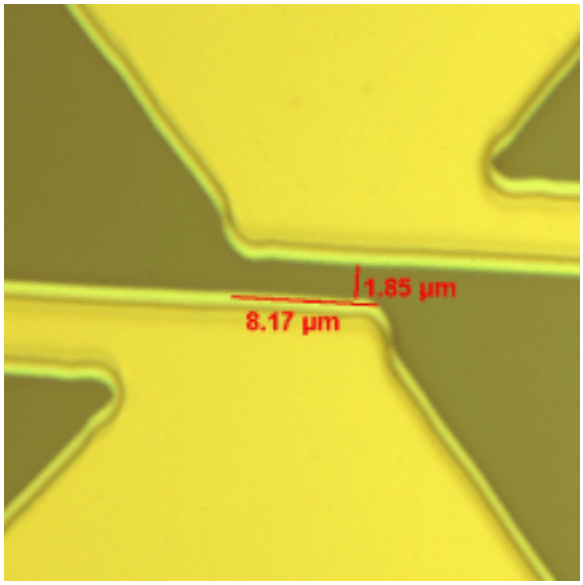

Figure 4.15: Optical microscope image of device used in test. The geometry is identical to the SNT junctions used in the other experiments described here, but there was no overlap of the films and so no direct current connection.

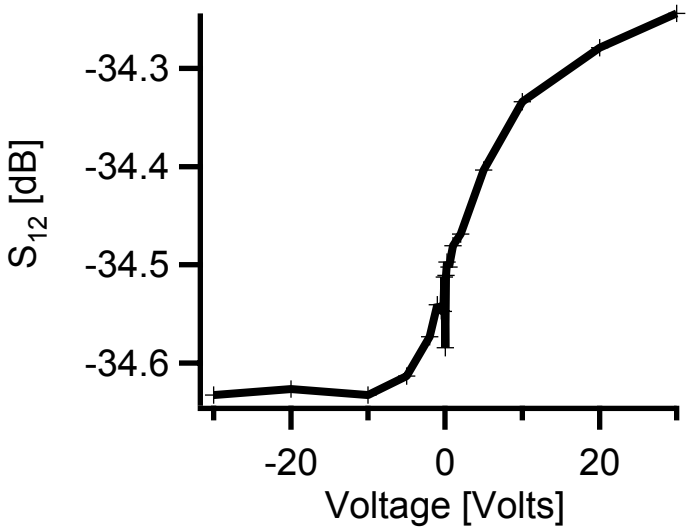

Figure 4.16: RF throughput of open device as a function of DC bias voltage.

even at room temperature over the largest needed voltage range the fractional effect is sub-ppm. For the higher resistivity wafer, it should be in the part per billion range.

4.7 Linearity of RF Chain

No measurement system is perfectly linear. In practice, the measured power is always a nonlinear function of the input power, and can be written as a Taylor expansion of the input power. In a noise measurement, the final stage of the measurement is generally the voltage output from a diode. If the measured voltage is $V_{measured}$ and the voltage that would be measured if the diode were perfectly linear is V_{linear} then the measured voltage may be approximated as

$$V_{measured} = V_{linear} + \beta V_{input}^2, \tag{4.47}$$

where β is measured in inverse volts and is a parameter that characterizes the nonlinearity of the measurement. The quantitative effect of this nonlinearity will be discussed in the chapter on the details of the least squares fit, in the section on the effect of an arbitrary nonlinearity on the temperature fit.

It is very difficult to get an accurate measurement of β, since there is a lack of RF instrumentation of any kind with high absolute accuracy in attenuation of power. One approach I took to getting a rough estimate of β was to put a pair of step attenuators in series with the measurement, right before the diode. One attenuator could be varied in steps of 10 dB and the other one in steps of 1 dB, and by stepping the attenuators and measuring the output on the diode, the nonlinearity of the diode could be estimated. This setup is shown in Figure 4.17.

Another way to measure nonlinearity is to connect the output of a RF generator directly into an RF measurement chain and measure the voltage at the output of the diode as a function of power from the generator. This method gives voltage as a function of power on the diode in real power units, although the stated power values from the generator are also not very linear. I performed this experiment on the DZM020BBP diode that was used for all the data in this work. Comparisons of measured power with a linear response of this diode are shown in Figure 4.18 and Figure 4.19.

Both methods are imprecise, and the values of β depend on the range of power over which the fit was performed. The values measured ranged over a factor of 2 from approximately 3 V^{-1} to 6 V^{-1}. This is sufficient, however, to estimate the order of magnitude of this effect. In practice, the best way to deal with this potential source of error is to decrease the dynamic range of the experiment

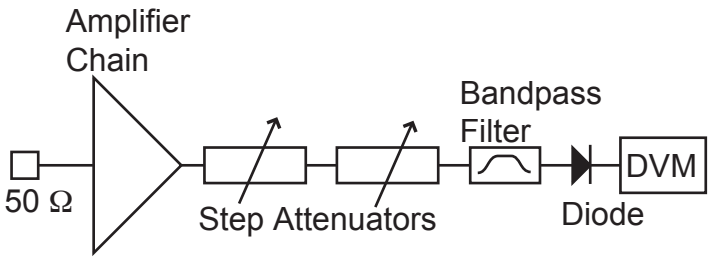

Figure 4.17: Schematic diagram showing how step attenuators are used to measure the nonlinearity of the diode.

until the nonlinearity is so low that it cannot effect the fit temperature.

4.8 Finite Frequency Corrections

Although the finite frequency corrections to the SNT have already been discussed theoretically in Chapter 3, it is worth taking the time at this point to estimate the size of these corrections quantitatively. As an approximation to get numerical estimates, I assume that gain is determined by taking data at two points at high enough bias that frequency is not important, and that a single point recorded at zero bias determines the measured temperature. As stated in Chapter 3, the current spectral density of the noise at zero voltage bias is

$$S_I(f) = \frac{2}{R} hf \coth\left(\frac{hf}{2k_B T}\right). \tag{4.48}$$

The fractional correction to the temperature due to finite frequency may then be computed as follows:

$$\frac{\delta T}{T} = \frac{S_I(f) - S_I(0)}{S_I(0)} = \frac{hf}{2k_B T} \coth\left(\frac{hf}{2k_B T}\right) - 1. \tag{4.49}$$

This function may be taylor expanded around zero for temperatures much larger than hf/k_B to get

$$\frac{\delta T}{T} \approx \frac{x^2}{12} + O(x^4), \tag{4.50}$$

where $x = hf/k_B T$, and $O(x^4)$ is a term of order x^4. Thus, as mentioned in Chapter 3, the fractional correction in temperature is proportional to the inverse square of temperature for fixed frequency.

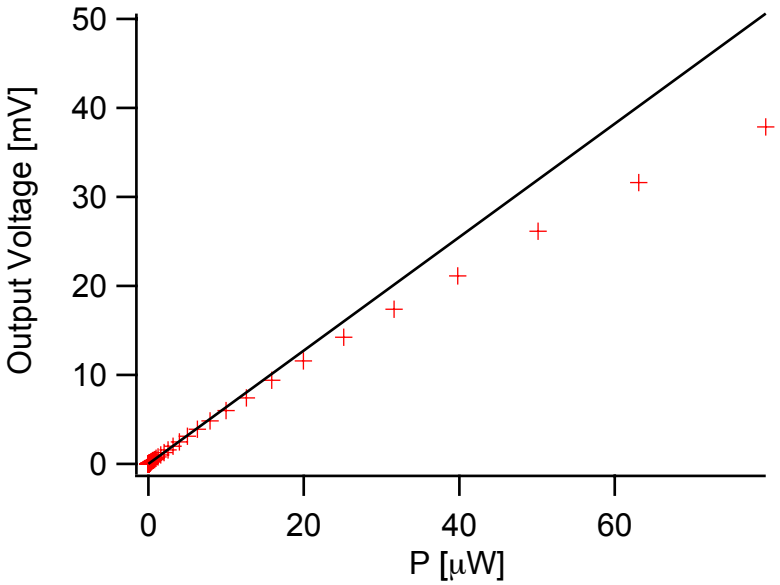

Figure 4.18: Diode voltage as a function of linear power as determined from a power sweep from an RF generator.

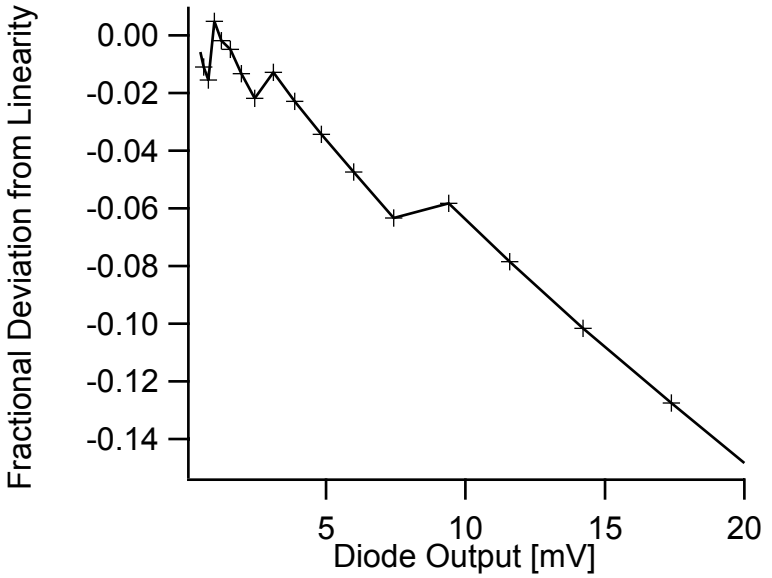

Figure 4.19: Fractional deviation from linear extrapolated line. Note that this should be linear, but that there are glitches at certain power levels. These represent the switching of the generator between different power ranges, and they demonstrate the difficulty of achieving accurate and linear RF power calibrations.

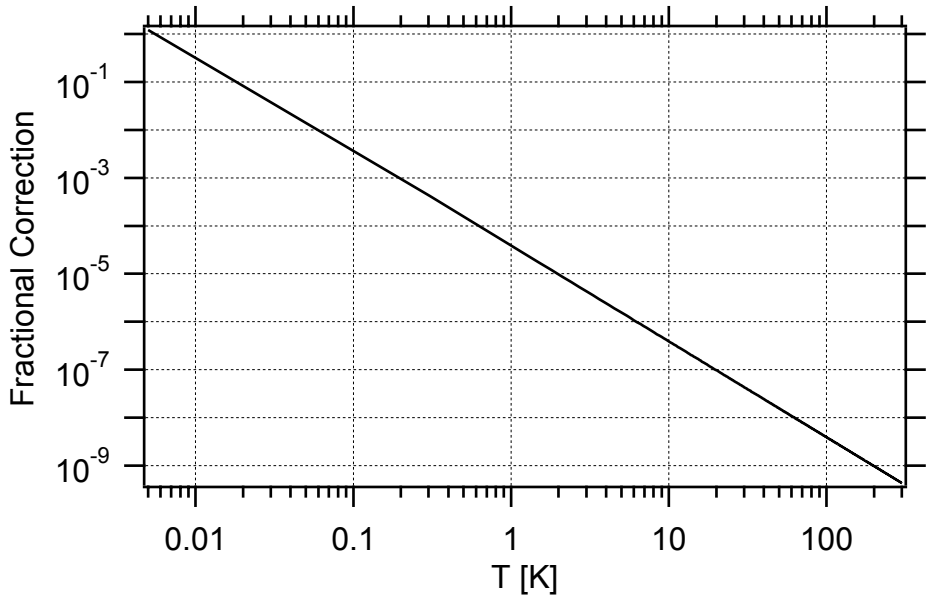

Figure 4.20: Fractional correction to temperature as a function of temperature, for a fixed measurement frequency of 450 MHz. 450 MHz corresponds to a hf/k_B temperature of 21.6 mK.

4.9 Voltage Offsets and Voltmeter linearity

Offsets are always a potential problem in sensitive voltage measurements. Voltage offsets may arise from contacts between different metals and from thermal voltages from temperature gradients. The presence of small voltage offsets does not affect the operation of the SNT, as long as both positive and negative voltage points are recorded. The voltage offset may then be found accurately from a fit of the noise data, with no effect on the determination of the fit temperature. Slow drifts in the voltage offset are not harmful as long as they are on the voltage lines and not the current bias lines. These kinds of drifts would be removed by the same digital lock-in technique that is used to eliminate the effect of RF amplifier drifts. Observed voltage offsets from fits are typically less than 20 nV, and are constant with time to within the statistical accuracy with which they are known. It is necessary to use some care in the wiring to achieve this low offset level, however.

In order to minimize offsets, all DC leads are as symmetric as possible twisted pair all the way from the room temperature electronics on the experiment rack down to the actual junction. This wiring scheme is discussed in detail in later chapters. This symmetry is extremely important, since in an asymmetric low temperature measurement the thermal offsets can bet in the hundreds of μV and can change from one run to the next. While this level of offset could be dealt with in principle,

it adds an unnecessary level of complexity to the experiment and it is better to just avoid it with twisted pair wiring.

Another potential source of error is any kind of nonlinearity or inaccuracy in the voltmeter used to record the voltage across the junction. Since the SNT relates temperature directly to voltage, any fractional errors in the voltmeter translate exactly to errors in the temperature measurement. This means that using any kind of amplifier before the voltmeter will generally degrade the accuracy. While the best amplifiers can be linear to a part in 10^4, 0.1 % or worse is more typical, and amplifiers generally have offsets that drift as well as drifting gain. A good rule of thumb is that for better than 1 % accuracy temperature measurement, a DC amplifier should not be used in the bias measurement.

The nonlinearities of the voltmeters are negligible. The nonlinearity of the analog to digital conversion on the HP 34420A nanovoltmeter is specified at 0.8 ppm of the reading plus 0.5 ppm of the range. For the Keithley 2000 multimeter, the nonlinearity is specified at 2 ppm of the reading plus 1 ppm of the range. In both cases this is small compared to the voltage accuracy available on the meters and compared to the highest accuracy to which the SNT has been measured so far.

4.10 High Frequency Radio Interference

While having a very large bandwidth is excellent for the speed of a noise measurement, it introduces the potential problem of picking up RF signals in the entire band being measured. In this section, I describe the effect of these signals, as well as how they are characterized and eliminated.

A constant RF signal added on top of the base noise signal simply adds to the noise temperature of the measurement, which in principle only affects the integration time and not the accuracy of the SNT measurement. In practice, the signals picked up are almost never constant. The band used in this work is generally somewhere between 250 MHz and 1 GHz, and there is an enormous variety of communications systems that use these frequencies, and which are often intermittent and totally unpredictable in their behavior. An added signal which varies randomly with time leads to glitches in the noise data which can severely limit the ultimate accuracy of the SNT. One of the most important steps in getting an SNT experiment to work is making sure that these signals are eliminated, and constant vigilance is required to make sure that they do not leak in to the experiment at any time.

Figure 4.21 shows just how severe the pickup problem can be. This figure shows what happens to the SNT measurement when totally unshielded, unfiltered leads are connected. Although the bias tee attenuates these high frequency signals, when the DC leads are totally exposed and unfiltered,

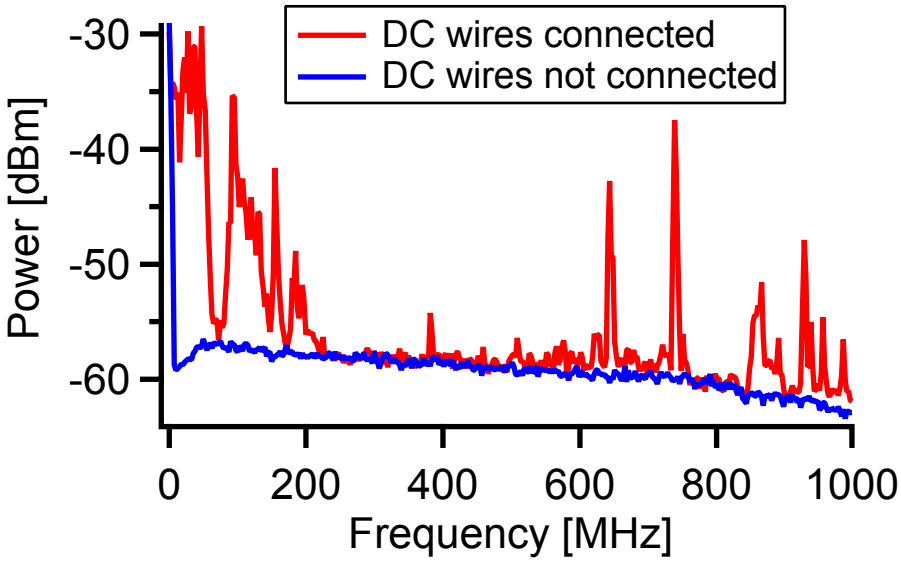

Figure 4.21: Noise spectrum from SNT with unfiltered, unshielded DC lines connected and disconnected. When the DC lines are unfiltered and are left in an unshielded environment, they act as antennas and pick up a vast array of radio stations.

they act as antennas, and are extremely effective at coupling in signal power, which still ends up reaching the device. Filtering and shielding are discussed in great detail later in this thesis. For now, I will discuss how the signals are found and eliminated assuming that the filtering problem has been solved on the DC lines.

Figure 4.22 shows the typical effect of an intermittent RF signal being picked up in an SNT setup with proper filtering a shielding on the DC lines. When this happens, it is useful to identify the location of the signal to make sure it is really RF pickup and not a problem with a cable or amplifier. This is done by examining the signal with a spectrum analyzer and integrating to look for peaks, which are generally small. Figure 4.23 shows one such signal, the same one that caused the glitches shown in the time domain in figure 4.22. To make absolutely sure that the signal on the spectrum analyzer is causing the time domain glitches, it is useful to put the spectrum analyzer into zero span mode on the peak and record a time series of the IF output on a voltmeter to see if the glitching behavior is the same as for the broadband noise signal.

Once the exact frequency of a signal is known, its source can be determined using the Federal Communications Commission (FCC) website at the address http://wireless.fcc.gov/uls. From this site, by clicking on “search licenses” and then on “advanced license search”, one gets to a site where

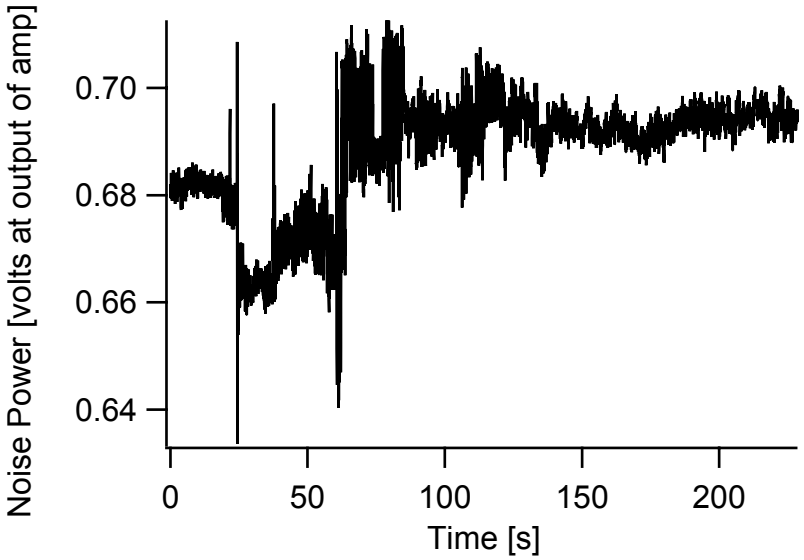

Figure 4.22: Time series of broadband noise data with a single frequency intermittent RF signal coupled in through the power supply wires of the cold amplifier.

one enters the frequency of a signal and ones location and the relevant information is displayed about the signal. The location may be either a zip code or just a city, and the frequency can be either an exact frequency or a range of frequencies. The site gives the exact location of the transmitting antenna, the power of the signal, as well as the contact information for the owner of the license. The exact location of the antenna is given in latitude and longitude coordinates, with a precision of a tenth of an arc second, which is about 3 meters. These coordinates may be put into the map software on the website http://www.topozone.com/viewmaps.asp to find where it is on a map. This can be very convenient for locating a particularly troublesome noise source.

The signal displayed in Figures 4.22 and 4.23 caused problems for quite some both in my experiment and in other broadband noise experiments done by Minghao Shen in the same lab before its source was discovered. The source was the base station for the mobile radios used by the Yale physical plant staff. This base station consists of a massive antenna on the roof of the Payne Whitney Gym, approximately 500 meters from our lab, in direct line of sight from the cryostats. Figure 4.24 shows the antenna as seen out the window of our lab building as well as a map showing the position of the antenna relative to the building. It turned out that this signal was getting in to the RF line along with the measured noise signal via the DC bias lines to the cryogenic amplifier, which do not have built in filtering. Careful shielding and filtering of these lines and adding more shielding to the

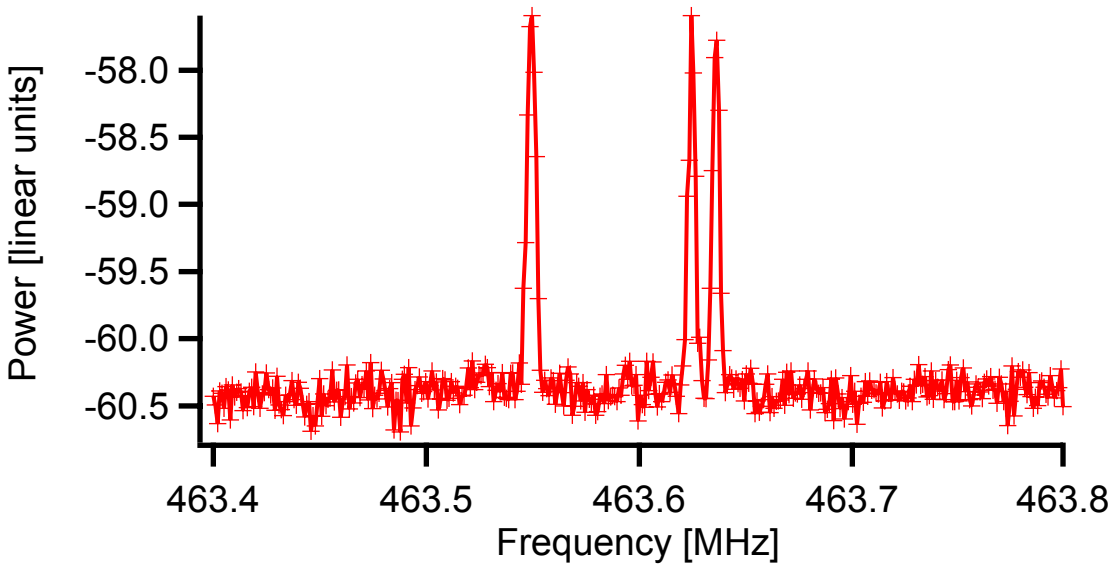

Figure 4.23: Spectrum of intermittent signal from physical plant communications system. This signal has caused the majority of RF interference related problems in our lab.

top of the cryostat attenuated this signal to unmeasurable levels.

In addition to the external source of a noise signal, it is important to know just how the signal is getting into the measurement chain, so that it may be eliminated. This is done using a microwave leak checking apparatus as shown in Figure 4.25. With this apparatus, a microwave signal in the middle of the amplifier band is amplitude modulated at an audible frequency, and the output of the RF measurement chain is rectified and amplified and put into a speaker to make an audible tone. The volume of the tone is proportional to the power coupling into the experiment, and by moving the position of the antenna around, the exact location of RF leaks can be found. These are generally found to be at various wiring feedthroughs, both on the wires themselves and at the various o-ring seals around the feedthroughs. The leaks around o-ring seals can be plugged by wrapping the metal with copper mesh and clamping it around the available tubes with hose clamps. The leaks through unused DC lines were plugged with screw caps. This process has proven to be effective in the unshielded part of the lab. Proper use of a shielded room eliminates these effects.

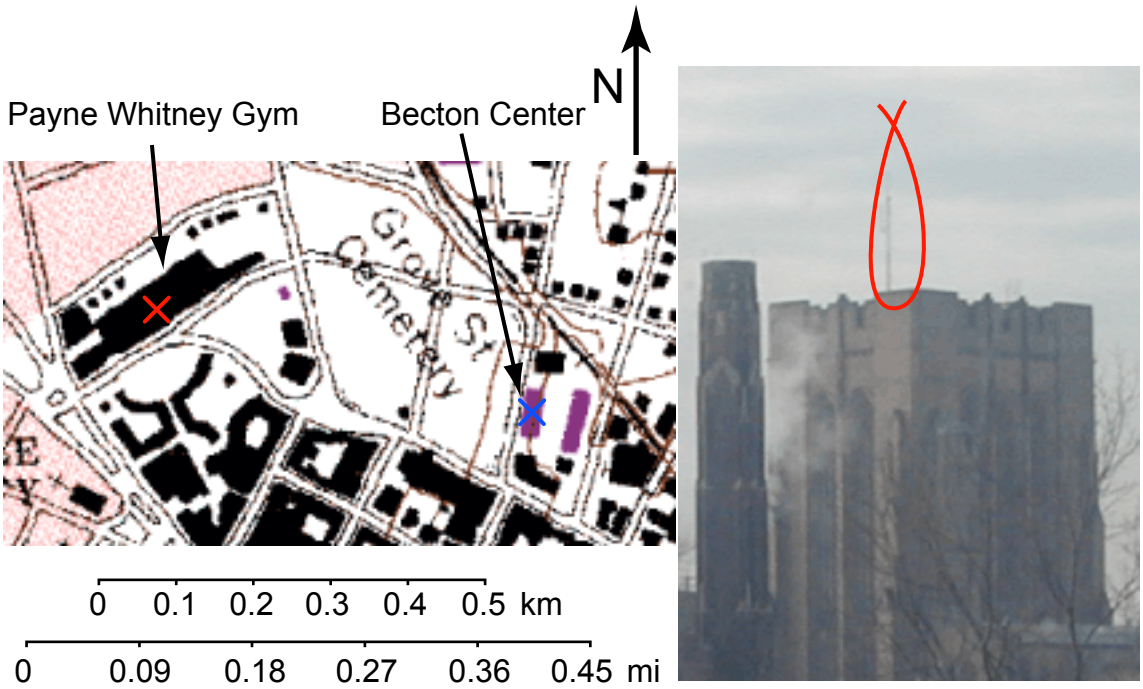

Figure 4.24: Left inset displays Topozone map showing location of Becton Center, where our lab is located and the Payne Whitney Gym, where the source of the physical plant signal is. The blue "x" shows the location of our lab and the red "x" shows the location of the antenna. The right inset shows the antenna as seen from becton looking across the Grove Street Cemetery. The antenna is about 500 meters away, and is directly visible through the window from the top of the cryostat. The antenna is circled in red in the photograph.

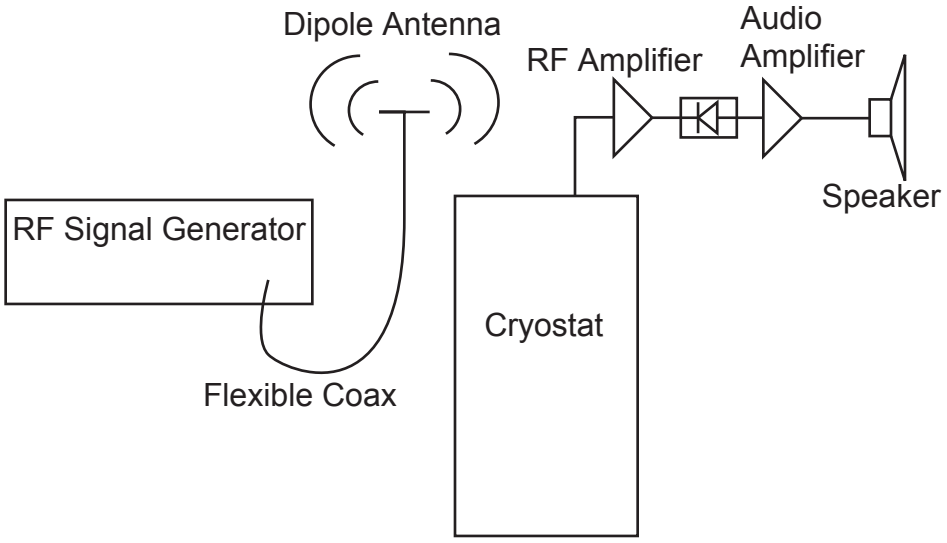

Figure 4.25: Schematic of RF leak checking setup. By moving the dipole around to different parts of the cryostat, the exact physical location of RF leaks into the system may be found and eliminated. While this is not a quantitative measure of pickup, it is extremely effective for pinpointing leaks.

4.11 Drift of RF Chain

The gain and noise temperature of RF amplifiers drift with time. The digital lock-in technique used in this work removes slow drift by making all measurements as differences between noise signals close to each other in time. Typical overnight gain and noise temperature drifts are shown in Figure 4.26. The gain and noise temperature of amplifiers generally depends on the physical temperature of the amplifier. Since the cryogenic amplifiers used as the first stage in the SNT measurements are generally sitting in the middle of the liquid helium bath, as the liquid helium level gets lower, the temperature changes and the amplifier characteristics change, as seen in the figure.

Note that in spite of the gain and noise temperature changing by more than on percent, the measured physical temperature of the SNT stays constant. The average of many noise signals with different gains $\{G^1, G^2, ..., G^N\}$ and noise temperatures $\{T_N^1, T_N^2, ..., T_N^N\}$ is

$$P = \frac{1}{N}\sum_{i=1}^{N} G^i \left[T_N^i + \frac{eV}{2k_BT}\coth\left(\frac{eV}{2k_BT}\right)\right], \tag{4.51}$$

which still has exactly the standard SNT form, with only the gain and nose temperature modified by the drift.

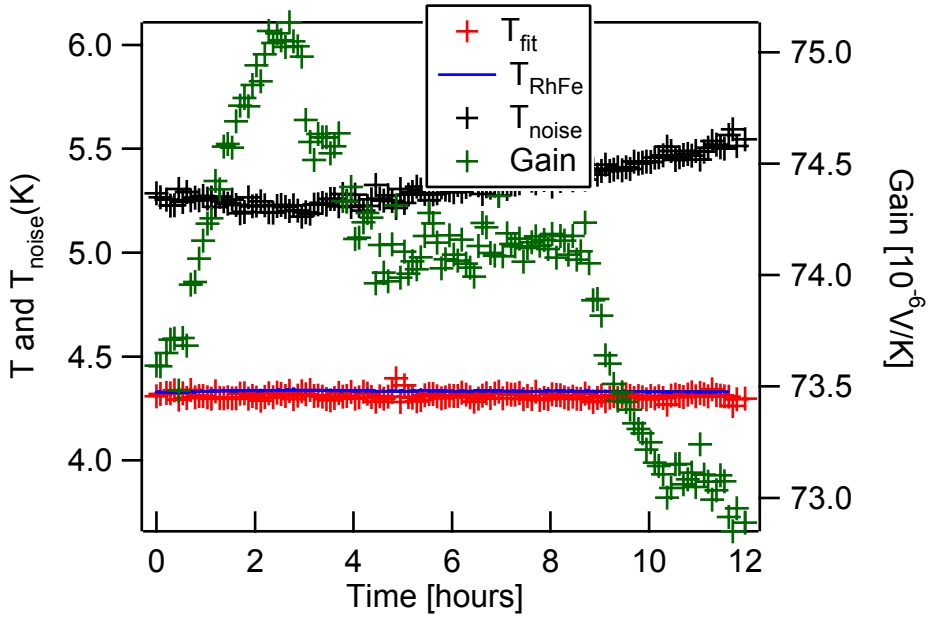

Figure 4.26: This figure shows typical drift of gain and noise temperature overnight, plotted along with SNT fit temperature and the temperature as measured by a rhodium iron thermometer. Note that while the amplifier parameters drift, the SNT fit temperature stays fixed, demonstrating the independence of the SNT fit temperature on amplifier parameters.

These drifts are not relevant to the SNT measurement as long as they are slow compared to the 10-30 ms time scale of the digital lock in chop frequency. That this is the case can be seen from the fact that the noise integrates down to below 50 ppm fractional statistical uncertainty in a way consistent with white noise statistics. These measurements are described in the data chapter of this thesis.

4.12 Conclusions

This chapter has covered a very wide range of systematic effects, some of which are of critical importance to SNT operation, and some of which are of almost no importance. The experimentalist who wishes to estimate or improve upon SNT accuracy must have a comparison of the sizes of those effects which are experimentally measurable. It is also important to know what the sign is of each effect, so that, for instance, one may reasonably discard as an explanation a systematic that always leads to a high temperature reading when the SNT is reading consistently low. The most important systematic effects are voltage drops near the junction that lead to voltage errors, nonlinearity of

Table 4.1: Table of estimates of present sizes of various systematic effects.

Temperature	Statistics	Changing Junction Impedance	Linearity of RF Chain	Voltage Drops	Frequency Corrections
10 mK	± 2 %	± 3×10^{-4}	-5×10^{-7}	+0.4 %	+32%
500 mK	± 400 ppm	± 3×10^{-4}	-2.5×10^{-5}	+0.4 %	+155 ppm
13 K	± 50 ppm	± 3×10^{-4}	-5×10^{-4}	+0.4 %	+230 ppb
300 K	± 50 ppm	± 1-10 %	-5×10^{-4}	+0.4 %	+0.43 ppb

the RF measurement apparatus, and the changing resistance of the junction. Some of these depend strongly on the temperature at which the measurement is performed. The following Table shows estimates of these effects. Note that while the effect of finite frequency corrections can be as high as 32 % for the lowest temperatures measured, or higher if higher measurement frequencies were used, this effect can be accurately corrected for, in principle to arbitrary accuracy. Voltage drops are difficult to estimate, because it is difficult to get accurate estimates of the film parameters as a function of temperature, and the exact dimensions of the junction which help determine the size of this effect vary from device to device. The effect of changing impedance is also very difficult to estimate accurately. The coupling between the device and the circuit depends on frequency, in general, and the number in this table is estimated from the magnitude of the change in SNT fit temperature at very different frequencies at 13 K. The temperatures below 13 K are estimated by assuming that the effect decreases linearly with temperature. The sign of the effect can depend on frequency, on the particular choice of junction and on the stray inductances and capacitances in the system. The 300 K result is simply the observed error, since this effect clearly dominates at that temperature.

The overarching message of this analysis is that for metrological applications the SNT device desing needs to be improved and for temperatures above 1 K the effects of the changing impedance must be investigated experimentally with more detail than I had time for in this investigation. These, along with a deeper understanding of the physics of shot noise, are the main tasks which face future experimenters who wish to apply the SNT to temperature metrology.

Chapter 5

The Least Squares Fit

5.1 Introduction

The temperature from the SNT is generally computed as a fit parameter in a least squares fit to a two dimensional data set. This leads to the questions of what choice of bias points is optimal for the most accurate possible temperature measurement in a given amount of time how statistical uncertainty in individual points affects statistical uncertainty in temperature measurement, and how nonlinearities in the noise curve affect measured temperature. This chapter consists of a theoretical analysis of these three problems.

5.2 Optimization of Bias Point Choice

In order to extract a temperature from the SNT it is necessary to apply a fit to a set of ordered pairs of voltages and noise powers. A detailed analysis of this fitting process is useful both because it indicates the optimal number and choice of voltage sampling points and because it indicates the potential problems that arise from the least squares fit. In this Section, I use the tools of differential geometry to analyze χ^2 surfaces in order to gain insight into the least squares fit, and in order to derive formulas which can be used to solve arbitrary problems in choice of bias points.

Throughout this analysis, I consider all voltages to be normalized to temperature, and denote them by $x = eV/k_BT$. I also consider all noise powers to have the zero-bias noise subtracted, removing the effect of system noise temperature. Initially, I will also neglect the effect of voltage offsets. Thus, the problem at hand is to sample points $\{x, p\}$ of the function

$$p(x) = \left[\left(\frac{x}{2}\right)\coth\left(\frac{x}{2}\right) - 1\right] + N(x), \tag{5.1}$$

where N(x) is a Gaussian random variable with standard deviation σ, and attempt to apply a fit to the data set selected. The data are compared against the fit function

$$f(x, G, t) = Gt\left[\left(\frac{x}{2t}\right)\coth\left(\frac{x}{2t}\right) - 1\right], \tag{5.2}$$

Where G and t represent the normalized gain and temperature, respectively. For any given data set corresponding to the sample points $\{x_1, ..., x_n\}$, I compute the reduced χ^2 function [7]

$$\chi^2 = \frac{\Sigma_{i-1}^{n}(p(x_i) - f(x_i, G, t))^2}{\sigma^2(n-2)}. \tag{5.3}$$

The task of a least squares fit is then to find the values of G and t that minimize χ^2 for a given data set. Since for any given data set $\chi^2(G, t)$ describes a two surface over the G,t plane, this problem can be restated as a differential geometry problem of finding the lowest point on this surface. The techniques of differential geometry can prove to be very effective in systematically finding minima and evaluating the shape of those minima. Quite a bit can be learned by considering data sets with $N(x) = 0$ and examining the surface described above.

The first important question to ask about this process is whether or not the solution is unique, that is whether or not there are local minima of the χ^2 surface other than the global minimum at $(G, t) = (1, 1)$. Let N(x) go to zero. Since $\chi^2(G, t)$ consists only of squared real numbers, $\chi^2(G, t) \geq 0$ for all G and t, and it is zero at $(G, t) = (1, 1)$. Therefore what is required here is to show that $\chi^2(G, t) > 0$ for all other G and t values, assuming nonzero choices of x. Consider some noise curve corresponding to $(G, t) \neq (1, 1)$. It can be seen by inspection that the curve intersects the $(G, t) = (1, 1)$ curve either only at zero or at zero and two points equidistant from zero. Thus as long as the voltage points sampled include at least two points other than $x = 0$ there will definitely be a point at which the square of the difference between the two noise curves is greater than zero, leading to a greater than zero χ^2. The only way for there to be more than one point with zero difference between the curves is for the curves to be identical, in which case χ^2 is zero for all choices of x. So $(G, t) = (1, 1)$ is both a local and global minimum of $\chi^2(G, t)$.

Finding the least squares fit for a given data set can be likened to allowing a ball to roll down a surface, where the low point of the surface is the coordinate of the minimum χ^2. It is worth taking the time at this point to look at what these surfaces look like for the typical SNT data set, and how the choice of points qualitatively affects the shape of the surface.

Figure 5.1 shows what a typical χ^2 contour looks like. Zoomed out, it looks like a valley, but zoomed in, the bottom of the valley has a roughly parabolic shape, giving the bottom region a

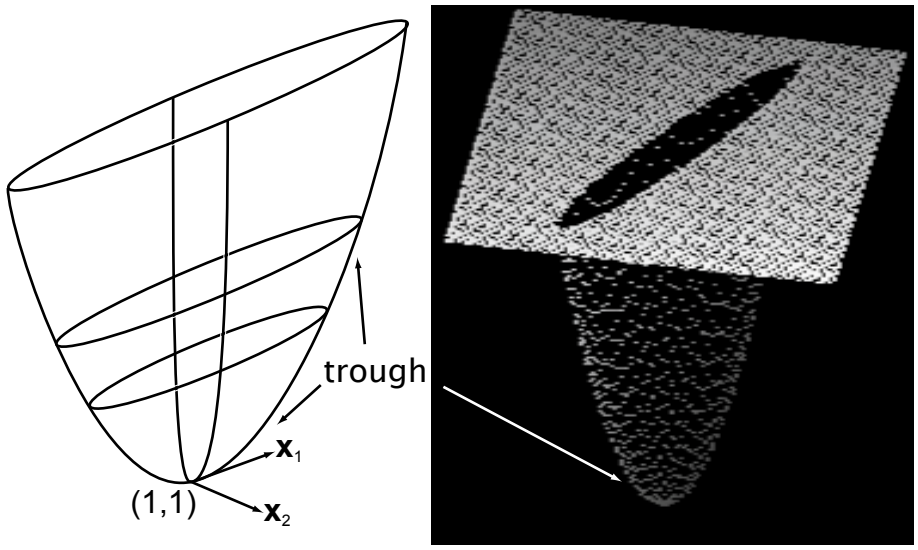

Figure 5.1: The right inset is a three dimensional surface plot showing qualitatively the shape of a typical χ^2 surface. Values have been truncated to show detail near the global minimum. This inverted Portuguese man of war shape is typical of all plots, regardless of the choice of points. The important changes are in the second derivative of the curves through the global minimum along the axis of the trough. For a poor choice of points, this second derivative can approach zero, constraining the product of G and t but not t by itself. The left inset shows the principal directions and the corresponding curves along the trough and perpendicular to the trough.

Portuguese man of war shape. The angle of the bottom trough may be found using the techniques of differential geometry, and then by approximating the curve along the bottom of the trough as a parabola the intersection of the trough with any given χ^2 contour may be computed. By finding the intersections with the $\chi^2 = 1$ contour and projecting onto the t axis, the uncertainty σ_t in t can be found.

The direction along the trough from the point $(1, 1)$ is the direction of minimum Gauss curvature. The directions of maximum and minimum Gauss curvature are called the principal directions, and the curvatures are called the principal curvatures. These directions and curvatures are the eigenvectors and eigenvalues, respectively, of the differential of the Gauss map [12]. The Gauss map, N, maps points on a surface into the unit sphere, with the direction of the normal vector at that point corresponding to the position of the image on the sphere. The differential of the Gauss map for a given pair of coordinates is

$$dN \begin{pmatrix} G \\ t \end{pmatrix} = \begin{pmatrix} a_{11} & a_{12} \\ a_{21} & a_{22} \end{pmatrix} \begin{pmatrix} G \\ t \end{pmatrix}. \tag{5.4}$$

The coefficients in the above matrix are found from the first and second fundamental forms as

follows:

$$\begin{aligned} a_{11} &= \tfrac{fF-eG}{EG-F^2} \\ a_{12} &= \tfrac{gF-fG}{EG-F^2} \\ a_{21} &= \tfrac{eF-fE}{EG-F^2} \\ a_{22} &= \tfrac{fF-gE}{EG-F^2}, \end{aligned} \tag{5.5}$$

where the coefficients E,F and G are from the first fundamental form and e,f, and g are from the second fundamental form. The first fundamental form is found as follows:

$$\begin{aligned} E &= \left(\tfrac{\partial\chi^2}{\partial G}\right)^2 + 1 \\ F &= \tfrac{\partial\chi^2}{\partial G}\tfrac{\partial\chi^2}{\partial t} \quad , \\ G &= \left(\tfrac{\partial\chi^2}{\partial t}\right)^2 + 1, \end{aligned} \tag{5.6}$$

and, since χ^2 is a minimum at (1,1), the first derivatives are zero, which leads to

$$E = G = 1, F = 0 \tag{5.7}$$

at (1,1). The second fundamental form at (1,1) is found as follows:

$$e = \begin{vmatrix} 1 & 0 & \frac{\partial\chi^2}{\partial G} \\ 0 & 1 & \frac{\partial\chi^2}{\partial t} \\ 0 & 0 & \frac{\partial^2\chi^2}{\partial G^2} \end{vmatrix} = \frac{\partial^2\chi^2}{\partial G^2}, \tag{5.8}$$

$$f = \begin{vmatrix} 1 & 0 & \frac{\partial\chi^2}{\partial G} \\ 0 & 1 & \frac{\partial\chi^2}{\partial t} \\ 0 & 0 & \frac{\partial^2\chi^2}{\partial G\partial t} \end{vmatrix} = \frac{\partial^2\chi^2}{\partial G\partial t}, \tag{5.9}$$

$$g = \begin{vmatrix} 1 & 0 & \frac{\partial\chi^2}{\partial G} \\ 0 & 1 & \frac{\partial\chi^2}{\partial t} \\ 0 & 0 & \frac{\partial^2\chi^2}{\partial t^2} \end{vmatrix} = \frac{\partial^2\chi^2}{\partial t^2}. \tag{5.10}$$

This is enough information to re-write the differential of the Gauss map explicitly in terms of G and t as follows:

$$\begin{pmatrix} a_{11} & a_{12} \\ a_{21} & a_{22} \end{pmatrix} = \begin{pmatrix} -e & -f \\ -f & -g \end{pmatrix} = \begin{pmatrix} -\frac{\partial^2\chi^2}{\partial G^2} & -\frac{\partial^2\chi^2}{\partial G\partial t} \\ -\frac{\partial^2\chi^2}{\partial G\partial t} & -\frac{\partial^2\chi^2}{\partial t^2} \end{pmatrix}. \tag{5.11}$$

The eigenvalues of this operator yield the principle curvatures

$$k_1 = \frac{1}{2}\left(e+g+\sqrt{e^2+4f^2-2eg+g^2}\right), k_2 = \frac{1}{2}\left(e+g-\sqrt{e^2+4f^2-2eg+g^2}\right). \tag{5.12}$$

The eigenvectors yield the negatives of the principle directions as follows:

$$\mathbf{x}_1 = \begin{pmatrix} \frac{1}{2f}\left(e-g+\sqrt{e^2+4f^2-2eg+g^2}\right) \\ 1 \end{pmatrix}, \mathbf{x}_2 = \begin{pmatrix} \frac{1}{2f}\left(e-g-\sqrt{e^2+4f^2-2eg+g^2}\right) \\ 1 \end{pmatrix}. \tag{5.13}$$

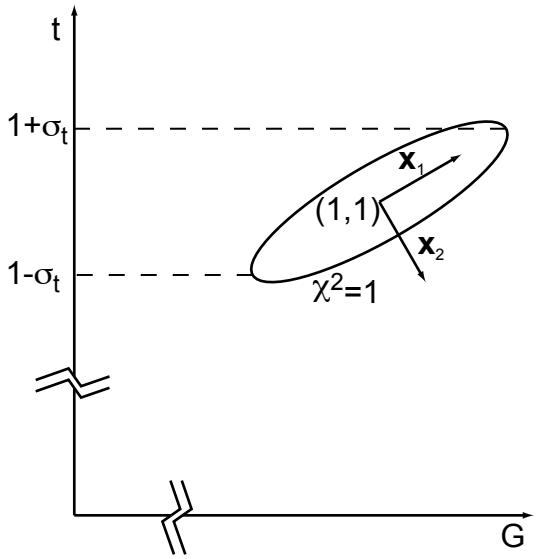

Figure 5.2: Geometry of model in Gt plane. This diagram shows the principal directions, the $\chi^2 = 1$ contour, and the statistical uncertainty in temperature in the approximation described in the text, σ_t. Note that this is not exactly the true uncertainty, but that as long as the aspect ratio of the contour is very high, the approximation is good. This figure is not drawn to scale.

Since the second derivatives of χ^2 at (1,1) are always positive, and since the square root is always positive, the second eigenvalue and eigenvector correspond to the curvature along the trough and the direction of the trough of the χ^2 surface, respectively. The projection of the bottom of the trough onto the G,t plane can be approximated as a line of slope $2f/\left(e - g - \sqrt{e^2 + 4f^2 - 2eg + g^2}\right)$ going through the point (1,1). Above this line, χ^2 may be approximated as a parabola centered around (1,1), where the coefficient of the parabola is found from the first principal curvature above. From the expression from this parabola, the points where the trough intersects the $\chi^2 = 1$ contour may be found, and the distance along the t axis of these points from (1,1) gives a good estimate of the statistical uncertainty in t σ_t, which is the key parameter in this discussion.

If the direction along the trough is parameterized by the variable s, and s is set to 0 at the point (1,1) then the parabolic approximation of χ^2 along the trough is

$$\chi^2 = \frac{k_2}{2} s^2, \tag{5.14}$$

so the values of s for which $\chi^2 = 1$ are

$$s = \pm\sqrt{\frac{2}{k_2}}. \tag{5.15}$$

Finally, from some simple trigonometry,

$$\sigma_t = \sqrt{\frac{2}{k_2\left[1+\left(\frac{e-g-\sqrt{e^2+4f^2-2eg+g^2}}{2f}\right)^2\right]}}. \tag{5.16}$$

This expression is found to be within 2 percent of the exact σ_t for a wide variety of circumstances. This expression, combined with the expressions above for e, f and g gives a very fast way to compute the fractional statistical temperature uncertainty for a given selected set of normalized voltage points. This allows for rapid comparisons of different point choices, from which the optimal choice may be found. With these analytical tools in hand, I may now proceed to evaluate the optimal choice of voltage points.

The first question to ask about point selection is whether more is better. In other words, whether for a fixed amount of wall clock time which may be distributed between the integration time on some number of points what the optimal number of points is to minimize the statistical uncertainty. I have used the above formulas, codified in Igor Pro scripts, to generate theoretical plots on of uncertainty for fixed wall clock time. Figure 5.3 shows how uncertainty decreases with increasing number of points. Note that while more points is slightly better for a fixed wall clock time (assuming a 100 % duty cycle), an order of magnitude more points only improves uncertainty by about a factor of two, so this is a very slowly improving function, and the penalty for only using two points instead of tens of points is not severe.

The next question is, if only two non-zero points are to be used, where the middle point should go. This can once again be answered by using the above formulas. Figure 5.4 shows how the temperature uncertainty depends on position of the smaller of the two points in a two point measurement. Not surprisingly, the optimal location for the smaller of the two points is half way between the larger of the two points and zero. This is the mode of data acquisition I used for taking SNT time series, and would be the mode that would probably be used in a practical commercial implementation of the SNT.

5.3 Statistical Error Propagation

For the purpose of this analysis I assume that data are taken in a sequence $\{0, V_1, 0, V_2, 0, V_1, 0, V_2, ...\}$, where V_1 and V_2 are voltages that are high enough multiples of k_BT/e to be on the almost linear part of the shot noise curve. The corresponding measured noise values are

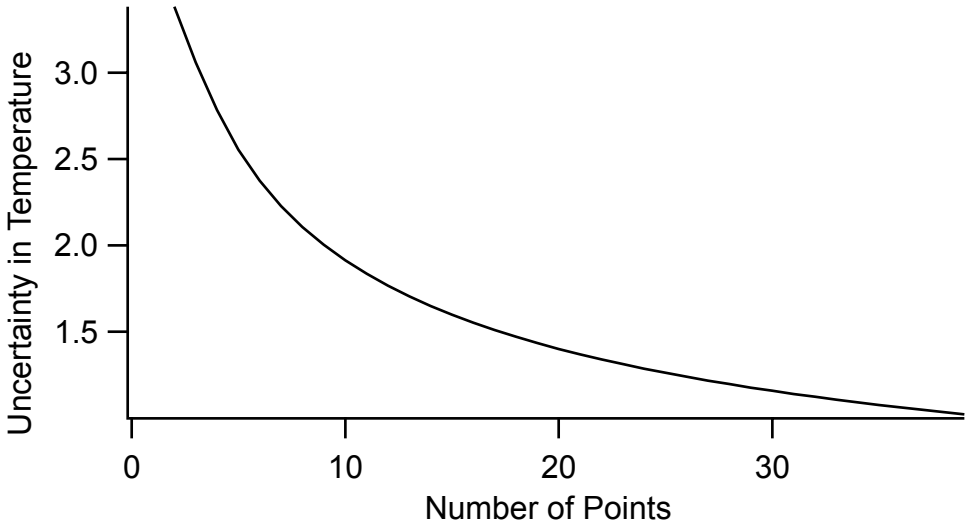

Figure 5.3: Theoretical plot of uncertainty in the temperature measurement as a function of number of points, assuming that the time spent integrating on each point is proportional to the reciprocal of the number of points, and thus that the statistical uncertainty of each point is proportional to the square root of the number of points. Since this is a theoretical plot, the absolute value of the uncertainty is not important. The important information of this plot is carried in the relative change in uncertainty.

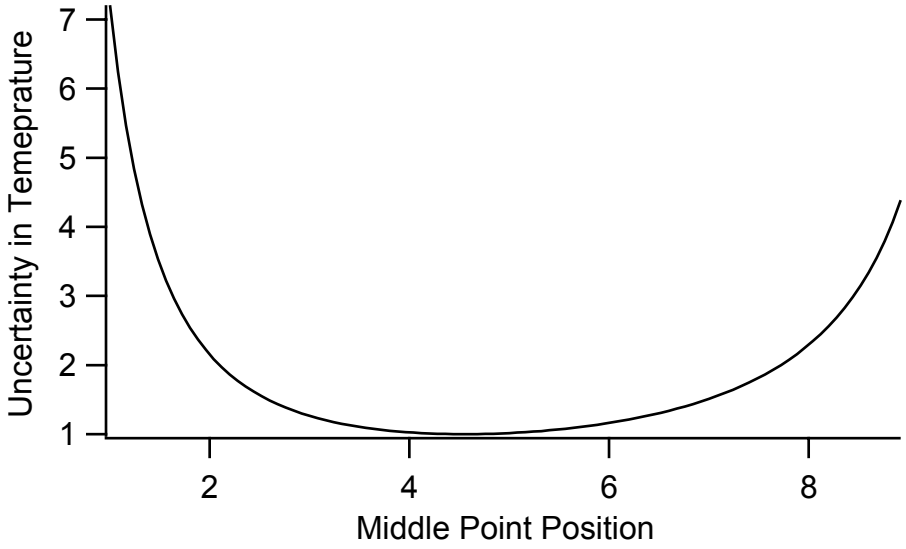

Figure 5.4: Theoretical plot of uncertainty in the temperature as a function of position of smaller bias point, assuming that two bias points are used, and that the larger of those is at normalized voltage x=10. The optimum choice is very close to 5, and repeating this calculation for different choices of the larger voltage also show that having the second point in the middle is very close to optimal. The uncertainty approaches infinity as the second point approaches either zero or the same bias as the larger point.

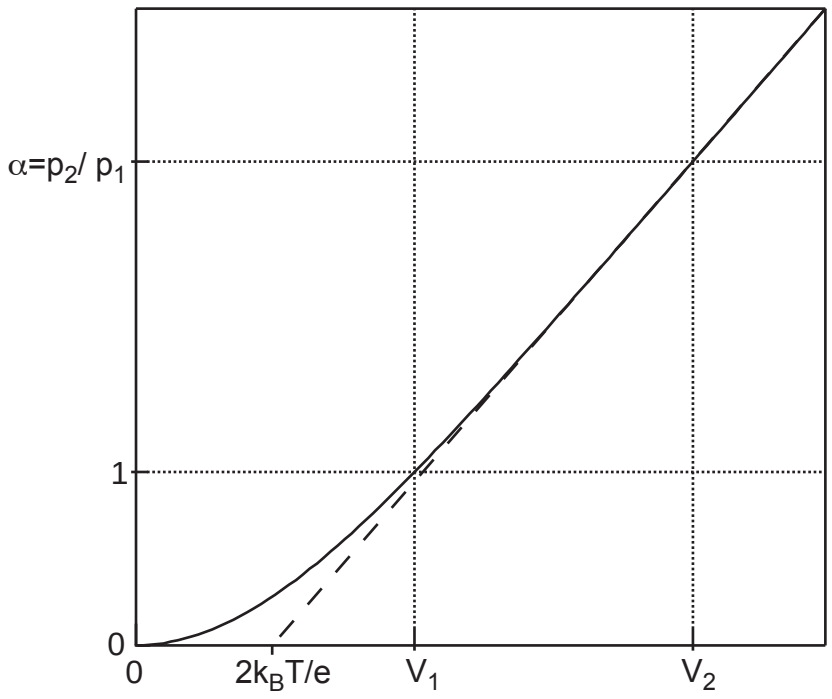

Figure 5.5: Illustration of definitions of variables. Note that P_1 and P_2 both have already had zero voltage noise subtracted.

$\{P_0^1, P_1^1, P_0^1, P_2^1, P_0^2, P_1^2, P_0^2, P_2^2, ...P_0^N, P_1^N, P_0^N, P_2^N\}$, where each point corresponds to an integration time τ. All the noise measurements are combined in two average noise power differences denoted by the lower case letters

$$p_{1,2} = \frac{\sum_{i=1}^{N}(P_{1,2}^i - P_0^i)}{N}. \tag{5.17}$$

The statistical uncertainty in a given noise measurement P for integration time τ is $P/\sqrt{B\tau}$, where B is the bandwidth of the measurement. The value of the noise measurements of the shot noise thermometer is

$$P = G(\frac{eV}{2k_B}\coth(\frac{eV}{2k_BT}) + T_N), \tag{5.18}$$

where T_N is the system noise temperature and G is the total system gain. For the finite bias values the noise is assumed to take the linear shot noise value of $GeV/2k_B$. The uncertainties of any given set of noise measurements add in quadrature to give a total uncertainty for each set of differential noise measurements p_1 and p_2 of

$$\sigma_{p_1,p_2} = \frac{G}{\sqrt{NB\tau}}\sqrt{(T_N+T)^2 + \left(T_N + \frac{eV_{1,2}}{2k_B}\right)^2}. \tag{5.19}$$

To determine the temperature, I first normalize the noise powers by calculating the ratio of the differential noise powers

$$\alpha \equiv \frac{p_2}{p_1} \approx \frac{\frac{eV_2}{2k_B} - T}{\frac{eV_1}{2k_B} - T}, \tag{5.20}$$

from which temperature may be computed as follows:

$$T = \frac{e(\alpha V_1 - V_2)}{2k_B(\alpha - 1)}. \tag{5.21}$$

From this, the uncertainty in the temperature is found to be

$$\sigma_T = \sigma_\alpha \frac{\partial T}{\partial \alpha}, \tag{5.22}$$

where

$$\frac{\partial T}{\partial \alpha} = \frac{e(V_2 - V_1)}{2k_B(\alpha-1)^2}. \tag{5.23}$$

The uncertainty in α is

$$\sigma_\alpha = \sqrt{\left(\frac{\partial \alpha}{\partial p_1}\sigma_{p_1}\right)^2 + \left(\frac{\partial \alpha}{\partial p_2}\sigma_{p_2}\right)^2} = \sqrt{\left(\frac{p_2}{p_1^2}\right)^2\sigma_{p_1}^2 + \left(\frac{1}{p_1}\right)^2\sigma_{p_2}^2} \tag{5.24}$$

$$= \frac{G}{\sqrt{B\tau N}p_1}\sqrt{\alpha\left[(T_N+T)^2+\left(T_N+\frac{eV_1}{2k_BT}\right)^2\right]+\left[(T_N+T)^2+\left(T_N+\frac{eV_2}{2k_BT}\right)^2\right]}. \quad (5.25)$$

So, finally, the uncertainty in the temperature measurement is

$$\sigma_T = \frac{Ge(V_2-V_1)}{2k_B(\alpha-1)^2p_1\sqrt{B\tau N}}\sqrt{\alpha\left[(T_N+T)^2+\left(T_N+\frac{eV_1}{2k_BT}\right)^2\right]+\left[(T_N+T)^2+\left(T_N+\frac{eV_2}{2k_BT}\right)^2\right]}. \quad (5.26)$$

To get the experimentally relevant uncertainty as a function of wall clock time t required to take a given set of data I define the duty cycle D of the experiment by the equation

$$\tau N = \frac{tD}{4}. \quad (5.27)$$

Re-expressing the temperature uncertainty in terms of wall-clock time, and substituting the value for p_1, the temperature uncertainty may be re-written as

$$\sigma_T = \frac{\frac{eV_2}{k_BT}-\frac{eV_1}{k_BT}}{(\alpha-1)^2\left(\frac{eV_1}{2k_BT}-1\right)\sqrt{BtD}}\sqrt{\alpha\left[(T_N+T)^2+\left(T_N+\frac{eV_1}{2k_BT}\right)^2\right]+\left[(T_N+T)^2+\left(T_N+\frac{eV_2}{2k_BT}\right)^2\right]}. \quad (5.28)$$

This is the most general form of the uncertainty given the above data taking method. One important limit worth discussing is that for which $T_N >> T$, which is generally true in dilution refrigerator measurements using semiconductor-based amplifiers. In this limit, I neglect all terms in the square root in the above equation except the noise temperature terms. I also assume that in a typical measurement $\frac{eV_1}{k_BT} = 5$ and $\frac{eV_2}{k_BT} = 10$. With these approximations,

$$\sigma_T = \frac{\sqrt{\alpha+1}\left(\frac{eV_2}{k_BT}-\frac{eV_1}{k_BT}\right)\sqrt{2}T_N}{(\alpha-1)^2\left(\frac{eV_1}{2k_BT}-1\right)\sqrt{BtD}} = \frac{3.25T_N}{\sqrt{BtD}}. \quad (5.29)$$

For a typical measurement in the dilution refrigerator the system noise temperature is about 10 K and the bandwidth is about 100 MHz. In these experiments a 50% duty cycle is typical, so the temperature resolution in a measurement under these circumstances should be about 5 mK/$\sqrt{\text{Hz}}$.

5.4 Effect of an Arbitrary Nonlinearity

I will treat the effect of an arbitrary nonlinearity in a similar way as the analysis of statistical noise effects above. First, I define the linear power P_0 as

$$P_0 = G\left[T_N + \frac{eV}{2k_B}\coth\left(\frac{eV}{2k_BT}\right)\right]. \tag{5.30}$$

I now introduce a general nonlinear noise power as follows:

$$P = P_0 + \beta P_0^2. \tag{5.31}$$

As in the analysis of statistical effects on the fit, I subtract the zero bias noise, using lower case letters to denote such differential noise powers.

$$p(V) = GT\left[\frac{eV}{2k_BT}\coth\left(\frac{eV}{2k_BT}\right) - 1\right]\left[1 + \beta GT_N\left(2 + \frac{T}{T_N} + \frac{T}{T_N}\frac{eV}{2k_BT}\coth\left(\frac{eV}{2k_BT}\right)\right)\right]. \tag{5.32}$$

Note that in the nonlinear case the noise with zero bias noise subtracted still contains information about the noise temperature, unlike in the linear case. I now set the gain and temperature to one and substitute in $x = eV/k_BT$, $r = T/T_N$ and $L = \beta GT_N$ to get the function

$$p(x) = \left[\frac{x}{2}\coth\left(\frac{x}{2}\right) - 1\right]\left[1 + L\left(2 + r + r\frac{x}{2}\coth\left(\frac{x}{2}\right)\right)\right], \tag{5.33}$$

which can then be fit to the function

$$f(x, G, t) = Gt\left[\frac{x}{2t}\coth\frac{x}{2t} - 1\right]. \tag{5.34}$$

The normalized temperature extracted from that fit as a function of the nonlinearity parameter L is plotted in Figure 5.6. Thus the relationship between a parabolic nonlinearity and fit temperature is simply linear for fixed temperature and noise temperature, with the sign of the error depending on the sign of the nonlinearity. More quantitatively, the fractional temperature deviation is 7.4 times the dimensionless parabolic nonlinearity constant L if r is fixed, and is equal to one. In a typical SNT measurement at around 10 K, noise temperature is T_N=10 K, gain is G = 2 μV/K, and the nonlinearity of the diode is β = -3.4 V^{-1}, which gives a L value of -6.8 $\times$ 10^{-5}, leading to a fractional temperature deviation of -5$\times 10^{-4}$. Figure 5.6 also shows the temperature error as a function of the dimensionless noise temperature parameter r for the above L value. This plot is particularly useful, since it shows both how the effect of nonlinearity gets smaller with temperature

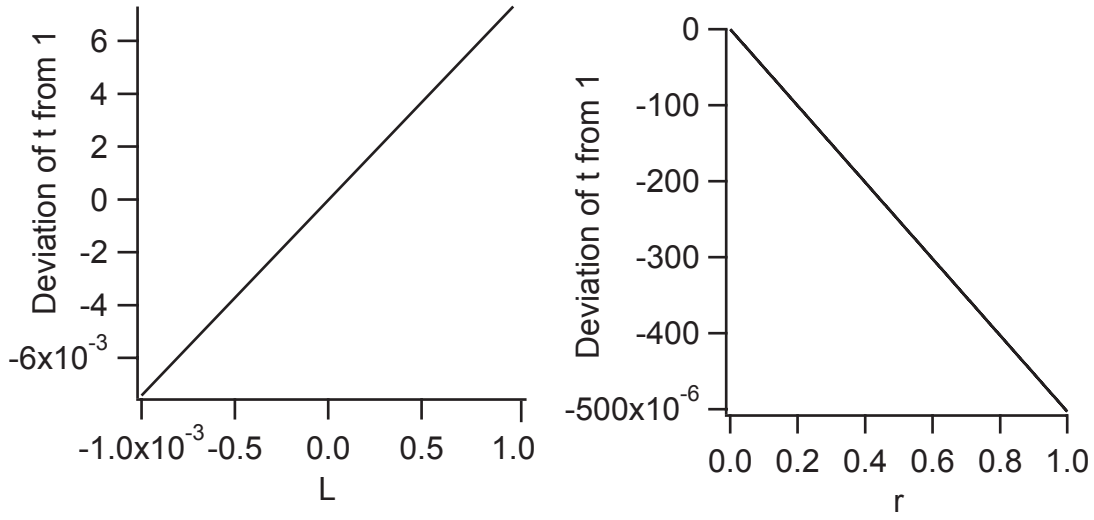

Figure 5.6: The left inset shows the deviation of normalized temperature fit from one as a function of dimensionless nonlinearity parameter L, assuming that the dimensionless parameter r is fixed at one. The right inset shows the deviation of the normalized temperature fit from one as a function of the dimensionless noise temperature parameter r, assuming that L is fixed, and is equal to -6.8×10^{-5}.

and how it can be forced to be smaller by adding attenuation in the RF chain, since that increases the noise temperature and hence decreases r. This is also a linear relationship, with a proportionality constant of -5×10^{-4}.

5.5 Conclusion

To summarize, in this chapter I have found the optimal choice of bias points for an SNT measurement, computed the statistical uncertainty of the SNT temperature measurement for a given amount of wall clock time, and found an algorithm for calculating the effect of an arbitrary nonlinearity in the RF measurement on the temperature determined by the SNT. A good choice of points is to have two points at as high a bias as can be tolerated, with the smaller voltage value of the two points roughly half way between the larger voltage value and zero. In practice, it can be useful to have more points for the purpose of understanding the physics of the tunnel junction, and increasing number of points also slightly increases the precision of the measurement in a given time.

Chapter 6

Fabrication

6.1 Introduction

The ideal device for a shot noise thermometer would be a tunnel junction which has very low lead resistance, a very linear I-V curve, voltage leads very close to the junction, a 50 Ohm impedance, and no superconductivity. The actual technology I used for this thesis evolved from a combination of these needs and what was available.

6.2 Device Design

I designed the devices to allow electrons to diffuse into the current leads as fast as possible while making as close contact to the junction as possible with the voltage leads. While some of the devices were fabricated by electron beam lithography and some were made by optical lithography, they all used the Dolan Bridge double angle evaporation technique, and were designed accordingly. In the Dolan Bridge technique a bridge of resist is suspended above the substrate, and a junction is formed by tilting the substrate two different directions and evaporating metal twice to create overlapping films, which are separated by an oxide which is grown between the evaporations. Figure 6.1 shows how this method works. Figure 6.2 shows a scanning electron micrograph of a Dolan Bridge. This junction fabrication technique is also very widely used for making superconducting tunnel junctions and single electron transistors.

All the devices made for this work were Aluminum-Aluminum Oxide-Aluminum, with roughly the same oxide parameters as are used in typical single electron transistor junctions. In the optically fabricated junctions, a layer of copper was deposited on top of the aluminum double layer to improve both electrical and thermal conductance from the junction to the leads.

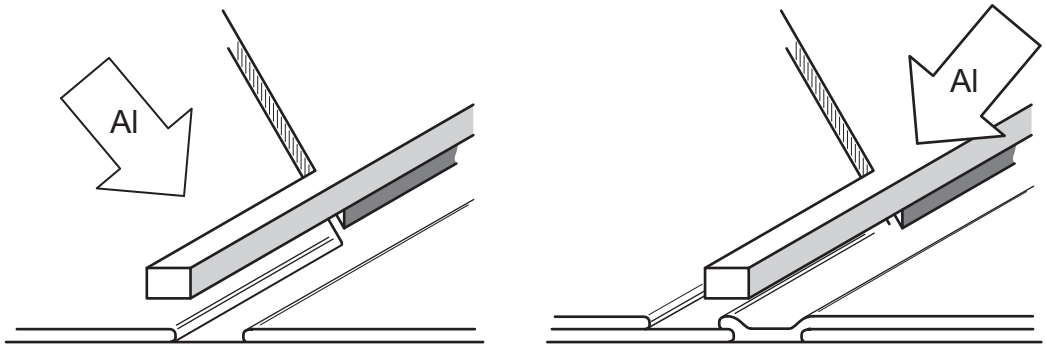

Figure 6.1: Cartoon showing the idea of the Dolan bridge junction fabrication technique. Metal is evaporated from different angles, and the suspended photoresist bridge casts a shadow, causing the films to overlap and form a junction.

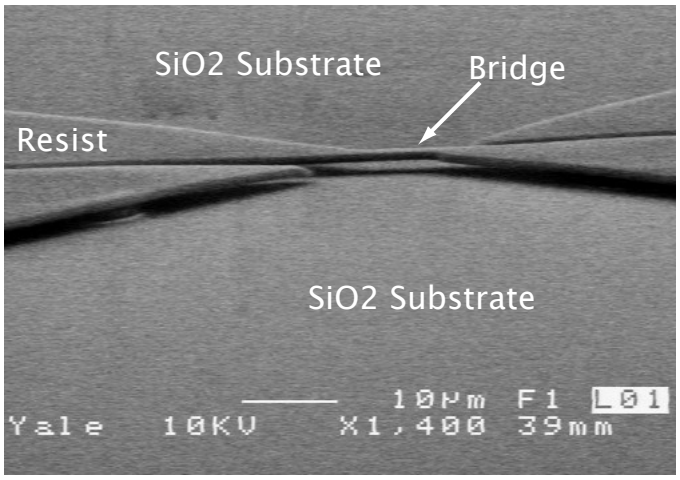

Figure 6.2: Scanning electron microscope image of a Dolan bridge.

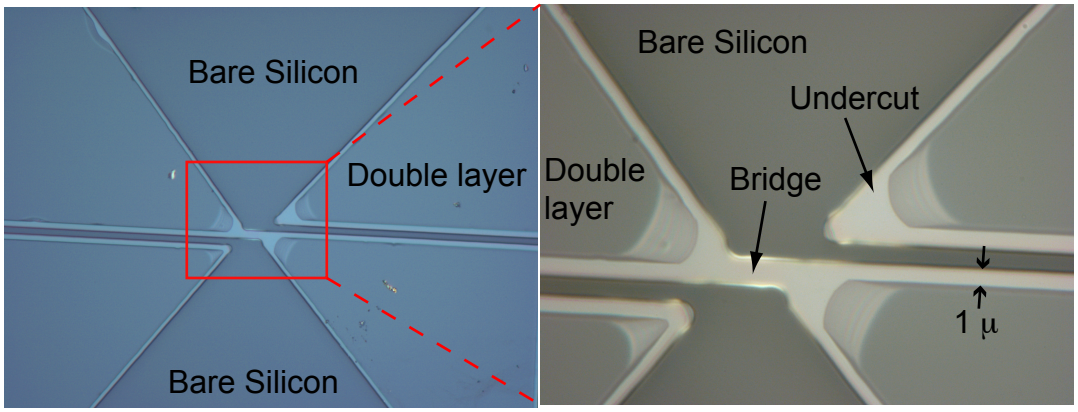

Figure 6.3: Optical image of resist bilayer showing undercut and suspended bridge.

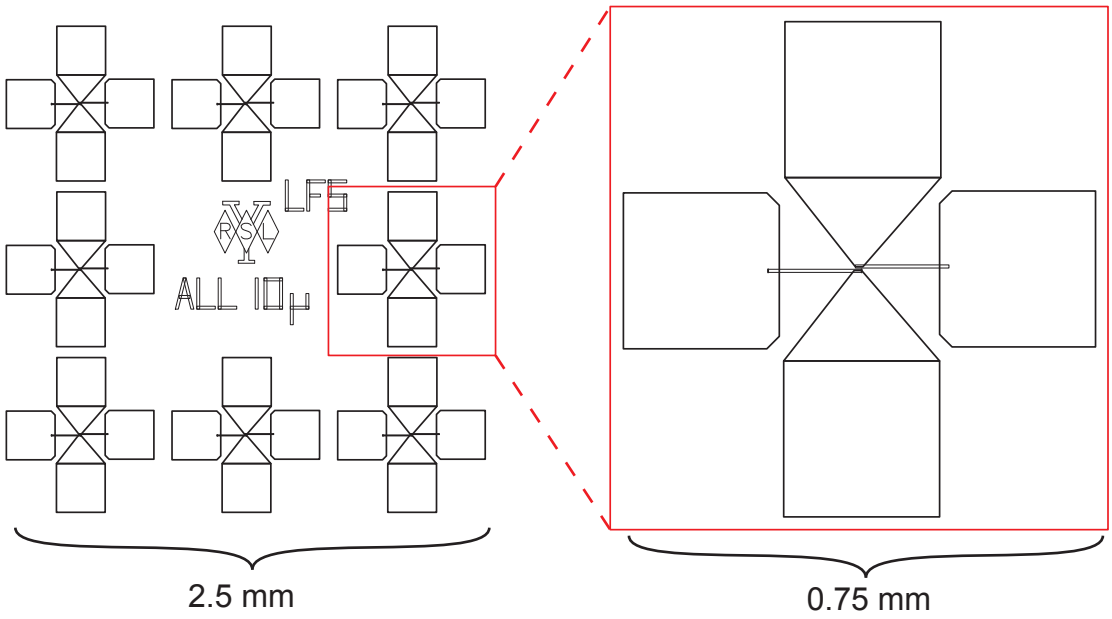

Figure 6.4: Optical die layout. Right inset shows blowup of a single device. The graphics in the center of the die indicate that the Dolan bridge in these devices is designed to be 10 μm long, along with the Schoelkopf lab logo and the author's initials.

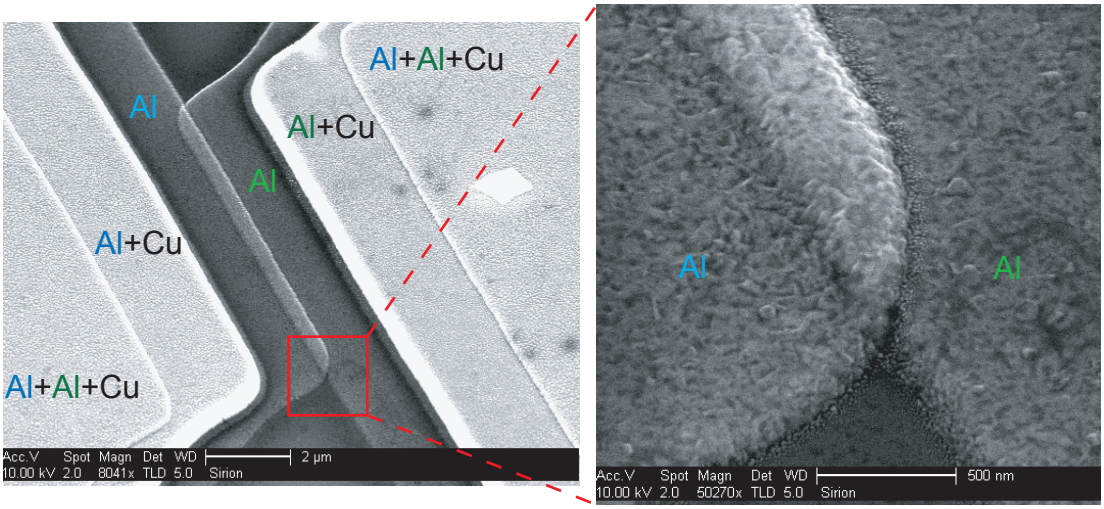

Figure 6.5: Scanning electron microscope image of junction. Right inset shows a zoomed in view of the end of the junction. Note the roughness of the film.

The layout was designed for a four wire measurement, with the voltage leads as close as possible to the junction and the current leads as rapidly expanding in size as possible to maximize diffusion into the leads. Figure 6.4 shows the layout of a typical die from an optical mask used to make SNT junctions. This is roughly identical to the layout used in the electron beam fabricated samples. Figure 6.5 shows a scanning electron micrograph of a typical junction.

6.3 Electron Beam Lithography

The main reason I used electron beam lithography to fabricate junctions is that that was what was available at the time. These devices were all made using the JEOL 6400 SEM converted for electron beam lithography with the Nanometer Pattern Generator System from JC Nabity Lithography Systems, inc. (http://www.jcnabity.com/). With this system it is possible to achieve resolution of better than 100 nm, which is an order of magnitude better than I needed for the devices fabricated for this project. The process I used had a layer of PMMA approximately 0.7 microns thick on top of a one micron thick layer of LOR 5A liftoff resist from Microchem. PMMA, or polymethyl methacrylate, is a very strong polymer also sold under the trade names Plexiglas, Perspex, Acrylite, Acrylplast, and Lucite, and is by far the most common top layer resist for electron beam lithography processes. The bottom layer resist is unaffected by both the electron beam and by the organic developer used for PMMA, and the PMMA is unaffected by the alkali developer which dissolves the bottom layer, so

the undercut is determined only by the development time in the alkali developer. This separation of the top and bottom layer resist chemistries is very powerful, as it removes the difficulties associated with the proximity effect, and makes for a very robust process.

All the electron beam fabricated devices were made by depositing aluminum from a tungsten boat in a Varian bell jar thermal evaporator. The details of this process are described in the Appendix. This generation of devices did not have the copper third layer.

6.4 Optical Lithography

Roughly half of the data taken in this work were on junctions fabricated optically. This is a far superior method of making devices than electron beam lithography, since hundreds can be made at a time with potentially high uniformity. The process used here consisted of an approximately 1 micron thick layer of S1813 photoresist from Shipley on top of about a 1 micron layer of LOR 20B liftoff resist, from Microchem. Unlike the electron beam process above, the resist chemistries of the top and bottom layer are not independent in this process, and a single developer is used to both remove the exposed sections of the top layer and to etch away the bottom layer and create the undercut.

The optical lithography was all done with an HTG mask aligner on 2 inch wafers in Yale's cleanroom. The illumination of the wafer by the mask aligner is nonuniform by as much as 10 %, and this leads to significant deviations in the width of the resist bridges across the wafer, which in turn lead to very poor uniformity of junction parameters. Figure 6.6 shows the distribution of junction resistances that results from this non-uniformity.

6.5 Substrate Issues

As with most tunnel junction devices, the substrate is not critical for shot noise thermometer junctions, but poor choice can be disastrous. The substrate must be totally insulating at DC over the whole relevant temperature range. This rules out using any plain semiconducting wafer without an oxide coating. Furthermore, using a wafer with even a moderate resistivity is unacceptable even with an oxide coating because of voltage depended microwave leakage. In this situation, the leads of the tunnel junction, the silicon dioxide layer and the underlying silicon form an MOS capacitor. This leads to a voltage dependent RF current path around the junction, which causes serious errors

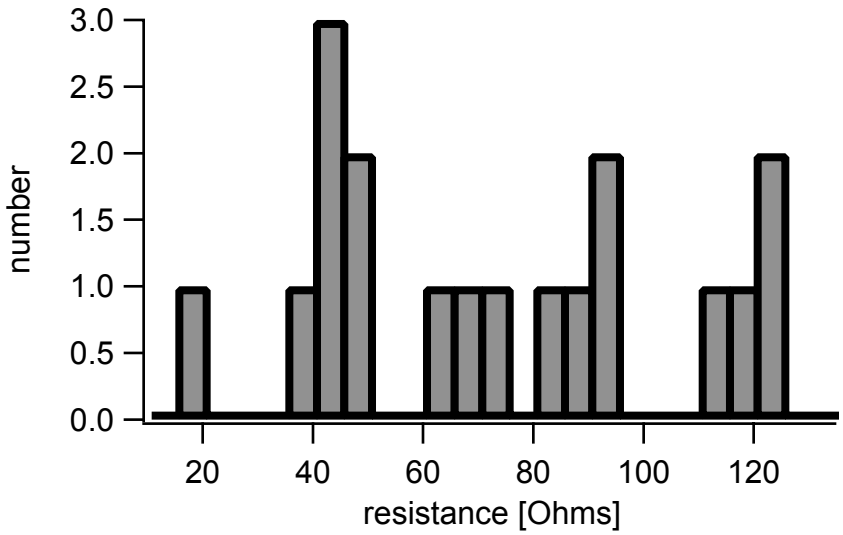

Figure 6.6: Histogram of optical junction parameters. The average is 77 Ω, with a 39 Ω standard deviation.

in the operation of the shot noise thermometer. If silicon wafers are used they should have as high a resistivity as possible. The wafers I used to fabricate my best junctions were "ultra high resistivity" 2 inch wafers from Virginia Semiconductor, which had a >20 kΩ-cm resistivity and a 470 nm steam grown oxide.

Another concern is that the substrate must allow for the formation of high enough quality metal films to grow good tunnel barrier oxides. I made a series of junctions on soda glass cover slips which were all severely pathological. Junctions made on glass exhibited random drift in resistance by as much as an order of magnitude in a few minutes with abrupt switching between resistance states (see Figure 6.7). Clearly, this behavior is totally unacceptable for a practical device, and must be avoided at all costs. This behavior never appeared in junctions fabricated on silicon wafers, except for irreversible transitions to a high resistance state.

One final design issue is thermal conductivity. This is more relevant at higher temperatures because diffusion cooling through the leads dominates at the sub-kelvin temperatures. In future generations of devices, switching to sapphire would probably be useful, however. Sapphire might also produce higher quality aluminum films.

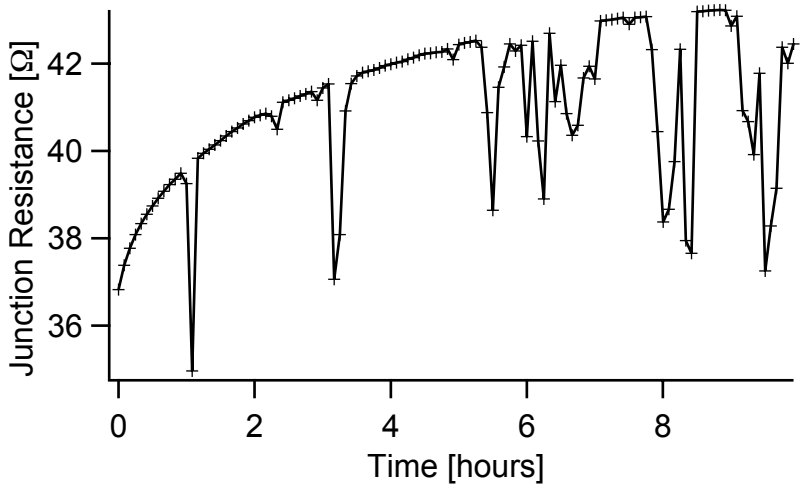

Figure 6.7: Drift of resistance of tunnel junction fabricated on a glass slide. This pathological behavior shows the danger of using the wrong substrate material for junction fabrication.

6.6 Blind Alleys and Problems

Destruction of junctions appears to be an inevitable side effect of working with tunnel junctions. Anecdotal evidence indicates that large junctions such as those used in this work are much less likely to get spontaneously destroyed than small junctions, but destruction does occasionally happen. The junctions that I measured which were destroyed all went to around a 1-3 Ohm short. Figure 6.8 shows an AFM image of a destroyed junction. The exact mechanism of junction destruction is not well understood. Static discharge of various kinds can destroy junctions, and exposure to multimeters, proximity to turbopumps, and direct exposure to cryogenic liquids are also known to destroy junctions sometimes. In practice, the best one can do to preserve junctions is to attempt to minimize exposure to these types of stresses, although junctions will occasionally die no matter what.

The most frustrating aspects of fabrication were in trying to get the undercut sufficient in the resist bilayer to create a totally suspended bridge that could be used for the double angle evaporation process. This proved to be particularly difficult in the optical process, since the top and bottom layer both use the same developer. The two most common failure modes were that the developer would be too aggressive on the top layer and the bridge would be destroyed or that it would not be aggressive enough on the bottom layer and it was impossible to get the needed undercut to suspend the bridge or in some cases even to etch down to the substrate. The effect of the developer on the

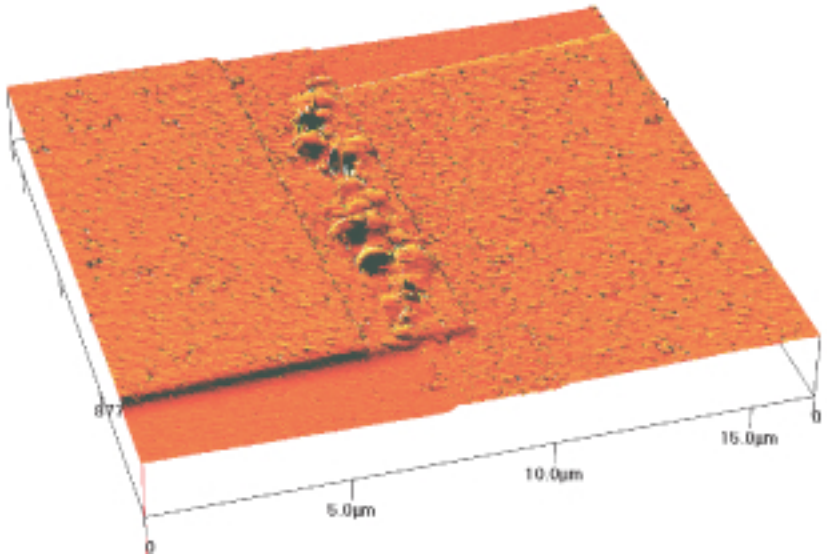

Figure 6.8: Destruction! Atomic force microscope image of tunnel junction that died to short. Destruction to short was by far the most common failure mode of these junctions.

top and the bottom layer work against each other: the more aggressive the developer, the more likely it is to destroy the bridges, but the less aggressive it is, the less likely it is to provide the needed effect on the bottom layer. The most important parameter to vary in finding the correct parameters turned out to be the concentration of the developer. Once I realized that this was the key variable, it was relatively easy to find a working process, and that process turned out to be very robust once it was working.

Chapter 7

Apparatus

7.1 Overview

In this section I will summarize the components that are needed to make the SNT work. First of all, the junction must be in an enclosure that protects it from radio noise of all kinds. This means that it must be in a conducting box that is sealed in a light-tight manner and has light-tight connections to both the RF line and the DC lines. I solved this problem by using two types of sample holder. First, and most frequently, I used the "jellyhog" sample holder that is in standard use in the Schoelkopf lab for all of our cryogenic experiments. This sample holder is a copper box about the size and shape of a hockey puck that gets its name from its similarity to a jellyfish and also to a hedgehog, due to the tentacle-like semi-rigid coax lines that protrude from its top. The other type of sample holder I used is a capsule made from copper plumbing fittings that is designed specifically for the SNT, and is intended to be as compact as possible. Inside both sample holders there must be some kind of circuit board which holds the chip with the tunnel junction on it and has wire bonds to which the chip is connected. These boards have a set of surface mount inductors and capacitors that separate the RF and DC signals from each other.

The next section that must be described in detail is the RF chain for measuring the noise power. There are some details to this that are essential if it is to work at the lowest temperatures. Next, the setup of the DC lines will be explained in detail. An essential component of the DC lines is the filtering, which must eliminate thermal noise from higher temperature parts of the cryostat while maintaining true twisted pair geometry to minimize low frequency pickup. We have devised a new form of filter for this application, which I will explain in detail in its own section.

The measurements described here below 250 mK were done in two dilution refrigerators, a Kelvi-

nox 400 from Oxford Instruments, and a dilution fridge from Cryoconcepts. The measurements between 250 mK and 4 K were done in a Heliox pumped helium-3 cryostat also from Oxford Instruments. The details of the commercial cryostats are described elsewhere and will not be described in detail here. The high accuracy temperature measurements above 4 K were done in a cryostat that I built for this purpose, and a section will be devoted to the design of that apparatus. Finally, the secondary thermometry used for comparisons will be discussed in detail, as well as how those measurements were carried out.

7.2 Sample Holder Design

I will first discuss the jellyhog style sample holder. The jellyhog is a standardized set of sample holders in use in the Schoelkopf lab which act as interchangeable parts. The system involves a set of interchangeable circuit boards with 20 DC wires and five microstrip lines for RF signals (see Figure 7.1). Each RF line is connected to a standard 50 mil pin that plugs into an SMA connector which is attached to the base of the jellyhog by 2-56 screws. One of the RF lines is wider than a standard mictrostrip, and is connected to the jellyhog by a screw as well as by one of the pins, in order to act as an RF ground. In the SNT experiment, the ground microstrip and one other microstrip are severed with a razor blade and a surface mount capacitor, generally 100 pF, is soldered across the break with solder paste, melted with a heat gun.

The DC lines connect to an AMP MODU type connector, a class of cheap, modular connectors available from Tyco Electronics. The connector solders into the board, just as the RF pins do, and goes through a square hole in the base of the jellyhog. Above this hole is connected a square box we call a "shroud" which contains another AMP MODU connector which in turn connects to a ribbon cable which leads out through the box into a shielded filter cable described below in the filter section (see Figure 7.12). The DC lines also have cuts made in them with razor blades, across which are soldered surface mount inductors, also with solder paste and a heat gun. Wire bonds are made from the four wire bond pads on the chip to the four DC lines with inductors and to the RF signal and ground pads. Once the chip, surface mount components and board are all in place, a copper lid is securely screwed on the jellyhog which makes it light-tight.

The other sample holder I used was more compact, and was specifically designed for the SNT, although unlike the jellyhog, I do not have a whimsical name for it. Figure 7.2 shows a photograph of the SNT capsule style sample holder. The main copper tube is 3/8 of an inch outer diameter

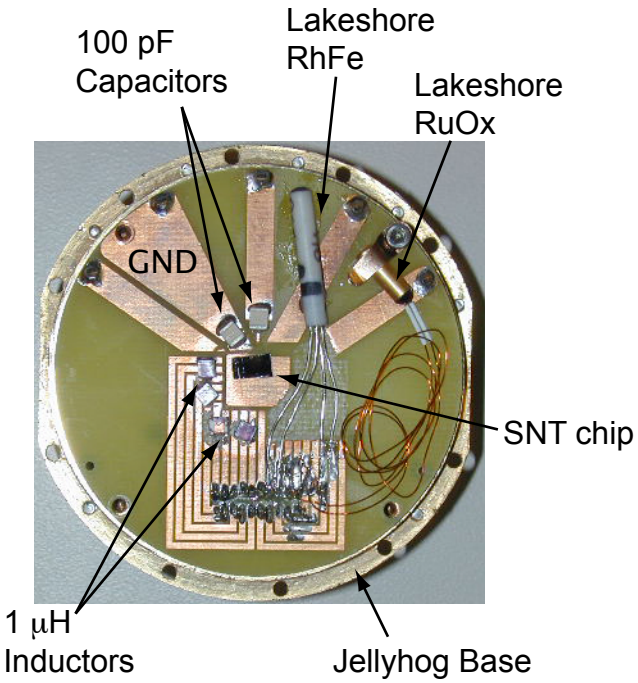

Figure 7.1: Typical Jellyhog board, showing various components used for SNT experiment, including the Lakeshore secondary thermometers used for temperature comparisons.

(9.53 mm) and 0.30 inches inner diameter (7.62 mm), which is the size that the American tubing industry calls "1/4 inch". The cap at the end of the top is a "1/4 inch" sweat fitting, available at any plumbing supply store in the United States. The cap has a hole in it with a thin tube soldered into it which high-pass filters all frequencies of radiation below millimeter wavelength but allows gas to pass out of the capsule when the vacuum can is being pumped out, preventing air from getting trapped. The base of the sample holder consisted of a "1/4 inch" copper sweat coupling with a piece of solid copper rod soldered into one end. The solid copper plug has a pair of holes drilled in it, one the right size for a thin hollow copper tube for the DC wires and the other the right size for a semi rigid copper coax line. Both of these are soft-soldered into their respective holes. A circuit board with appropriate patterning for the surface mount components and bond pads to connect to the junction is attached to the semi-rigid coax by a bead of solder applied with a soldering iron. This bead also forms the ground connection for the RF ground. The inner conductor of the coax is soldered to the circuit board, and twisted pair DC lines which are fed down the thin copper tube are soldered to the copper traces on the board. These thin copper tubes are 1/8 of an inch outer diameter (3.18 mm), and are available from Utrecht art supplies (part number 51084.) Utrecht also sells a slightly larger size tube with an outer diameter of 5/32 of an inch (3.97 mm), into which the smaller size fits snugly. The 5/32 inch tube is part number 51083, and both of these can be purchased on the Utrecht website at http://www.utrecht.com. By alternating between these sizes, it is possible to join successive segments with rosin core solder applied with a soldering iron, making a tubes of arbitrary length down which DC wires may be passed. This is useful in making SNT probes that need to go deep into some small space, such as down the neck of a helium storage dewar.

The selection process for the surface mount components was straightforward. They must be of a type that works at low temperatures, the capacitors much have a low impedance at the frequencies of noise being measured, and the inductors must have a high impedance at those same frequencies. I used 100 pF ceramic surface mount capacitors from American Technical Ceramics (ATC) for all the capacitors in this work. The impedance of a capacitor at frequency f is $Z = 1/i2\pi fC$, which has a magnitude of between 2.5 and 5 Ohms for the frequency range used in these experiments (300-600 MHz). The impedance of an inductor at frequency f is $Z = i2\pi fL$, which has a magnitude between 100 and 250 Ohms for the frequency range used here with 390 nH inductors. The inductors used were all wire wound surface mount inductors from Coilcraft. It is important to select inductors without ferrite cores, since they can be highly temperature dependent.

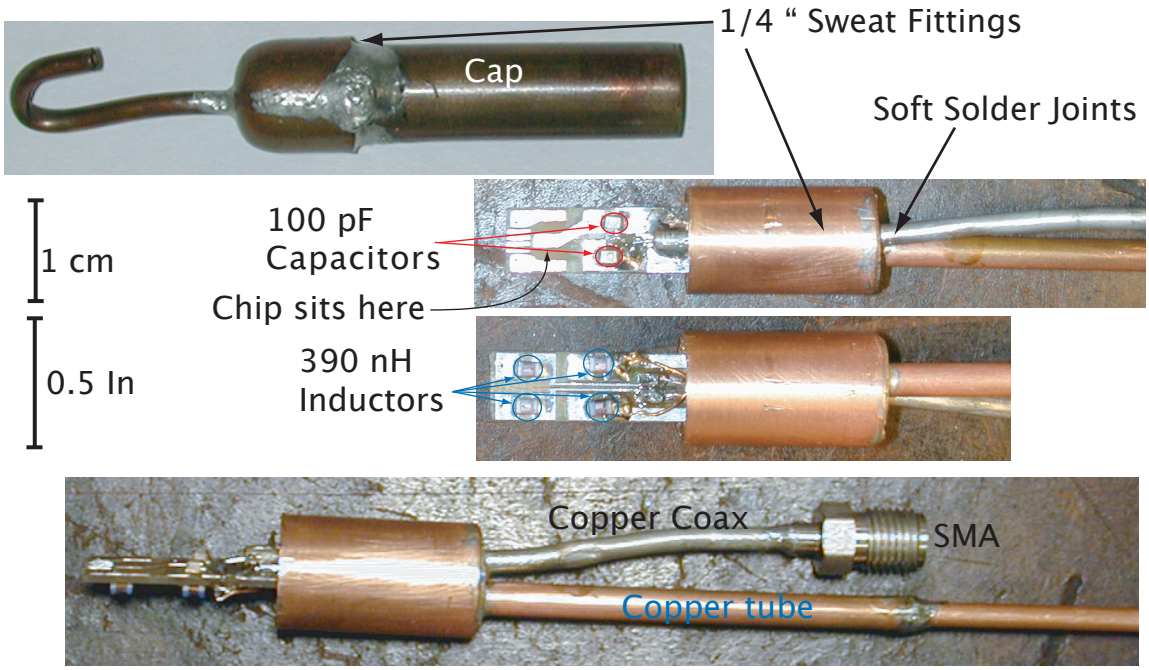

Figure 7.2: SNT capsule. In this form, the SNT has a form factor much closer to what one would normally associate with a thermometer than the jellyhog setup.

By connecting two junctions in series with a capacitor it is possible to construct a “noise bridge”, which could be used to circumvent the nonlinearity problems in the SNT. The schematic of this noise bridge is shown in Figure 7.3. At high frequencies, the junctions are simply in series, and so the measured noise power is proportional to the sum of the noise powers from the two junctions. At DC, the junctions are not connected at all, and are each measured by their own distinct set of four wires, as in the standard SNT circuit. In this apparatus, noise power is measured as a function of the two voltages on the junctions, which can be plotted as a two dimensional surface. This surface has the shape of an inverted square pyramid with rounded corners. At any fixed noise power for a pair of voltages (V_1, V_2) such that $\sqrt{V_1^2 + V_2^2}$ is larger than a few $k_B T/e$, the contour of constant power looks like a square with rounded corners. The exact shape of this square can be very accurately measured, since it depends only on DC voltages which can be accurately measured and the extent to which very small changes in noise power can be detected and removed. At a low enough level of deviation in noise power, any amplifier chain can be made to be arbitrarily linear, so if temperature could be extracted from this data, nonlinearities of the amplifier would be eliminated. I have not pursued this method very far, but I did construct a sample holder that allows for these measurements

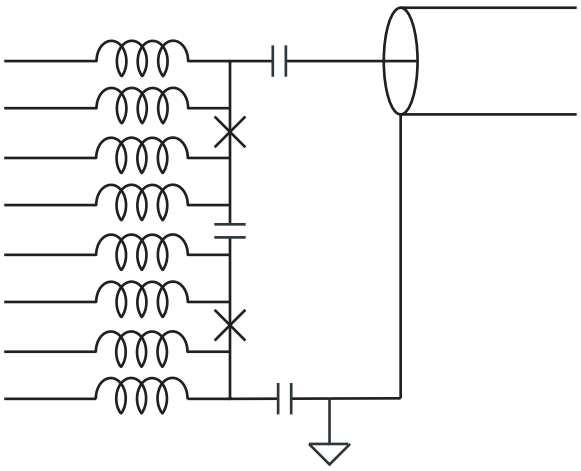

Figure 7.3: Noise bridge schematic. In the RF, the junctions are in series, but as DC circuits they consist of two totally independent four-wire measurements.

to be made, which is shown in Figure 7.4, and have taken enough data at room temperature (shown in the next chapter) to demonstrate the the RF circuit in Figure 7.3 works. This method may be worth pursuing by future researchers, but does not address the nonlinearities of the device noise as a function of voltage which are dominant at this point.

7.3 RF Setup

The RF setup used differed slightly in the various experiments, but the basic layout remained standard, and I will describe that here. Much care must be taken in the layout of the RF circuitry to prevent any form of heating from affecting the junction. The details given here are for the dilution refrigerator measurements in which the thermal demands to keep the sample cold are the most severe. For warmer experiments some components described here can be left out, but the principles remain the same.

One aspect of the process of keeping the device cold is thermal isolation and appropriate heat sinking of the device. This is achieved by use of semi rigid cables made from stainless steel on both the inner and outer conductors. These help isolate the base from the warmer parts of the cryostat, while still passing the RF signals, and are used to bridge the last thermal gradient before the base temperature, which is the most critical thermal gradient. Lines that are only stainless steel on the outer conductor are used to bridge the higher temperature thermal gradients, with copper braids

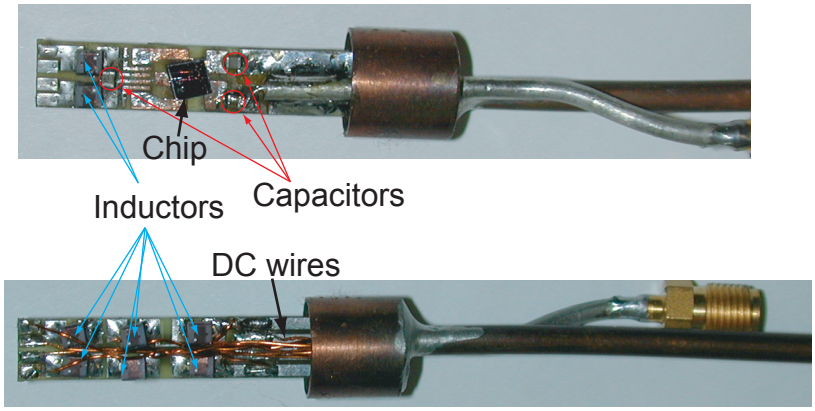

Figure 7.4: Noise bridge capsule. This is the physical implementation of the circuit shown in Figure 7.3

heat sinking their outer conductors to various temperatures as shown in Figure 7.5. The inner conductor of the bottom piece of coaxial cable is heat sunk using an Anritsu bias tee. The RF port of the bias tee is connected to the side facing away from the device, the RF+DC port faces the device, and the DC port is connected via a powder filter to a terminator. The powder filter consists of a wire over a meter long fed through a hole in a copper block filled with metal powder suspended in epoxy, and provides a very effective heat sink.

Also relevant to making the device stay cold is filtering out thermal photons from warmer parts of the experiment. This is accomplished by the use of two low pass filters and a circulator. The low pass filter closest to the device is a short piece of lossy coax with metal powder in it which aggressively filters very high frequencies, although it also adds loss in band. The next stage is a 750 MHz low pass commercial LC filter from Minicircuits (an SLP 750). These filters are both at the base temperature of the dilution refrigerator. The circulator, which sits at the 50-100 mK plate, acts as a one way valve for RF signals, sending warm photons or other noise from the amplifier to a 50 Ω terminator while all the colder parts of the experiment are exposed to is the thermal noise from the cold terminator. Figure 7.6 shows the characteristics of the circulator for passing RF signals in opposite directions. The circulator has a slight, almost constant, attenuation in the forward direction, and a strongly frequency dependent attenuation in the reverse direction that peaks in the band of the amplifiers used in this experiment, which are centered around 450 MHz.

After all the stages of filtering between the device and the 4 kelvin helium bath, the signal goes through a directional coupler which allows signals to be intentionally fed down to the device if

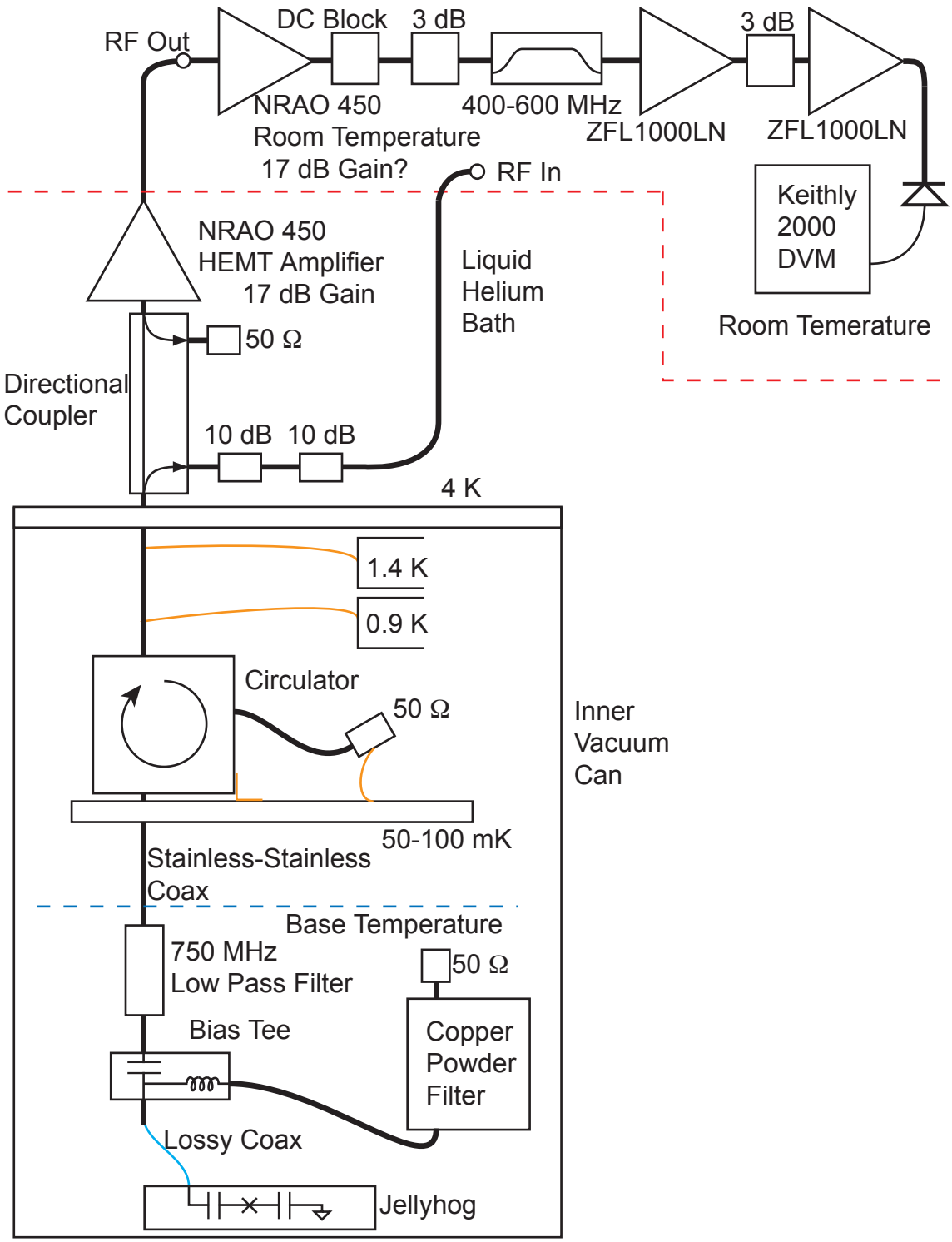

Figure 7.5: Schematic of RF setup used in dilution refrigerator experiments.

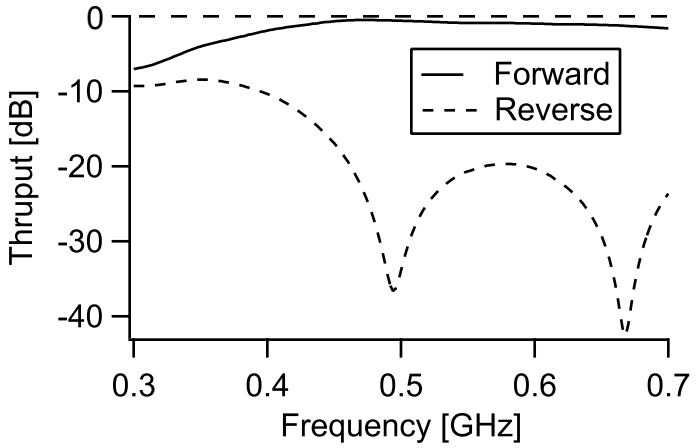

Figure 7.6: Circulator plot. This shows the reverse isolation and throughput of the circulator used in the dilution refrigerator measurements described in the next chapter. Data shown are at room temperature. Slight shifts in frequency take place with cooling.

needed and then to a cryogenic HEMT amplifier. While the circulator and filters cause high attenuation, with the high powers available at room temperature it is still possible to irradiate the device to see frequency dependent effects described in the noise theory chapter and to be demonstrated in the results chapter. The amplifiers I used were all made by Richard Bradley at the National Radio Astronomy Observatory (NRAO), although commercial amplifiers are available with similar characteristics. The noise temperature and gain of a typical NRAO HEMT amplifier is shown in Figure 7.7. Although the noise temperature for this type of amplifier can be as low as 2 kelvin, the measured system noise temperature was typically around 10 K, which is presumably due to the attenuation of the signal between the junction and the amplifier. These amplifiers always sit in the helium bath, and their noise temperature sets the overall noise temperature of the measurement. As was described in the chapter on the least squares fit, at the lowest temperatures this noise temperature totally dominates the signal to noise ratio of the experiment, since it is much larger than the physical noise temperature. Ideally, these amplifiers would be replaced by or augmented by a first gain stage using SQUID amplifiers, which could have as much as two orders of magnitude lower noise temperature. The output of the cryogenic amplifier is connected via a stainless steel coaxial cable to a room temperature feedthrough, to which the room temperature RF chain is connected. This RF chain consists of a series of amplifiers separated by attenuators to prevent excessive reflections which can lead to oscillations and a bandpass filter made from commercial LC filters from Minicircuits. The first stage of the RF chain was generally an amplifier with about a 30 kelvin noise temperature,

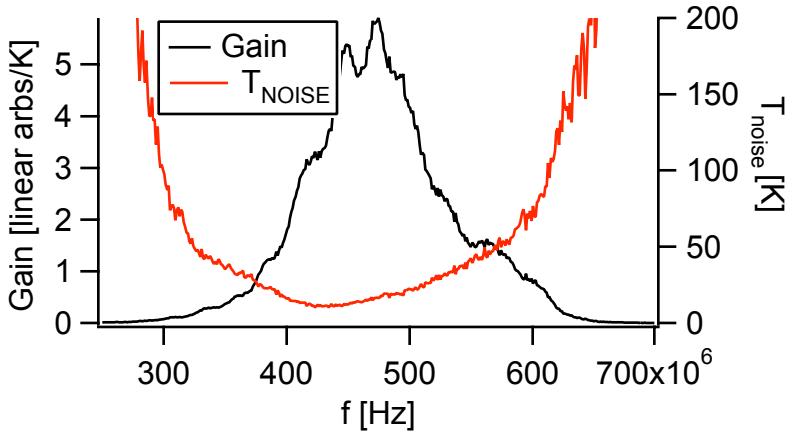

Figure 7.7: NRAO 450 gain and noise temperature. These data were taken by comparing noise spectra of the SNT at different bias points. In addition to showing the properties of the amplifier used in this work, this plot shows the utility of the SNT for amplifier characterization.

also made at NRAO, which is designed to match the frequency band of the cryogenic amplifier. The other gain stages were Minicircuits amplifiers with several hundred kelvin noise temperature. Finally, this signal was connected to a Herotek DZM020BBP zero bias Schottky diode, which produces a DC voltage proportional to the incident RF power. This voltage is read out by a Keithley 2000 digital voltmeter over the GPIB to a personal computer.

An alternate RF setup that was used to determine the how the measurement might depend on frequency involves use of a mixer to select only a narrow bandwidth around a single frequency. Figure 7.8 shows a schematic diagram of how this measurement was performed. Single frequency measurements of this type can also be performed with a spectrum analyzer in zero span mode, however the level of nonlinearity of the spectrum analyzer is both not sufficient and not well specified, and so it is unsatisfactory as a detector for high precision SNT measurements.

7.4 DC Setup

The DC apparatus is also largely designed around the problem of minimizing heating of the device and eliminating incident thermal photons. Figure 7.9 shows the overall layout of the DC measurement. The DC lines are connected via surface mount inductors and an AMP MODU connector both already discussed to the so-called “tapeworm filter”, a filter we invented in our lab for twisted pair measurements. This filter is called a tapeworm because its long, flat geometry resembles roughly the shape of the well-known parasite the tapeworm. The tapeworm filter will be discussed in detail

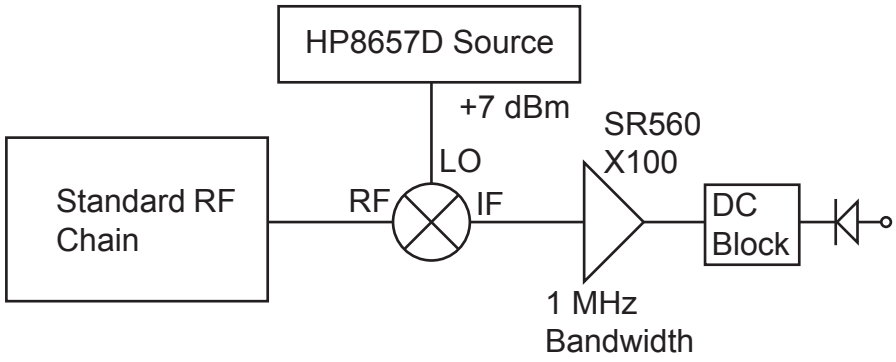

Figure 7.8: Schematic diagram of noise measurement with a mixer. I typically used a Minicircuits ZFM2000 mixer. LO RF and IF stand for local oscillator, radio frequency and intermediate frequency respectively.

below in the filtering section of this chapter. It is always at the base temperature of the cryostat, and in addition to its direct contact the the sample holder, it is generally heat sunk via a copper braid directly to main cooling stage. This acts both as a filter and a heat sink for the DC lines.

The tapeworm filter is connected via a micro-D connector, available from Tyco electronics, to manganin twisted pair lines that exist in both of the dilution refrigerators used in this work. These lines are thermally anchored at the various intermediate temperature stages and connect to yet another set of micro-D connectors on the 4 kelvin plate inside the inner vacuum can of the cryostat. From this connector a ribbon cable connects to a commercially fabricated circuit board, called the "mollusk board" due to the resemblance of its circuit layout to a clamshell (see Figure 7.10). Surface mount resistors are soldered to this board which creates a voltage divider for the all the DC lines to attenuate the thermal noise from warmer parts of the cryostat. Figure 7.9 has a detail of the schematic on the mollusk board. The voltage divider on the current bias lines fixes the ground of the circuit as cold cryostat ground, and makes the actual bias across the device symmetric with respect to that ground. The 100 Ω resistors in series with the device on the current bias act as bias resistors for measuring the current. One of these resistors is selected to have four wires connected from it to room temperature which allows its resistance to be measured accurately and then its voltage to be monitored to measure the current through the SNT junction. The voltage bias lines simply have 10 kΩ resistors in series.

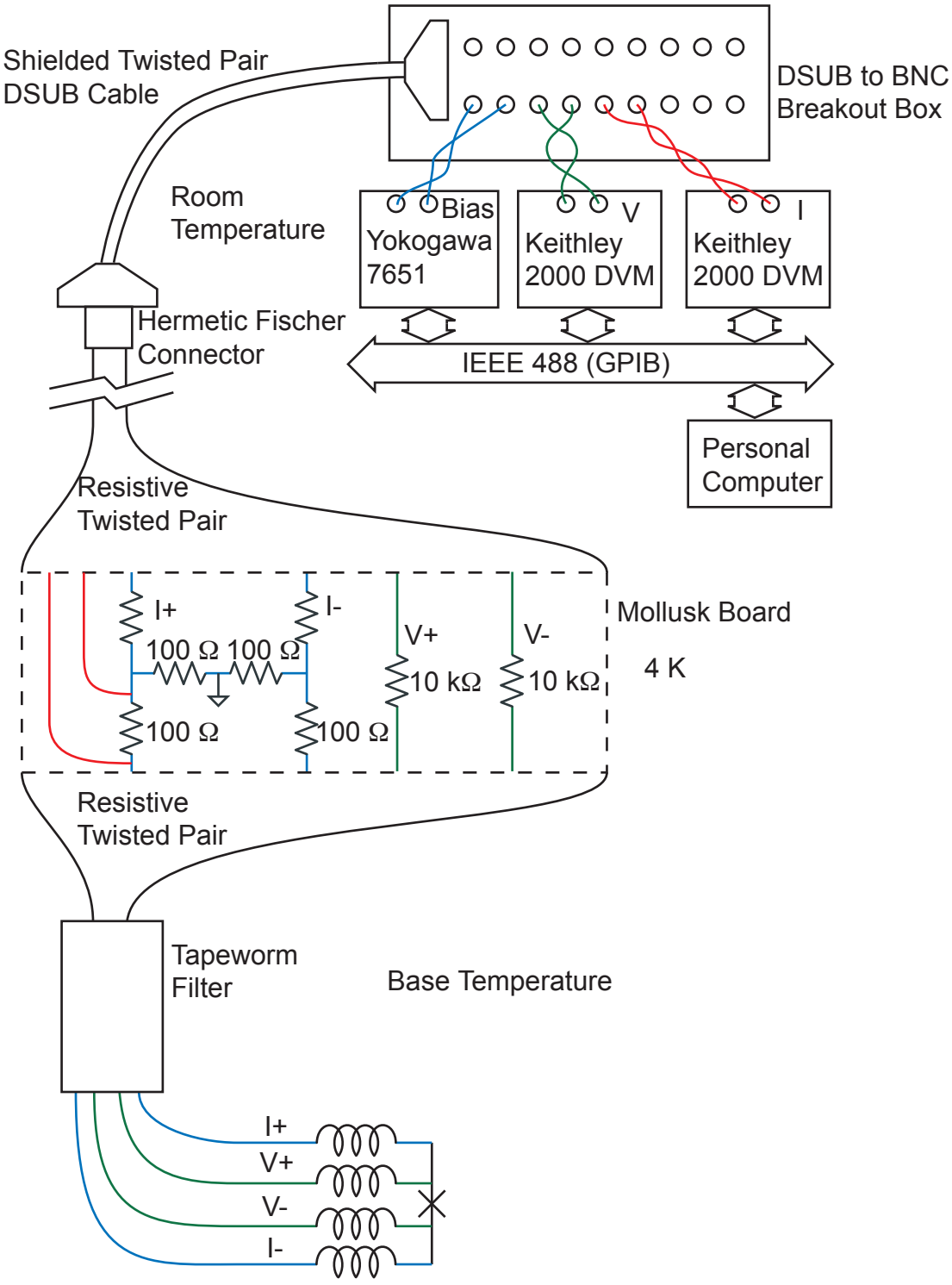

Figure 7.9: Schematic of DC setup used in dilution refrigerator experiments.

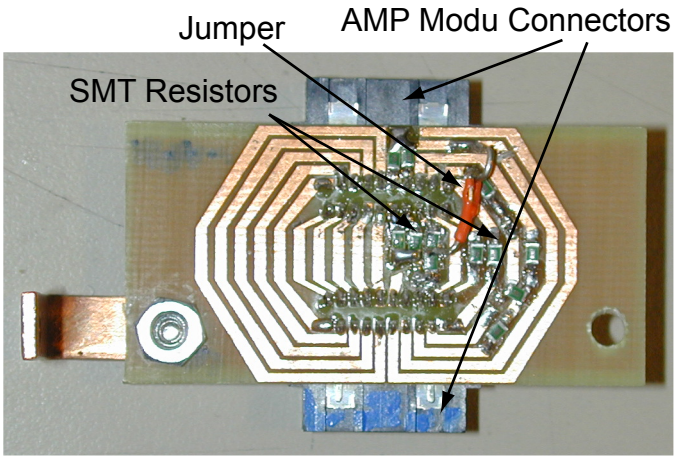

Figure 7.10: Photograph of a mollusk board. The exact layout of the surface mount resistors is shown in Figure 7.9. The copper bracket shown on the left of this image is fastened to the 4 kelvin plate, and large copper traces that cover most of the opposite side of the board are also connected to the plate by a copper braid to provide an added heat sink.

7.5 Filtering

In this section I will describe the construction and testing of the tapeworm filter in detail. All of this work was done in collaboration with John Teufel, a fellow graduate student in Rob Schoelkopf's lab who also needed a twisted pair filter for his superconducting tunnel junction detector.

The tapeworm filter consists of a twisted pair of resistive wires wrapped tightly in copper tape. The copper tape acts both as a shield and as a ground to which the lines are capacitively coupled. The copper tape is pressed around the wires very closely so that the distance between the wires and the shield is that of the insulator thickness on the wires, about 10 micrometers. Thus there is a high capacitance from the wires to ground as well as between the two wires in any given pair. This capacitance to ground combined with the high resistivity of the wires makes the cable a continuous RC line (see Figure 7.13). This system is simple enough that the RF loss of the line as a function of length can be modelled accurately.

The ends of the wires are soldered to a short segment of ribbon cable which allows for easy connectorization and which is more mechanically and thermally robust than the main section of the cable (see Figure 7.11.) The ribbon cable end may then be slotted through a copper shield into the box which contains the experiment, and sealed in with low temperature solder. This creates RF-tight continuous shielding from the noisy end of the filter down into the low noise shielded enclosure

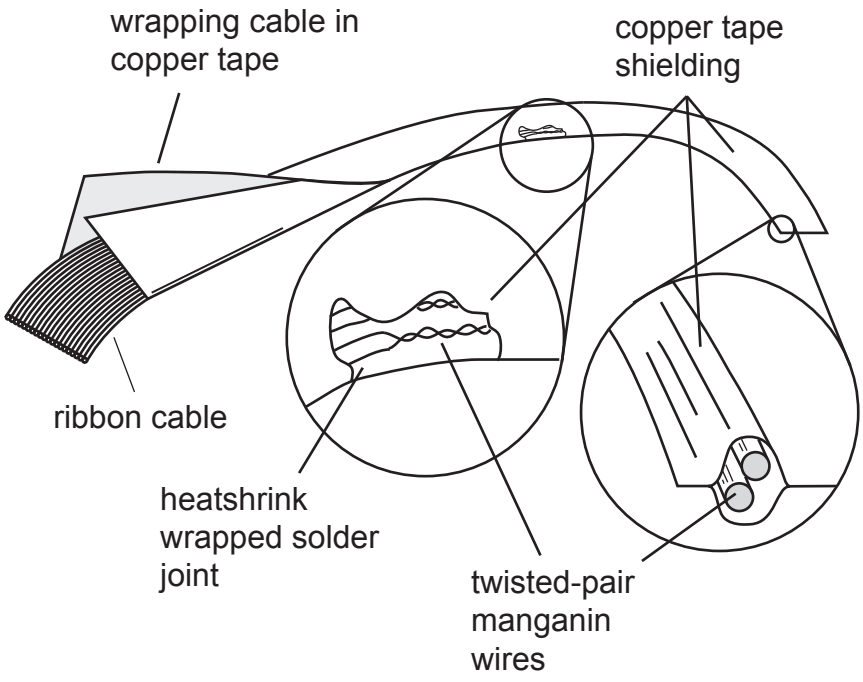

Figure 7.11: Tapeworm assembly diagram. This shows how the copper tape is wrapped around the wires to form a shield. The cutaway diagram shows how the twisted pairs are joined to the ribbon cable inside of the shielding. The cross sectional zoom to the right shows how each twisted pair has its own shield once the copper tape has been properly pressed.

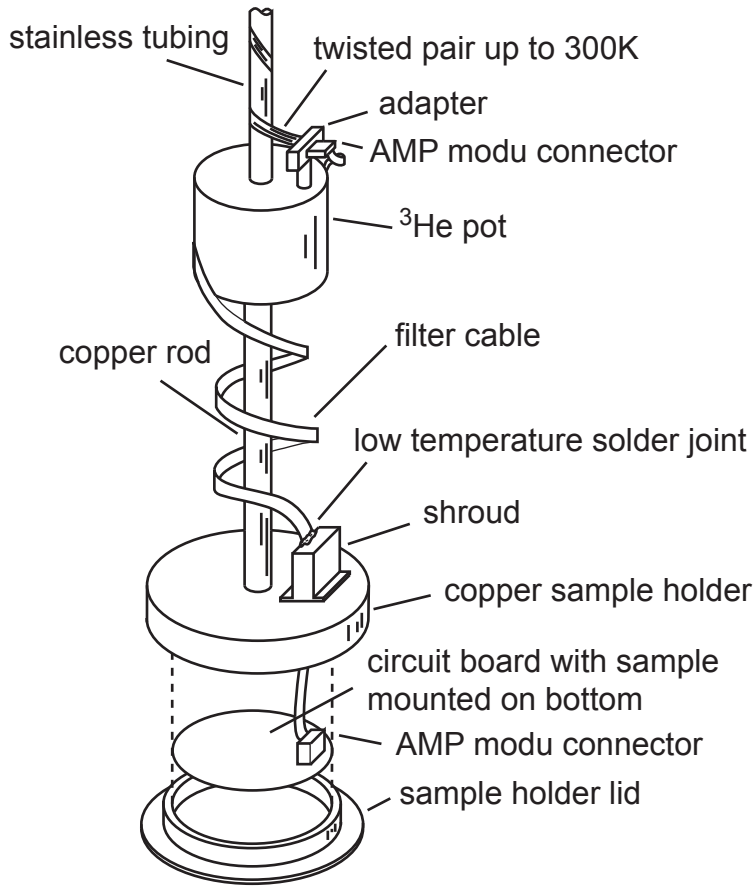

Figure 7.12: Tapeworm filter installation. The "head" of the tapeworm connects to the sample holder, and the main body has the form factor of a ribbon cable, allowing for easy installation by looping it around the cryostat.

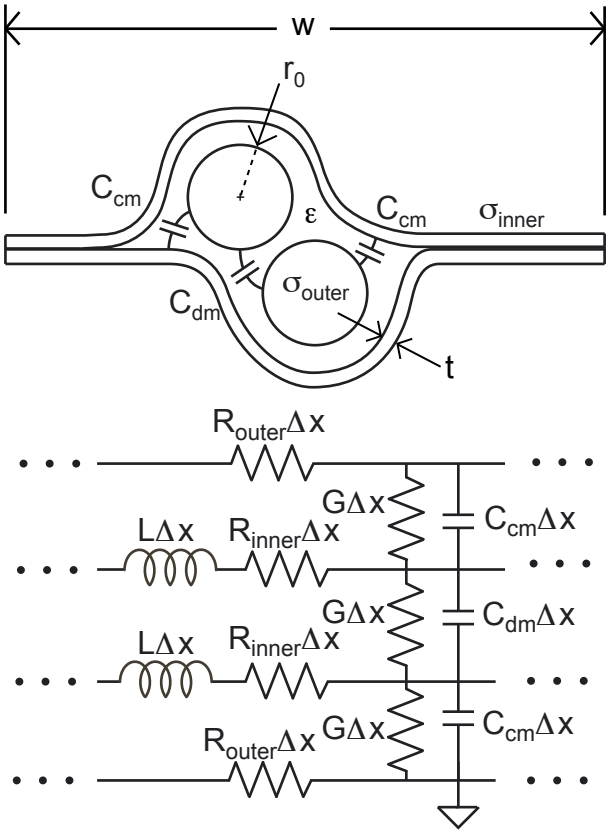

Figure 7.13: Tapeworm RC diagram. This shows the RC line schematic on which the tapeworm model is based, along with the physical origin of the parameters used.

containing the experiment.

The first step in fabrication of the cable is assembling the twisted pairs by fastening the pair at one end and twisting the opposite end with an electric drill motor until the pair is twisted at the desired pitch. The inner conductor of our filter is polyimide-coated manganin wire 4 mils in diameter with a 0.25 mil thick insulating layer. The wire used was 38 Gauge single build polyimide coated manganin wire from MWS Wire Industries, http://www.mwswire.com. Once enough twisted pairs of the right length have been made, they must be arranged in the order in which they will be assembled into the cable and soldered to the ends of the ribbon cable. The solder joints are individually encased in heat shrink tubing to prevent shorting. The entire assembly of wires and ribbon cables is then wrapped up in copper tape by folding the tape twice as shown in Figure 7.11. Once the tape is stuck to itself, form fitting adhesion to the wires may be achieved by pressing the whole assembly with a rolling pin. This gives the cable the profile shown in the cutaway blowup diagram in Figure

7.13, maximizing the capacitance between the inner conductor and the shield. The copper tape is 3M tape #1181, 1" or 1.5" wide, available from Allied Electronics, Allied stock number 617-4710, http://www.alliedelec.com. Note that there are other types of copper tape available that are not suitable because there is a layer of paper between the copper and the adhesive.

The exposed ends of the cable are both ribbon cable, and are easily fitted with AMP modu solderless connectors. AMP sells a wide variety of connectors in the modu line including conversions to various other kinds of connectors and PC board pluggable connectors. This allows for easy connection to whatever connector one may have in the cryostat as well as to the PC board on which the sample is mounted.

In order to make a light-tight connection from the shield of the cable to the sample holder, we use a copper "shroud" through which the cable is threaded which mates to the sample holder. This "shroud" consists of a copper box with a thin slot at one end and an open face surrounded by a flange at the other end (see Figure 7.12.) The copper-shielded ribbon cable part of the cable is passed through the slot in the shroud which is then sealed with Indium-Cadmium low temperature solder (applied with a heat gun). This is done in such a way as to leave a little extra length in the cable so the AMP modu connector can be mated with the circuit board inside the sample holder. The shroud is then bolted over an opening in the sample holder and sealed with an Indium o-ring. When the whole system is assembled, there is light-tight shielding from the beginning of the cable all the way down to the sample holder, surrounding the sample.

To understand the theory of the filter, I consider it to be a set of transmission lines with capacitance per unit length C_{cm} and C_{dm} for common mode and differential mode respectively, resistance per unit length R, and inductance per unit length L. Because of the finite skin depth of high frequency signals, R is frequency dependent. To analyze this line, I follow the standard treatment of the lossy transmission line [56] to find the complex propagation constant $\gamma = \alpha + i\beta = \sqrt{(R(\omega) + i\omega L)(G(\omega) + i\omega C)}$, which corresponds to travelling wave solutions $V(x) = V_0^+ e^{-\gamma x} + V_0^- e^{\gamma x}$.

$R(\omega)$ can be computed from the DC conductivity σ and the fraction of the cross-sectional area that carries current at frequency ω. The skin depth is $\delta = \sqrt{2/\mu_0\sigma\omega}$, where μ_0 is the permeability of the vacuum and σ is the DC conductivity of the material. I then compute the resistance of the inner and outer conductors at finite frequency as follows: $R_{inner} = 1/2\pi\sigma_{inner}\delta_{inner}^2(e^{-r/\delta_{inner}} + (\frac{r_0}{\delta_{inner}}) - 1)$, and $R_{outer} = 1/2\pi\sigma_{outer}\delta_{outer}(1 - e^{-t/\delta_{inner}})$.

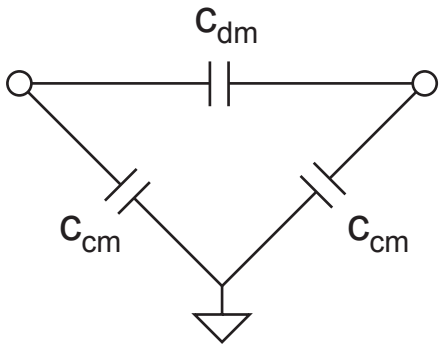

Figure 7.14: Simplified diagram of capacitances used to calculate attenuation.

To find the capacitances per unit length we both compute theoretical values and measure capacitances directly. The measurement of the capacitance is described below in the section on filter testing. The theoretical models are based on various published descriptions of transmission lines [73].

Both the common mode and differential mode are treated using the simplified model shown in Figure 7.14, with a single value for C calculated from the series and parallel combinations of C_{dm} and C_{cm}. I can compute C as follows (see Fig. 7.13):

$$C = \begin{cases} \frac{C_{dm}C_{cm}}{C_{dm}+C_{cm}} + C_{cm} & \text{for common mode} \\ C_{dm} + \frac{C_{cm}}{2} & \text{for differential mode} \end{cases} . \tag{7.1}$$

The total resistance R used in the final calculation is then found from

$$R = \begin{cases} R_{inner} + R_{outer} & \text{for common mode} \\ 2R_{inner} & \text{for differential mode} \end{cases} . \tag{7.2}$$

The shunt conductance as a function of frequency is computed as follows:

$$G(\omega) = \omega C \tan\delta, \tag{7.3}$$

where $\tan\delta$ is the loss tangent of the dielectric material.

The capacitance per unit length C and the dielectric constant ϵ are fit parameters in the model, and the inductance L is calculated from them using the assumption that $L = \epsilon\mu_0/C$. ϵ may be estimated from the value for the polyimide insulation on the wire.

The lumped-element inductance at each end of the line is from the wire that connects the inner conductor of the filter with the inner conductor of the 50 Ω line from the network analyzer. This

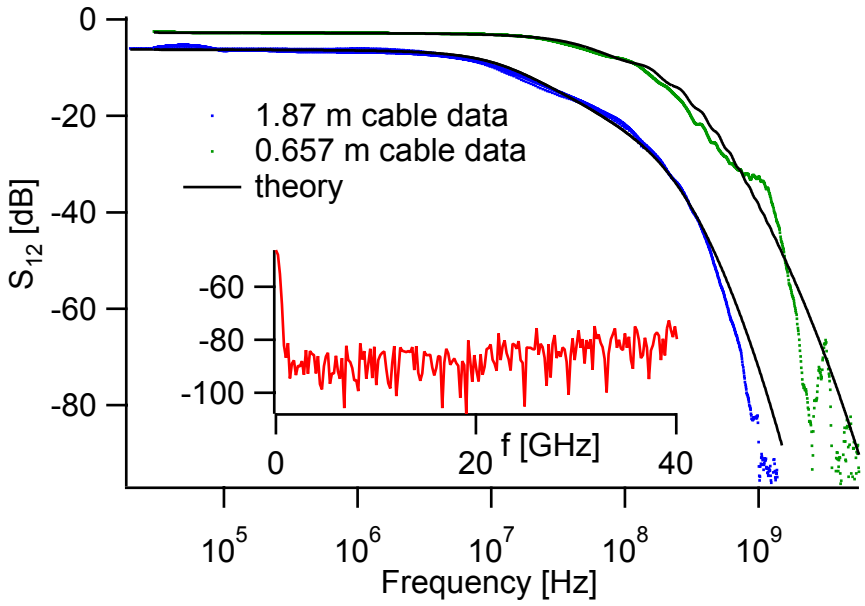

Figure 7.15: Measured throughput of tapeworm filter compared against theory.

can be roughly estimated by assuming that the wire has about a nH per millimeter of inductance, and measuring the length of bare wire. Since there are about two or three centimeters of bare wire at each end, this gives a rough estimate of L_{end} of about 30 nH. Not surprisingly, the best-fit inductance turns out to be a little higher, 45 nH.

With the relevant parameters for the transmission line in hand, I proceed to calculate the propagation constant as described above. From this one may use standard transmission line theory to calculate the insertion loss of the filter cable [56]:

$$\text{insertion loss} = |S_{12}|^2 = |S_{21}|^2 = \left| \frac{1}{\cosh(\gamma l) + \frac{1}{2}(\frac{Z_0}{Z_{net}} + \frac{Z_{net}}{Z_0})\sinh(\gamma l)} \right|^2, \tag{7.4}$$

where Z_{net} is the impedance of the line from the network analyzer in the test circuit (50 Ω). For simplicity, I have shown the insertion loss of the filter cable alone. The actual theory I compare to network analyzer data includes the end inductances.

To test the filter, a test jig was constructed that consisted of a pair of SMA connectors whose center pins were soldered to a pair of wires. The SMA connectors were inset in a groove over which a brass plate was mounted, sealed with a pair of indium o-rings sandwiching the cable. This provided a light-tight seal from one pair of SMA connectors to the other. The transmission as a function of frequency was then measured on a HP8753D network analyzer from 30 kHz to 6 GHz, and from 50

Table 7.1: Table of fit parameters in filter model.

Parameter	Value	Units
σ_{manganin}	2.2×10^6	$\Omega^{-1}\text{m}^{-1}$
σ_{copper}	5.9×10^7	$\Omega^{-1}\text{m}^{-1}$
C	210	pF/m
L	190	nH/m
$\tan(\delta)$	0.01	
ϵ_r	3.5	
w	0.02	m
t	1×10^{-4}	m
L_{end}	45	nH

MHz to 40 GHz on a HP8722D network analyzer. Figure 6 shows a plot of S_{12} at room temperature compared with theoretical transmission for two different lengths of cable. Note that the behavior of the filters is monotonic and very close to the predicted behavior.

By adjusting the parameters slightly, good fits can be found with very reasonable values for all the parameters. The values of the parameters are in Table 7.1.

Note that ϵ_r is approximately the value of the relative dielectric constant for polyimide. In this model, all of the parameters I use are physically reasonable, which may be contrasted to the powder filter, in which it is difficult to construct such a model.

The capacitance per unit length was measured by connecting a 10 kΩ resistor in parallel with the cable to a EG&G 5113 low noise pre-amp in front of a Stanford Research Systems SR760 FFT analyzer. Looking at the RC rolloff of the noise spectrum, it was possible to determine the capacitance per unit length. By connecting the 10 kΩ resistor either between the two conductors of a twisted pair or from one conductor to the shield it was possible to separately measure the common mode and differential mode capacitance.

By neglecting the resistance of the manganin wire and treating the whole cable as just a capacitor, the Johnson noise spectrum can be measured and fit to extract the desired capacitances. In order to eliminate the extra capacitance from the connectors at the end of the cable, different cable lengths were measured and estimates were made of the capacitance per unit length by computing $\Delta C/\Delta l$. This yielded capacitance values of C_{cm}=200 pF/m and C_{dm}=51 pF/m.

The capacitances can also be estimated to check how reasonable our values are by computing certain theoretical limits. In one limit, I consider the line to be a coaxial line with the insulation on the wire surrounded tightly by copper. In the opposite limit, I consider the wire to be sandwiched

halfway between a pair of ground planes pushed up against the outside of the insulation. In the first limit, the capacitance is given by

$$C = \frac{2\pi\epsilon_0\epsilon_r}{\ln(\frac{r+s}{r})} = 1.6 \text{ nF/m}, \tag{7.5}$$

where ϵ_r is the relative dielectric constant, r is the radius of the wire (50 micrometers), and s is the thickness of the insulation (6.4 micrometers.) In the second limit, the capacitance of the so-called "slabline" [73] can be calculated as

$$C = \frac{2\pi\epsilon_0}{\ln(\frac{4(r+s)}{\pi r})} = 150 \text{ pF/m}, \tag{7.6}$$

where we assume that the average relative dielectric constant is 1. As expected, the actual capacitance, 210 pF/m, is between these limits.

I used this filter for all of my measurements, and it has also been used in a variety of single electron transistor and superconducting tunnel junction experiments, and appears to perform as well as the more commonly used coaxial powder filters.

7.6 Matryoshkastat

The cryostat that I built for the very high accuracy thermometry work above 4 kelvin I called the Matryoshkastat, or (матрёшкастат). This name comes from the fact that the nested heat shields inside the inner vacuum can of this cryostat resemble the geometry of the Russian Matryoshka (матрёшка) doll, which consists of a set of nested dolls. The Matryoshkastat is designed to sit in a six inch bore liquid helium dewar, and to have two internested heat shields the temperature of which are independently regulated above 4 kelvin.

The Matryoshkastat consists of an insert designed to fit in a six inch bore dewar. The depth of the dewar with no belly is 49.5 inches. The top of the dewar has a 7.75 inch diameter bolt circle of 10-32 threaded holes, and an o-ring seal with a diameter of 6.625 inch diameter. The vacuum can is hung from a pair of 3/4 inch thin wall stainless tubes that also conned the vacuum space with the warm feedthroughs. These feedthroughs are fitted with KF-16 flanges which are used for getting DC wiring into the can as well as for the pump-out for the can. There are also line-of-sight ports going from KF-40 flanges at room temperature down to indium-sealed flanges on the 4 K plate. One of these is used for Rf lines, and the other is a spare which could be used for adding a pickup tube for a 1K pot by a future user. Two blank stainless steel flanges were made by the Yale physics machine

shop, and I made one brass one for the RF feedthrough. The other ports going down from room temperature are four 0.375 inch outer diameter tubes that go down through the baffle stack from cajun fittings on the top plate. The exact mechanical details of the Matryoshkastat are not included here for brevity, and are available in a manual as a separate document.

The structure inside the vacuum can consists of a removable pair of oxygen free high conductivity (OFHC) copper plates linked by stainless steel tubes to each other and to a brass mounting plate. A pair of home-made OFHC copper heat shields then get screwed to the copper plates to make two large, enclosed isothermal surfaces. Each copper plate has its own heater wire connected to room temperature which allows for independent temperature regulation. If this cryostat were to be used for hydrogen triple point operation, the outer shield would be held at 12 K or so, while the inner shield would be regulated to be at the triple point (which would hang from the inner shield) by a differential thermocouple.

The temperature of the two stages of the cryostat are regulated with a Cryocon 32 temperature controller. The output of the controller puts current through either of two heaters that consist of manganin wire wrapped around the upper and lower copper plates to which the heat shields are attached. One channel of the Cryocon 32 is only designed to put a voltage into a very high input impedance circuit and is not capable of sourcing enough current to directly heat the cryostat. The current from this channel is boosted using a buffer made from an operational amplifier powered by an external DC power supply.

7.7 Secondary Thermometry

A variety of secondary thermometers were used in this work both for temperature regulation and for carrying out temperature comparisons of the SNT. The thermometers used for temperature comparisons were all either rhodium iron resistance thermometers or ruthenium oxide resistance thermometers. For the first generation of temperature comparison experiments, performed in the Kelvinox dilution refrigerator and the Heliox pumped helium-3 cryostat, an RX202A-AA ruthenium oxide sensor from Lakeshore was used as a comparison between 4 kelvin and 50 milikelvin, which is calibrated from 50 milikelvin through 40 kelvin. In this set of measurements, the temperatures above 1.4 kelvin was measured with a RF-800-4-1.4L, which is calibrated from 1.4 kelvin to 325 kelvin. Lakeshore sells all of their sensors in both an “uncalibrated” version, which operate off of a standard curve and are not individually calibrated, and a version that are individually calibrated, which

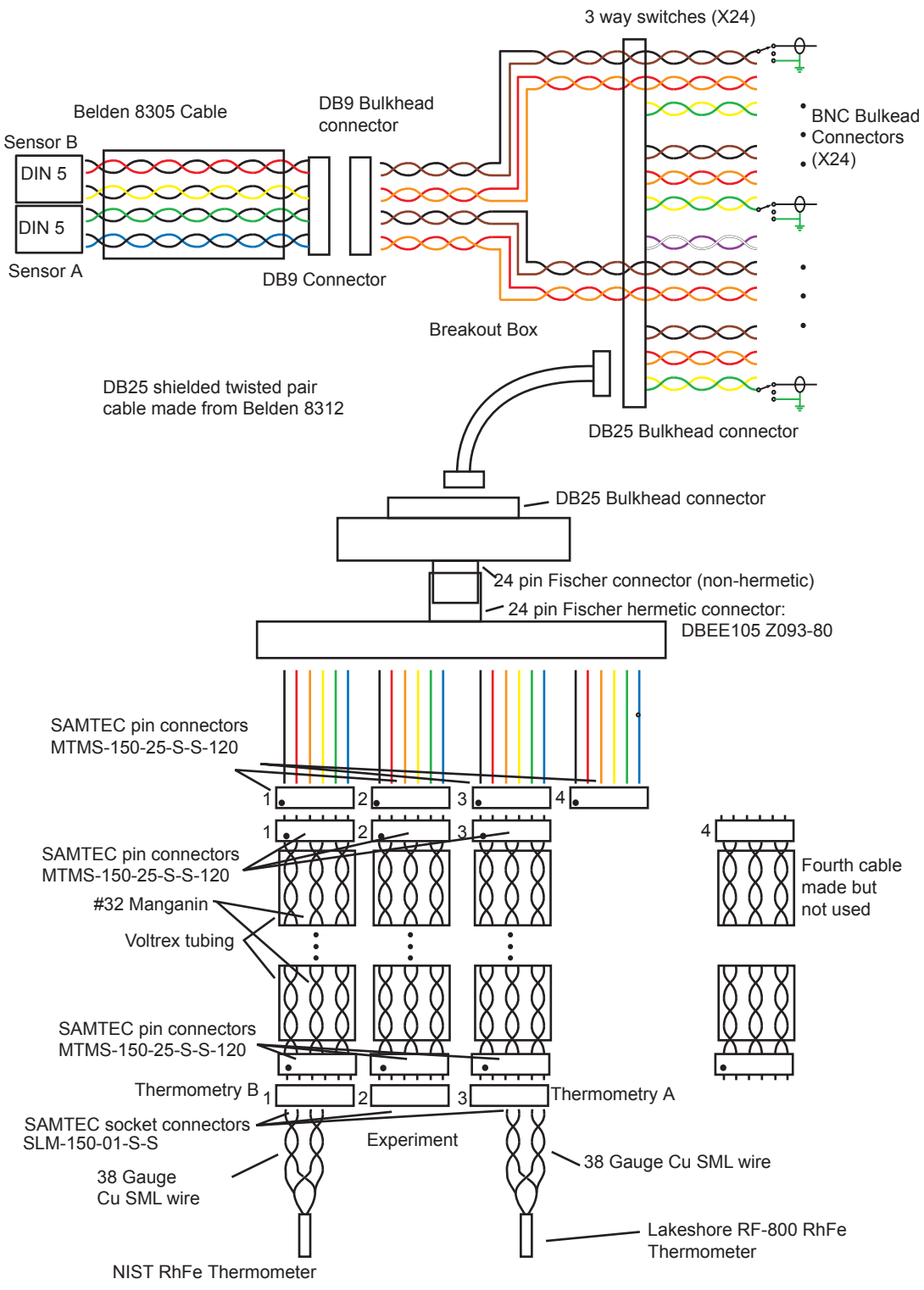

Figure 7.16: Schematic of Matryoshkastat wiring.

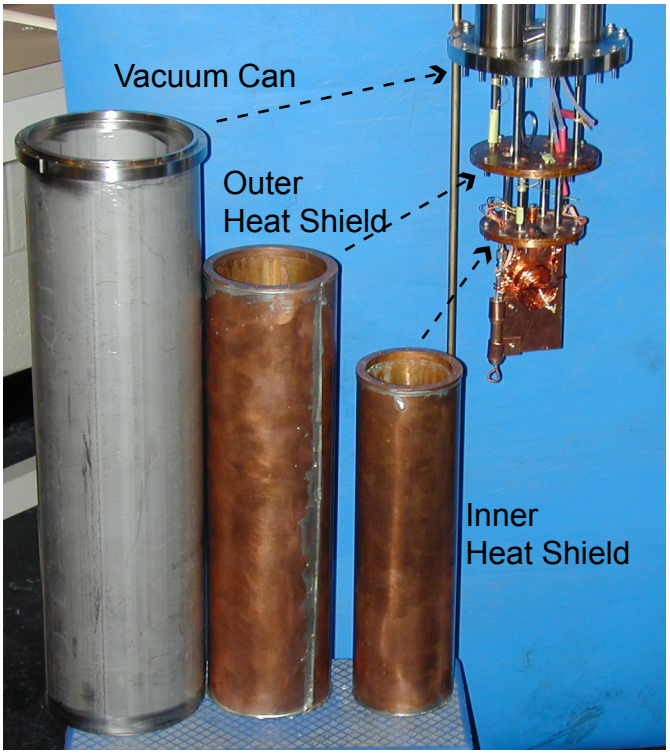

Figure 7.17: Internested cans. This photograph shows how the Matryoshkastat got its name. The two copper heat shields sit in vacuum under normal operation.

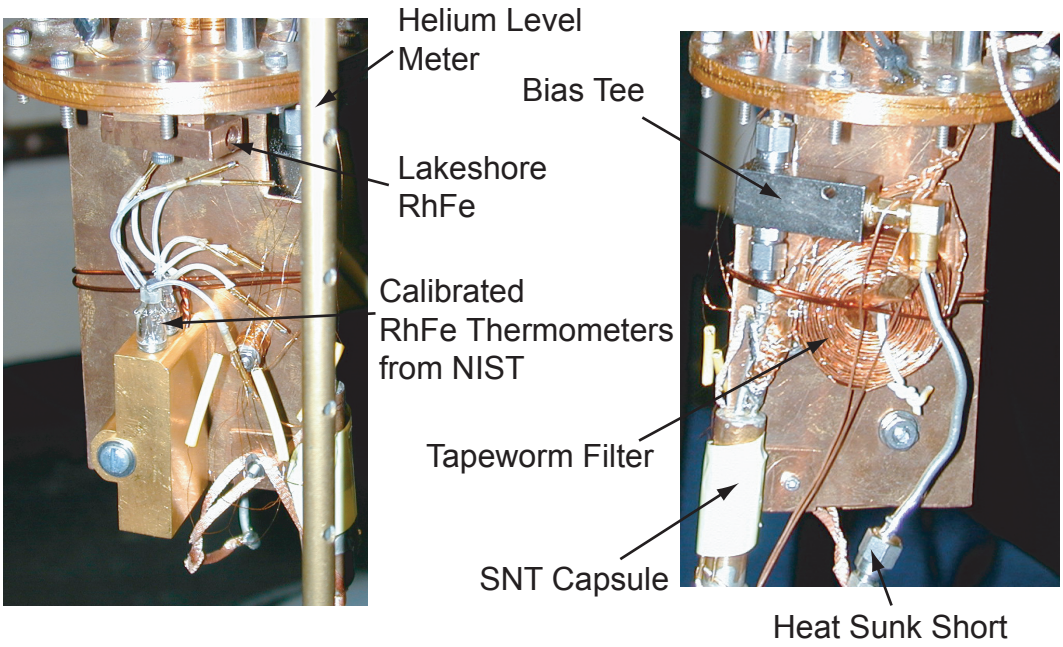

Figure 7.18: Close-up photo of thermometer comparison at base of Matryoshkastat. All thermometers are securely attached to a piece of OHFC copper sheet, and the secondary thermometers are all snugly fit with vacuum grease into OFHC copper blocks.

Table 7.2: Table of uncertainties of commercial secondary thermometers. These data are taken from the Lakeshore data sheets.

Thermometer	0.05 K	0.3 K	1.4 K	4.2 K	20 K	77 K	300 K
RX202A-AA	±3 mK	±4 mK	±5 mK	±16 mK	±37 mK	-	-
RF-800-4-1.4L	-	-	±7 mK	±7 mK	±10 mK	±13 mK	±23 mK

were used here. Lakeshore maintains an internal set of standards based on platinum, germanium, and rhodium iron resistance thermometers which they have calibrated at either NIST or NPL with respect to ITS-90 in the range above 0.65 kelvin and the PLTS-2000 in the range below 0.65 kelvin. Lakeshore provides resistance and temperature data taken during the calibration run for each sensor they sell. They also provide the coefficients of a Chebychev polynomial which can be used to interpolate the resistance-temperature curves and give a temperature value for any given resistance value.

Table 7.2 gives the stated calibration uncertainties for the Lakeshore thermometers given in their documentation. These thermometers were read out by applying a current bias with a Yokogawa current source and measuring the voltage across the sensor and the voltage across a bias resistor, generally at room temperature. The bias was reversed periodically to remove offsets, the resistance

was calculated from the ratio of the voltages, and temperature was determined from that resistance.

Below 50 milikelvin, I had to rely on the thermometry provided by the cryostat manufacturers both for the Oxford and the Cryoconcepts dilution refrigerators. Both of these were ruthenium oxide resistance thermometers which were measured and converted to temperature using resistance bridges that were sold with the respective cryostats. The Oxford thermometry was calibrated against a nuclear orientation thermometer when the cryostat was commissioned in 1999. Between that time and 2002 when I did my measurements in the Kelvinox, an error in the wiring in the Oxford electronics was discovered (a wire that should have been soldered to pin 6 was soldered to pin 9 and vice versa), and fixing this could have changed the calibration of the resistance readout. Also, three years is enough time for potentially significant drift in the calibration. Because of these potential systematic effects, it is difficult to put accurate error bars on this temperature measurement. The better low temperature work I did was in the cryoconcepts dilution refrigerator, comparing against the ruthenium oxide thermometer that came with that system. Unlike the run in the Oxford system, this run was immediately after the refrigerator had been purchased, and we were given detailed information about the calibration by Patrick Pari, one of the scientists at Cryoconcepts. The Cryoconcepts ruthenium oxide sensor was calibrated in the range from 9 mK to 30 mK using a nuclear orientation thermometer, and in the range from 50 mK to 4.2 K using a GR-200A germanium thermometer originally calibrated by Lakeshore Cryotronics. Data from 30 mK to 50 mK were interpolated using the higher and lower temperature data. The stated fractional calibration uncertainty of the ruthenium oxide thermometer was approximately 10% in the range where data were taken.

One other thermometer that was used for temperature regulation of the outer heat shield in the Matryoshkastat was a Lakeshore DT-670C-BO diode thermometer. This thermometer, which has a range from 1.2 K up to 500 K, was read out with a four wire measurement connected to the Cryocon 32 temperature controller. This is not an individually calibrated sensor, and the calibration uncertainties are higher than for the resistance thermometers from Lakeshore. The uncertainty of this temperature was not at all important, however, since the role of this temperature stage was just to provide an approximate temperature slightly cooler than the inner heat shield.

The high accuracy temperature comparisons performed in the Matryoshkastat used a rhodium iron resistance thermometer calibrated at NIST directly off of the ITS-90. This sensor (serial number B115) was measured using the Agilent nanovoltmeter, and a temperature controlled resistance stan-

dard, as shown in Figure 7.19. This sensor is approximately 100 Ω at room temperature, and 12 Ω at 13.8 K. By measuring the ratio of the voltage across the rhodium iron resistance thermometer to the voltage across the resistance standard, and reversing the bias, the resistance of the thermometer may be computed accurately using the formula

$$R_{RIRT} = \frac{V^{+}_{RIRT} - V^{-}_{RIRT}}{V^{+}_{std} - V^{-}_{std}} R_{std}, \tag{7.7}$$

Where R_{RIRT} and R_{std} are the resistances of the rhodium iron resistance thermometer and the standard resistor and $V^{\pm}_{RIRT}$ and $V^{\pm}_{std}$ are the measured voltages across the rhodium iron resistance thermometer and the standard resistor for positive and negative current bias. The resistance of the standard, R_{std} is 100.00047 Ω. As was mentioned in Chapter 4, the nonlinearity of the analog to digital conversion on the HP 34420A nanovoltmeter is specified at 0.8 ppm of the reading plus 0.5 ppm of the range. Thus the dominant uncertainty in the temperature measurement is in the calibration uncertainty of the rhodium iron resistance thermometer, which is better than 30 ppm over the range where I took data for this work. This sensor was held by friction and a thin layer of vacuum grease into a tight clearance hole in a gold plated copper block which was fastened to an OFHC copper sheet that extended down from the bottom plate of the Matryoshkastat, inside the inner heat shield.

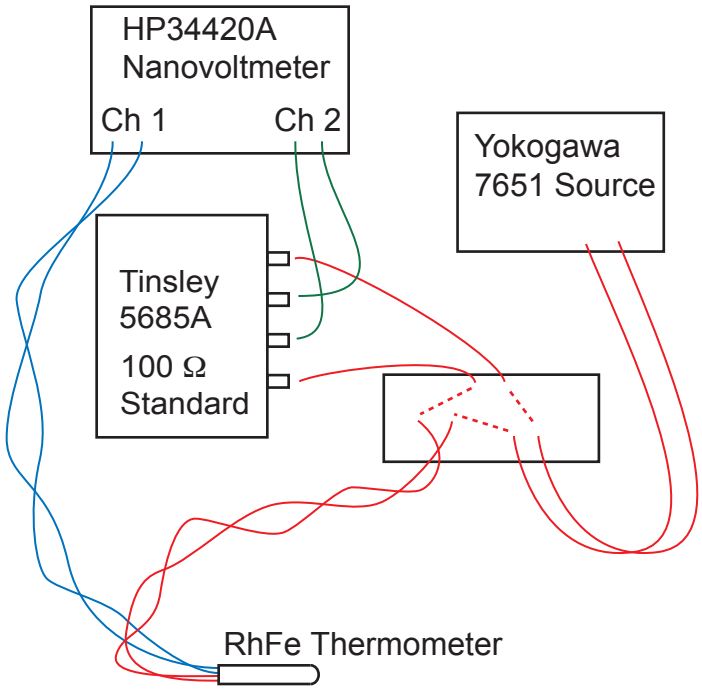

Figure 7.19: Schematic of precision resistance measurement. The Yokogawa was set to put out ± 500 μA excitation, and the nanovoltmeter was set to the 100 mV scale.

Chapter 8

Measurements

8.1 Introduction

The bulk of the work presented in this thesis consists of comparison of the SNT noise curve against theory at various temperatures and comparisons of the extracted fit temperature with various secondary thermometers described in the previous Chapter. In this Chapter, I first describe how noise data were recorded and compared with theory and present some representative data from two temperatures and from the statistical analysis of the noise fit. This first Section also shows how the SNT has been used to measure temperature in real time. The next Section describes the detailed temperature comparisons that were made to secondary thermometers at various temperatures. The effects of finite frequency on noise that are described in Chapter 3 are then demonstrated experimentally, and I show that these effects can be not only accounted for in temperature measurements, but are potentially useful. Next, I present measurements that characterize how the coupling of the junction to its RF environment changes with voltage, and describe how this difficulty might be overcome. Finally, I present DC data showing the detailed conductance physics of the junctions studied here, and demonstrating that the junctions made by Ruggiero et. al. [64] with manganese doped aluminum can be non superconducting at all accessible temperatures with no magnetic field applied. All of the RF data on SNT junctions taken below 1 K had a magnetic field sufficient to suppress all traces of superconductivity, generally about half a Tesla.

8.2 Noise Curve Tests

The first experimental question which must be answered before the SNT can be evaluated as a thermometer and as a possible standard is how well the voltage dependence of the noise can be

understood. This is made difficult by the subtle effects of various types of nonlinearity which can slightly bend the shot noise curve either up or down. These effects are discussed in more detail later in this Chapter. The basic agreement of the noise curve to theory was shown clearly at low levels of uncertainty in Chapter 1.

Figures 8.2 and 8.1 show some of the best data demonstrating the functional form of the noise with high precision. These data are taken by recording many individual noise-voltage curves on the computer and averaging them together. Each noise-voltage curve is taken by stepping between a finite voltage and zero while that voltage is swept from zero up to the maximum in the following sequence:

$$V = \{\Delta V, 0, -\Delta V, 0, 2\Delta V, 0, -2\Delta V, 0, 3\Delta V, 0, -3\Delta V, 0, ..., N\Delta V, 0, -N\Delta V, 0\}, \tag{8.1}$$

where ΔV is the distance in voltage between adjacent points, and 2N is the total number of nonzero voltages measured. After data have been recorded in this manner, the differences of the voltages and of the powers between adjacent points in the above sequence are computed and recorded. Thus the y value of each point in the final curve represents the difference between the power at a finite voltage and at zero voltage, and the x value represents the difference between the measured voltage and the voltage when the current is set to zero at the top of the cryostat. This method removes offsets in power, offsets in the voltage measurement, and any slow drifts in both of those offsets, just as a lock-in amplifier would do. We generally call this method either the "tic toc" method or the digital lock-in method.

Figure 8.3 shows over four decades in temperature data in agreement with the predicted functional form. This is the most accurate and widest temperature range verification of the junction noise so far. Also note that while the data shown in Figure 8.3 only go to a temperature of 37 mK, the data shown in Figure 8.13 show data in the same form verifying the functional form of the noise down to 10 mK, with appropriate corrections for the finite frequency of the measurement (see below).

The data taken with the tic toc method have lost all information about the noise temperature of the amplifier, but this has the advantage that it decreases the number of fit parameters required to determine temperature. In the absence of offsets, only the temperature and gain need be used as fit parameters. In the apparatus used here, there are typically a few tens of nanovolts of voltage offset in the voltage on the current bias side of the wiring, which the tic toc method does not remove. Thus three parameters are needed to fit the data: temperature, gain, and voltage offset. The fit

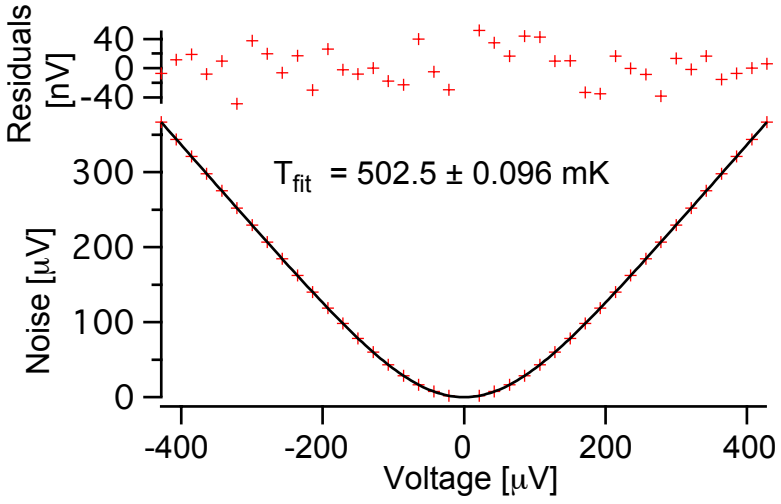

Figure 8.1: Data from a long integration time measurement in the Kelvinox. The fit parameters from this data set were T = 0.5025 ± 9.6X10^{-05} K, and offsetvoltage = -18 nV ± 4.3 nV.

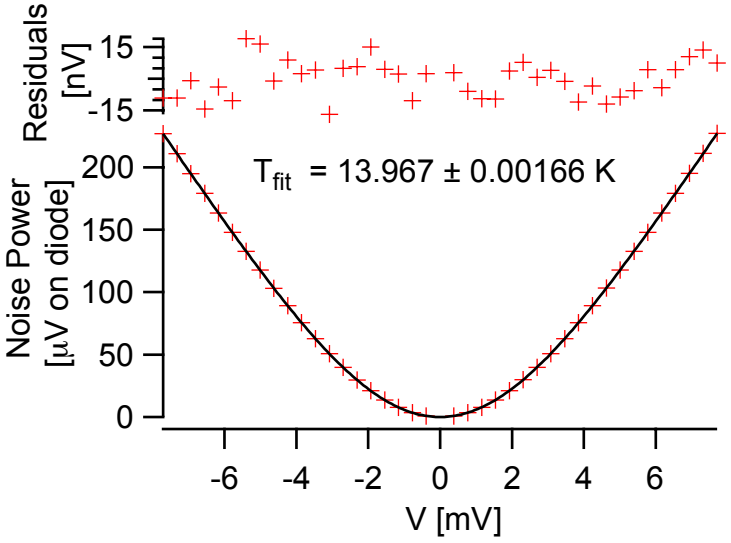

Figure 8.2: Data from long integration time measurement in the Matryoshkastat. Note that as with the 0.5 K data above, the statistical uncertainty determined from the fit is much smaller than the systematic errors discussed in Chapter 4.

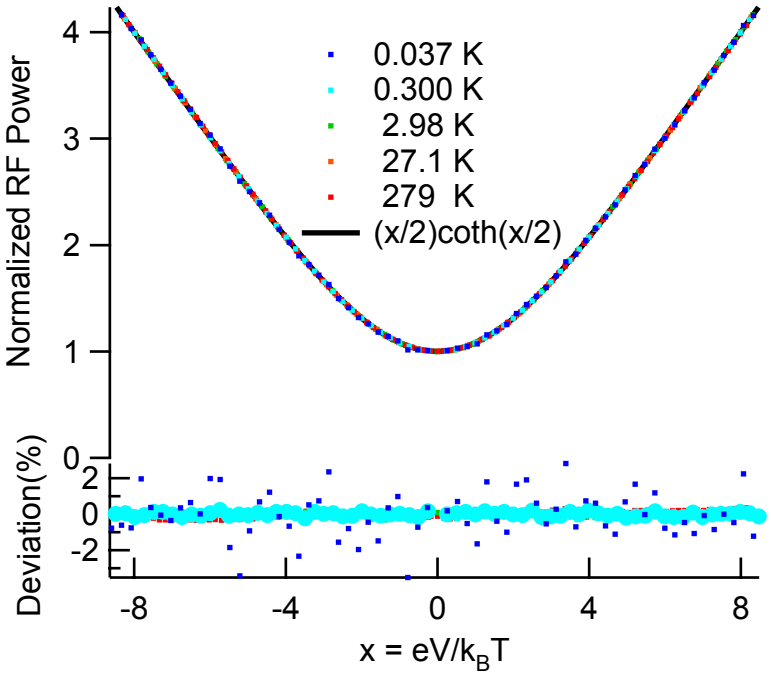

Figure 8.3: Noise data at different temperatures, with voltage normalized to temperature and noise power normalized to the Johnson noise. This remarkable agreement with the theoretical functional form over more than four decades in temperature is the most accurate and broadest temperature range measurement of the noise from a tunnel junction so far.

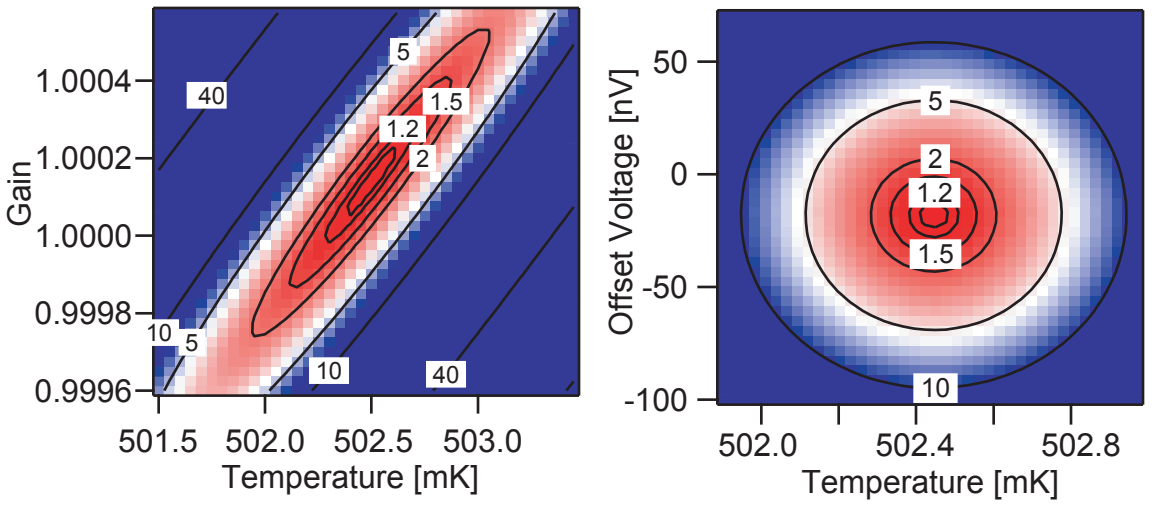

Figure 8.4: Contours of χ^2 from long integration time data from kelvinox at 0.5 K shown in Figure 8.1. Note that the offset voltage and the temperature are uncorrelated. For brevity I have omitted the contours of offset voltage and gain, however they are also uncorrelated.

function used is

$$= G\left[\frac{e(V-V_{offset})}{k_BT}\coth\left(\frac{e(V-V_{offset})}{2k_BT}\right)-T\right] \tag{8.2}$$

. The data shown in Figures 8.2 and 8.1 have been fit to this function.

These data appear to agree to within 100 parts per million to the predicted shot noise function. However, the agreement shows the potential peril of shot noise thermometry. The data shown in Figure 8.2 were taken at a temperature that was known to within better than 100 parts per million, and yet the fit temperature above and the temperature as with a calibrated rhodium iron resistance thermometer differed by about 0.7 %. This is probably due to a combination of subtle nonlinearity effects and DC voltage offsets discussed in Chapter 4.

It is now worth taking the time to discuss the statistics of this fit. The process of finding fit parameters from a least squares fit consists of trying to find a global maximum of the function χ^2, as was discussed in detail in Chapter 5. Examining the contours of the χ^2 surface is useful in determining the quality of the least squares fit. Figure 8.4 shows such contours for the fit of the data shown in Figure 8.1. On a small enough scale, it is typical for the χ^2 contours of any pair of variables to be ellipses near the optimal values. The eccentricities of these ellipses characterizes the correlation between the variables. If a pair of variables are perfectly uncorrelated, the contours will appear as circles, and in the limit as they become totally correlated the ellipses stretch out into

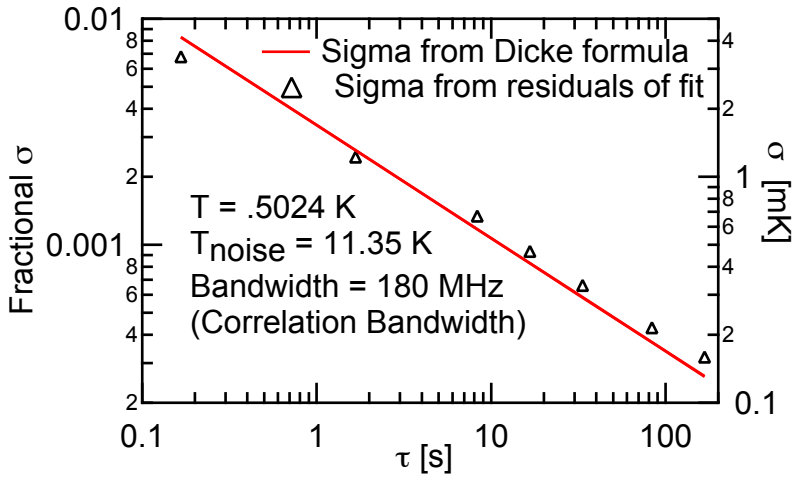

Figure 8.5: Standard deviation of temperature fit as a function of integration time per point. the red line shows the expected result from the Dicke radiometer formula introduced in Chapter 1.

parallel lines and the variables may not be independently determined. The right inset of Figure 8.4 shows that the voltage offset and the temperature are totally uncorrelated. The left inset shows that the gain and temperature are in fact correlated to some degree, but that the overall shape of the curves are well-behaved, and are as expected based on the analysis in Chapter 5.

The data analyzed above were taken over several hours, and were recorded in a series of separate data files, and so it is possible to evaluate the behavior of the statistics of these data as a function of time. Figure 8.5 shows how the uncertainty of the noise measurement decreased with time, and compares it to the Dicke result [18]. This is some of the highest accuracy and precision shot noise data taken so far. This excellent agreement of the integration of the noise data with the Dicke result shows that it is possible to keep improving statistical precision in an SNT measurement by simply waiting longer, as was discussed in more detail in Chapter 5.

While the above measurements were necessary to evaluate the SNT and verify the physics used to extract temperature from the data, it is possible to optimize the data taking for more rapid determination of temperature. In chapter 5 I described a method that involves only stepping the voltage between two nonzero points and zero voltage to determine temperature quickly. I have employed this to record temperature as a function of time at various temperatures. Figure 8.6 shows such a temperature time series at various temperatures in the Cryoconcepts dilution refrigerator. Figure 8.7 shows such a temperature time trace at room temperature in the lab. These data show

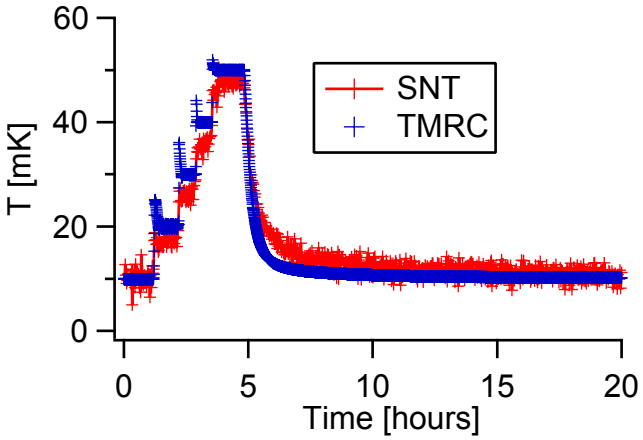

Figure 8.6: Timetrace of temperature in Cryoconcepts dilution refrigerator. This demonstrates the operation of the SNT as a real-time thermometer at very low temperatures.

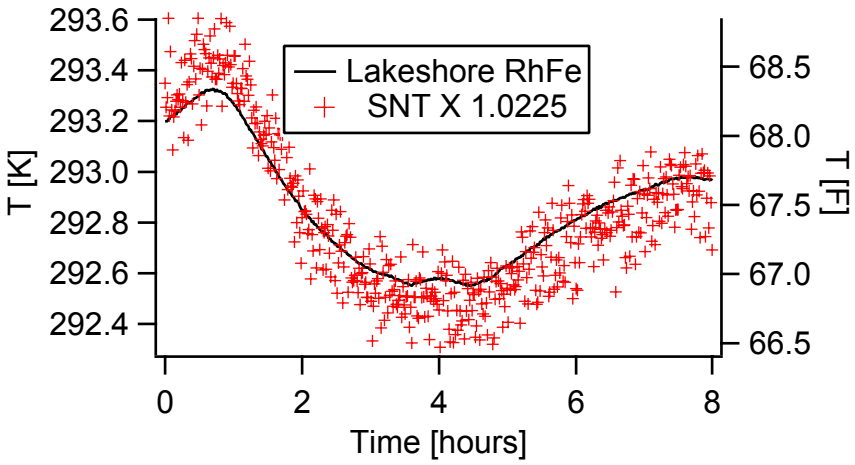

Figure 8.7: Timetrace of SNT temp at room temperature compared against lakeshore thermometer. This demonstrates the operation of the SNT as a real-time thermometer at room temperature, although a correction factor is needed to make the temperature agree exactly with the true temperature. This data set also show typical diurnal variations of temperature in the Schoelkopf lab, in Becton Center, where all the measurements in this thesis were carried out.

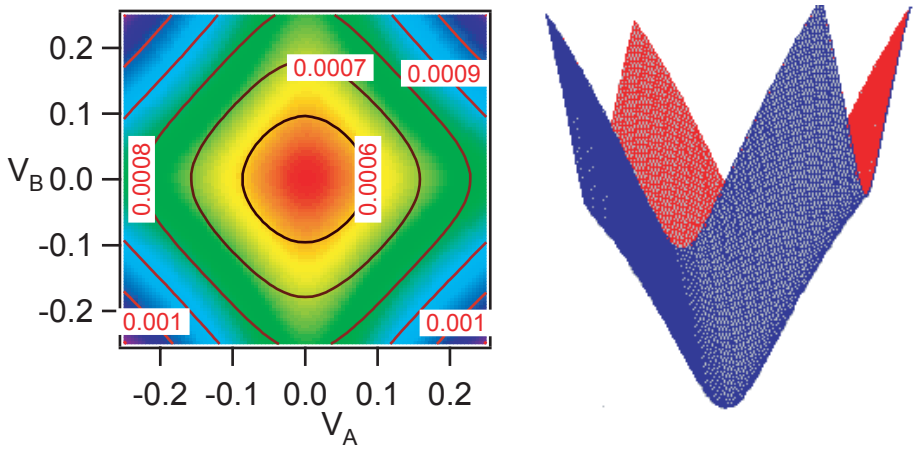

Figure 8.8: Noise bridge data at room temperature. This shows experimental data from the noise bridge described in the previous chapter displayed both as a contour plot and as a surface plot. This was intended only as a proof of concept, and no effort was made to extract temperature from the shape of the contours. It is clear that this apparatus is functional, however, and could be used to eliminate RF chain nonlinearities in the future.

that while the SNT does not read accurately at room temperature, when a correction factor is applied, it does follow the correct temperature faithfully, and with reasonable signal to noise. They also are a record of the size of typical daily temperature drifts in the lab in Becton.

Finally, one of the noise curve comparisons I did was to test the noise bridge described in Chapter 7. Figure 8.8 shows data from the noise bridge. This is simple proof of concept data, and I did not make any effort to really extract temperature from the noise contours. This method only attempts to deal with the nonlinearities in the RF chain, and does not help with the more important nonlinearities caused by the changing impedance of the junction.

8.3 T vs. T Comparisons

Once the basic operation of the SNT has been established, it is necessary to compare the extracted fit temperature to secondary thermometers. The secondary thermometers used for comparisons are described in the previous Chapter of this thesis. Figure 8.9 shows an overview of the comparisons. The data on this plot represent comparisons to the Lakeshore RF-800 calibrated rhodium iron thermometer and Lakeshore RX202A ruthenium oxide thermometer made in the Heliox pumped helium-3 cryostat, and comparisons to the calibrated ruthenium oxide thermometer from Cryoconcepts made in the Cryoconcepts dilution refrigerator. Overall, these data agreed to within the uncertainty of

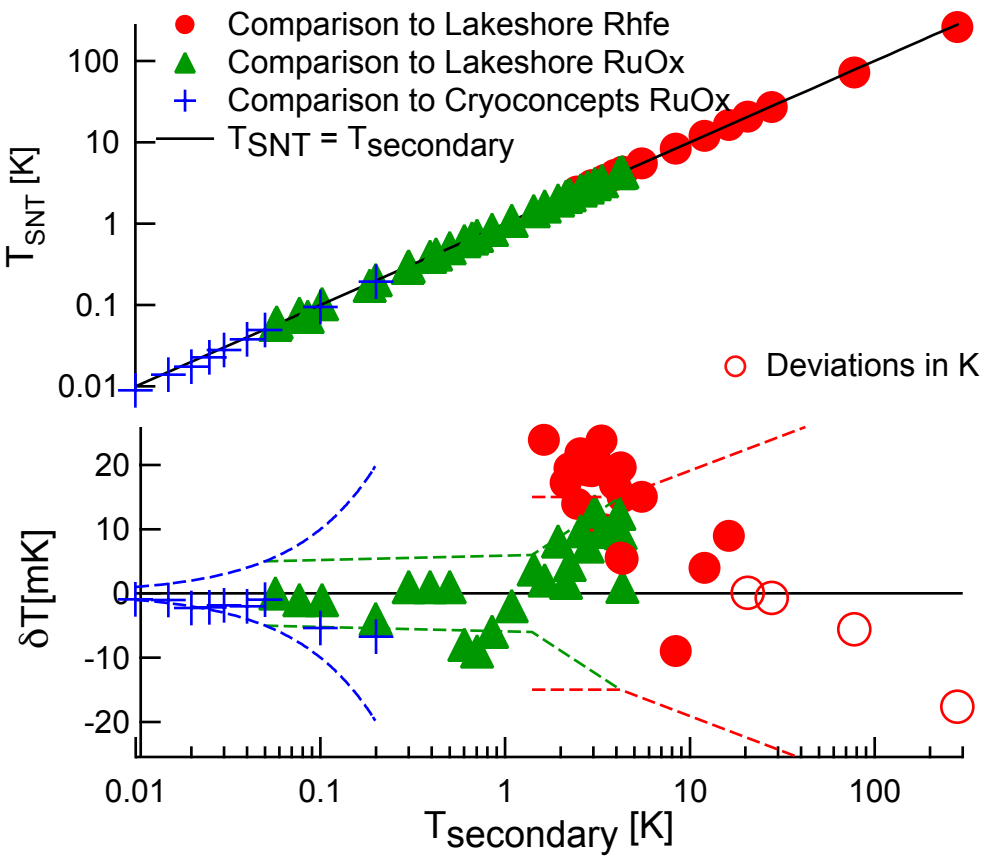

Figure 8.9: This is a plot of several temperature comparisons. SNT fit temperature is plotted on the vertical axis, and temperature determined from secondary thermometers is plotted on the horizontal axis. Dotted lines indicate stated calibration uncertainties of the secondary thermometers. Open circles indicate deviations in K, not mK.

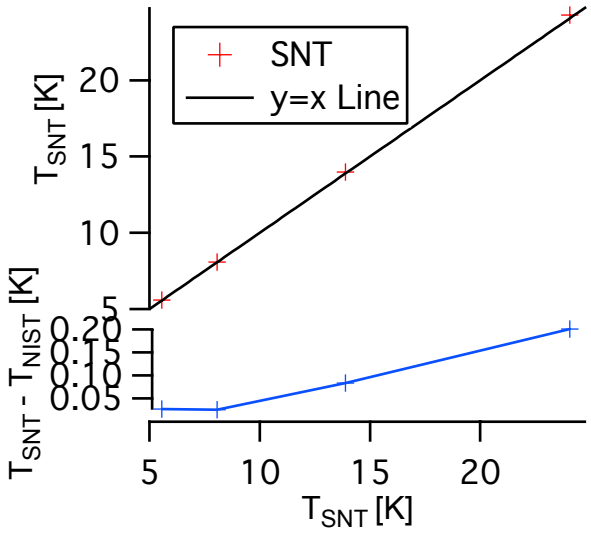

Figure 8.10: This shows a temperature comparison similar to Figure 8.9, only for the high accuracy comparisons to the NIST thermometer carried out in the Matryoshkastat. The SNT indicates a temperature that is consistently high relative to the NIST thermometer, which is probably primarily due to voltage errors in the leads, as discussed in Chapter 4. No error bars are shown since the systematic errors vastly exceed statistical errors.

the secondary thermometer up through approximately 20 K. However, I carried out more accurate comparisons with a rhodium iron resistance thermometer calibrated at NIST against the ITS-90. The results of this comparison are shown in Figure 8.10. Although the statistical uncertainty of the SNT measurement was in the hundreds of parts per million or better and the accuracy of the secondary thermometry was also generally better than 100 parts per million, these data differ by as much as 0.7%.

It is worth noting that the SNT data consistently read high relative to the temperature as measured by the NIST resistance thermometer. The sign of this difference is consistent with a voltage drop between the junction and the voltage leads as described in Section 4.5, and the size of the effect is roughly consistent with estimates made in that section. If that were the only effect at work, however, the fractional size of the temperature error would be constant with temperature, which is not the case. Thus, there is clearly some other effect at work here. This effect is probably a combination of different nonlinear effects. I was unable to separate the different nonlinear effects with a sufficient degree of accuracy in this work to correct for them, but I describe measurements of the frequency dependent nonlinearities later in this Chapter.

Figure 8.11 shows a time series of rhodium iron resistance thermometer data from the Ma-

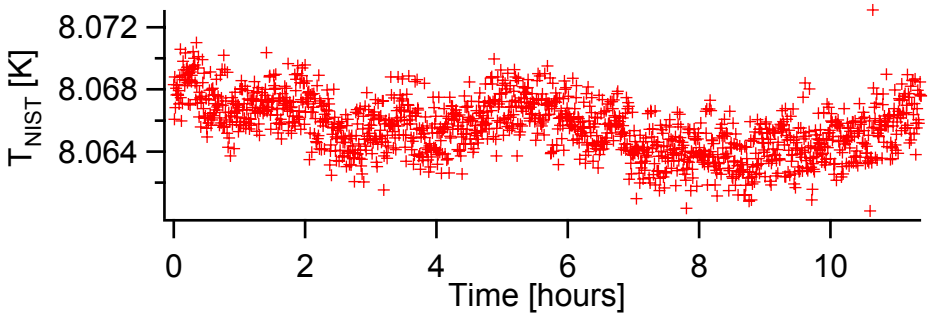

Figure 8.11: Time series of Matryoshkastat temperature measured on the NIST thermometer at approximately 8 kelvin. This data set was recorded while regulating the Matryoshkastat at a fixed temperature, and the variability in temperature shown here is typical. There was always a random drift on the order of 1 to 4 mK over a few hours in the Matryoshkastat.

tryoshkastat during a temperature comparison run. This shows the ultimate limits of the temperature regulation in the Matryoshkastat, and hence one of the ultimate limits on the temperature precision of any comparison. Since accuracy was never at the level of single milikelvins in this work, this level of drift was not ever a dominant problem.

8.4 Finite Frequency Effects

Most of the noise data presented in this thesis were taken at a frequency range centered around about 450-500 MHz, which corresponds to about a 22-24 mK temperature. Thus, at the base temperature of the dilution refrigerator, hf/k_BT was more than 2, and the finite frequency effects are very important. In this temperature/frequency regime, a majority of the noise being measured is from the zero point motion of the electromagnetic modes of the sample, since there is not enough thermal energy to excite very many photons, as can be seen in Figure 3.8 in Chapter 3. In this regime, the finite frequency formula for the noise must be used, which is

$$S_I(f,V,T) = \frac{2k_BT}{R}\left[\frac{eV+hf}{2k_BT}\coth\left(\frac{eV+hf}{2k_BT}\right) + \frac{eV-hf}{2k_BT}\coth\left(\frac{eV-hf}{2k_BT}\right)\right]. \quad (8.3)$$

In practice, the noise measurement consists of the weighted sum of measurements at different frequencies over some frequency band defined by the band of the amplifier and the circulator. This band is shown in Figure 8.12.

The noise data are fit to a sum of Equation 8.3 with different frequencies weighted by the numbers shown in the bar graph in Figure 8.12. When the data are fit with these corrections, they agree

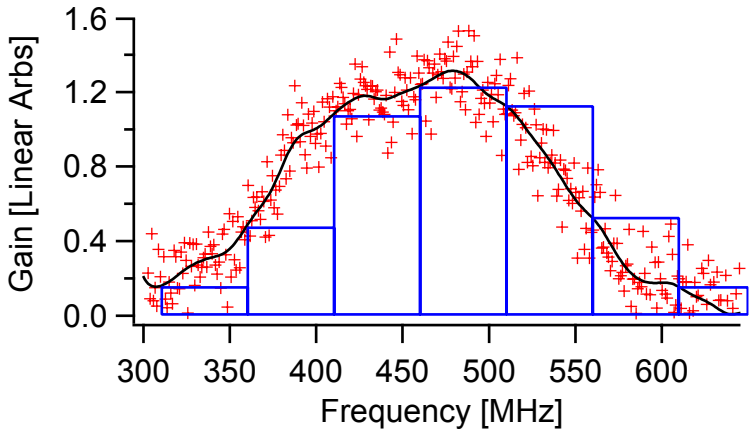

Figure 8.12: Gain as a function of frequency. The upper left corners of the bars indicate the gain and frequency values used in the finite frequency fit function. Data were also fit with a single frequency fixed at 450 MHz, which gave answers that were identical to within the statistical uncertainty of the SNT measurement.

with the theory, and the fit temperature agrees with the temperature as measured by the secondary thermometry to within the calibration accuracy. Figure 8.13 shows such a data fit at a series of temperatures, with the voltage data normalized to temperature and the noise data normalized in such a way as to make the shot noise limit for all curves identical, i.e. by dividing by the gain. In these normalized units, the zero voltage noise rises up above one as the temperature gets low compared to frequency. This is the very beginning of the frequency dependence of the noise shown in Figure 3.8, $hf/2k_BT \coth hf/2k_BT$.

Once temperatures have been extracted from noise data, they are compared to the Cryoconcepts ruthenium oxide thermometer. This comparison is shown in Figure 8.14. The stated calibration uncertainty of the ruthenium oxide was about 10 % over the whole range, with is consistent with what was observed. It is also possible to see interesting quantum effects in the data displayed in Figure 8.14. The red triangular markers show what temperature would be extracted if the zero frequency result were used. With this model, the effective temperature saturates and deviates from the true temperature in a way that becomes more pronounced as temperature gets below hf/k_B, which is shown by the green dotted line.

Another frequency dependent effect which is of potential interest is that of irradiation of the junction by high frequency microwaves. As was discussed in Chapter 3, the expression for the noise

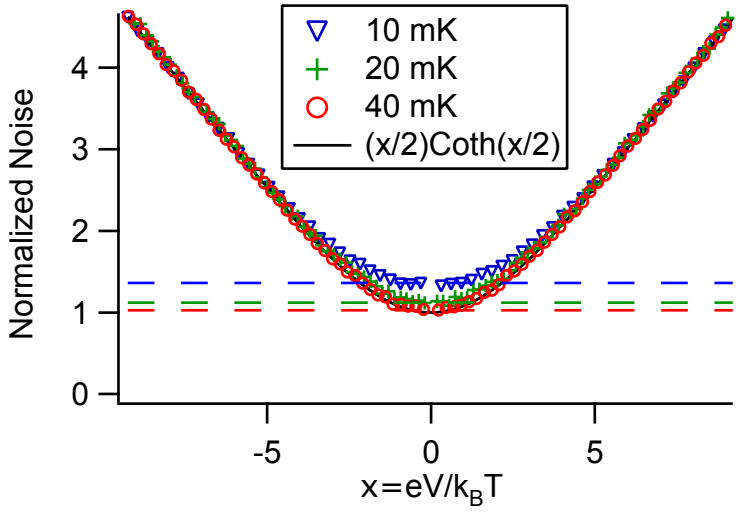

Figure 8.13: Normalized noise at temperatures near the base temperature of a dilution refrigerator. These data were prepared in the same manner as those in shown in Figure 1.9, by normalizing gains of all curves and removing offsets between the shot noise limits of the curves. The important point to notice here is that even in the normalized form, the noise changes as temperature becomes lower than the quantum crossover temperature corresponding to the measurement frequency.

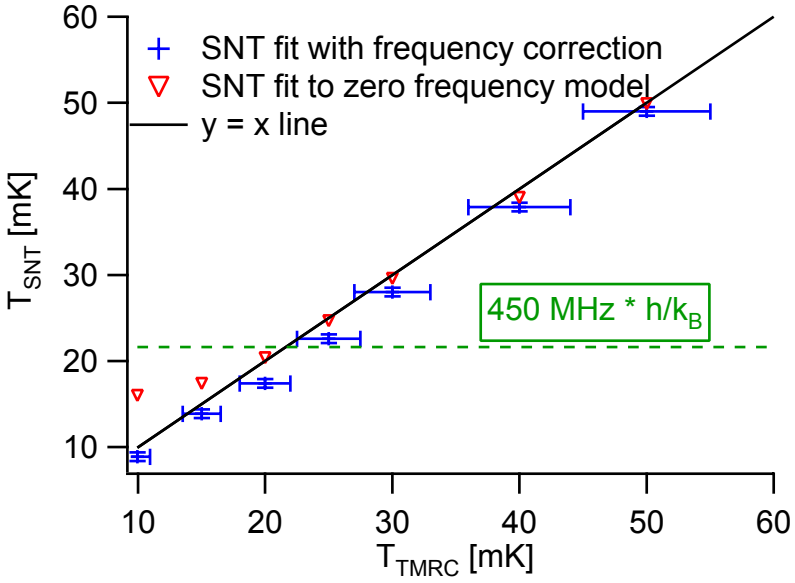

Figure 8.14: This data set shows another temperature comparison, where the secondary thermometer is the ruthenium oxide thermometer that was installed with the Cryoconcepts dilution refrigerator. Blue cross markers show the SNT temperature as determined by a correct fit to the finite frequency form of the noise. Red triangular markers show a naive fit to the zero frequency form of the noise. Note that the zero frequency fit diverges from the correct temperature as the temperature becomes lower than the quantum crossover temperature, shown by a horizontal dotted green line.

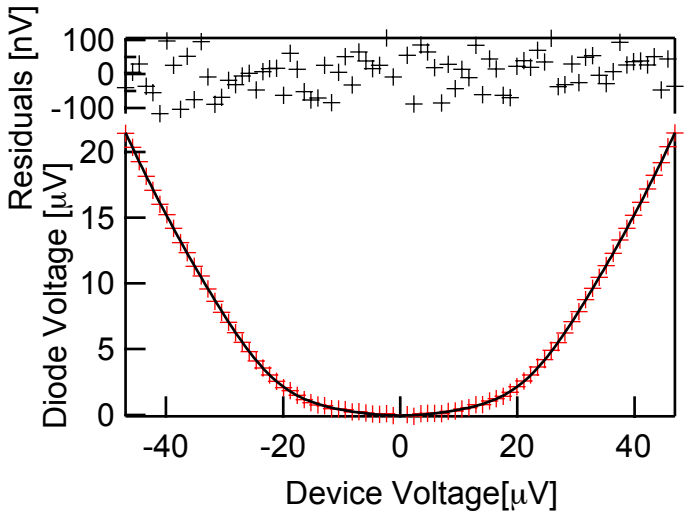

Figure 8.15: Noise from a junction at 29 mK irradiated with microwaves of frequency 5.3 GHz and normalized amplitude α=2.08. The black line shows a fit to the function given in the text.

in the case of an irradiated junction becomes

$$S_I(V,T) = \frac{1}{R}\sum_{\pm}\sum_{n=0}^{\infty} J_n^2(\alpha)\left[(eV \pm nhf)\coth\left(\frac{eV \pm nhf}{2k_BT}\right)\right], \tag{8.4}$$

where J_N^2 is the square of a Bessel function of the first kind, and $\alpha = eV_{ac}/hf$, where V_{ac} is the voltage amplitude of the irradiating signal across the junction.

Although in principle the RF apparatus has been designed to minimize out of band signals getting down to the device, when enough power is put at the "RF in" port it is possible to get a signal onto the device. I irradiated a SNT junction with a sinusoidal tone at a frequency of 5.3 GHz and measured its noise power as a function of voltage. Figure 8.15 shows a plot of such data with a fit to the above function. The dimensionless parameter α is found from the fit to be 2.08, which translates to about 45 μV amplitude across the junction. This effect could be very useful for determining the exact voltage across the junction, since it relates the voltage across the junction to a known frequency.

8.5 Experimental Studies of Systematic Effects

The impedance of a tunnel junction depends on voltage, and the coupling of the noise signal from the junction to the RF circuitry depends on that impedance. Therefore, the coupling changes with voltage. Also, the nonlinearity of the current and changing resistance leads to the shot noise $2eV/R$

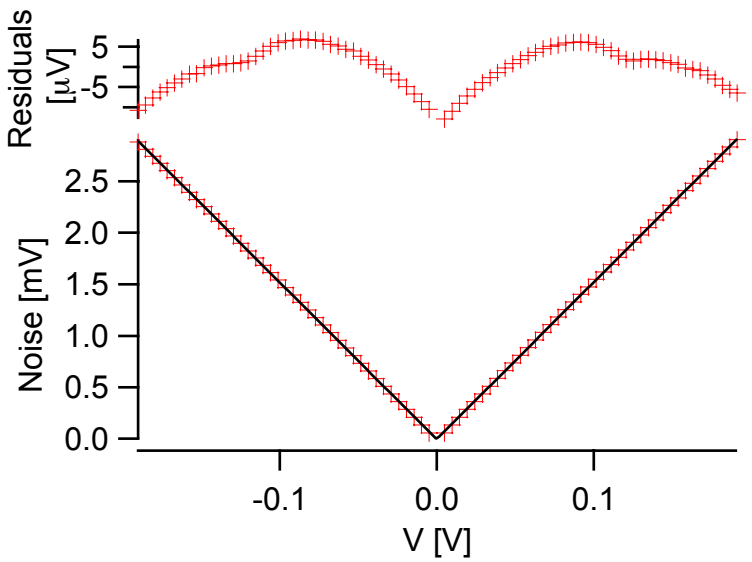

Figure 8.16: Noise from an SNT junction as a function of voltage over a very large range in voltage, but with temperature at approximately 4 K. This shows dramatically the nonlinear effects in the noise and the RF coupling that make high temperature SNT measurements complicated.

to be replaced by $2eI(V)$ and the noise power measured is proportional to $I(V)R(V)^2$. The overall effect of these nonlinearities can be seen in Figure 8.16, which shows the noise over a large bias range at a relatively low temperature. For the purposes of shot noise, temperature is effectively zero for these data, and the curvature from the junction's changing conductance properties can clearly be seen. One possibility might be that some of this curvature is the result of the nonlinearity of the Rf measurement chain. This possibility is ruled out, at least as a dominant effect, by the fact that changing the attenuation before the amplifier chain does not change the shape or relative size of the curvature.

The easiest way to measure the effect of changing RF coupling is with a RF reflected power measurement, done by sending a signal in through the "RF in" port at the top of the cryostat, as shown in Figure 7.5., and measuring how much of that signal comes out at the "RF out" port at the top of the cryostat. Since they are separate ports, a S_{21} measurement on a vector network analyzer is carried out, although it is really the reflected power that is being measured. Figure 8.17 shows traces from a network analyzer measurement of reflected power as a function of frequency for two different DC voltage applied to the device. It is difficult to see how the curves differ, but their difference is displayed below the traces, and it shows the trends quite clearly. The important

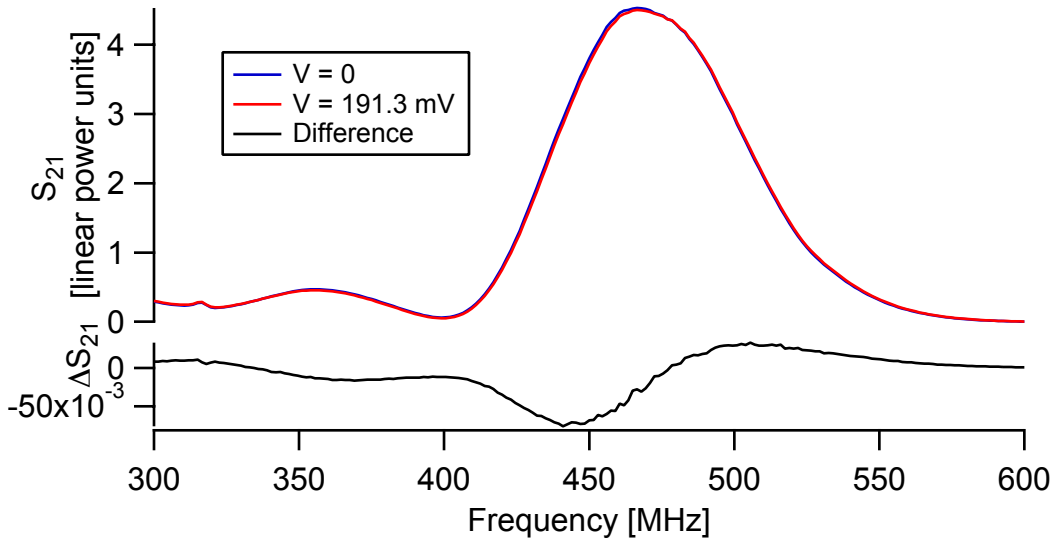

Figure 8.17: Reflected power from an SNT junction at 5.2 K as a function of voltage and frequency. The blue and red curves displayed above correspond to zero voltage and 191.3 mV, respectively, and the black curve below shows the difference between the curves. Note that at some frequencies the difference is positive and at some frequencies it is negative.

thing to notice is that while the reflected power is certainly dependent on voltage, the sign of the dependence changes with frequency. Thus, for some frequencies, finite voltage bias leads to better coupling, for some it leads to worse, and presumably for a careful choice of frequency it leads to no change or almost no change. Also, it is important to note the rate of change of the voltage dependence of reflected power with respect to frequency. If this rate of change is to high, it will be impossible to choose a band in which the behavior of the coupling is constant in frequency with enough bandwidth to have tolerable integration times. This rate of change is set by the physical distance between the device and the circulator, which should be kept as short as possible. If the circulator is at room temperature, for instance, the distance from the device to the circulator can be as long as 2 meters, making oscillations in the S curves with a period of 50 MHz.

By fixing frequency on the network analyzer and stepping the bias voltage on the device, it is possible to record the reflected power as a function of voltage at different frequencies to attempt to find optimal frequencies at which the change in coupling as a function of voltage is a minimum. Figure 8.18 shows such curves at several frequencies. Notice that in some cases the coupling increases, in some cases it decreases, and at 511 MHz it is roughly constant. How can the coupling remain constant when the impedance of the device is changing? Figure 8.19 has the answer. The reflected

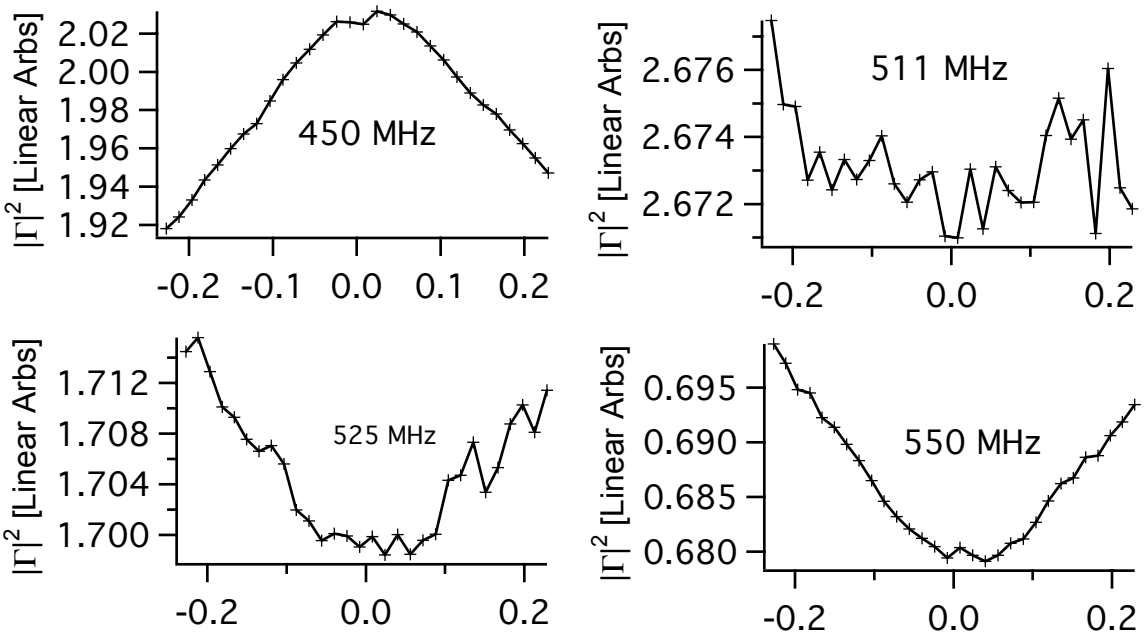

Figure 8.18: Reflected power from an SNT junction at 5.2 K as a function of voltage at different frequencies. These plots are the same type of data as shown in Figure 8.17, but sliced along a different axis. Note that for some frequencies, increasing voltage increases the coupling, and for some it decreases the coupling, while there are still others for which the magnitude appears to be approximately constant.

power does change, but at 511 MHz its amplitude remains constant while its phase changes. The data displayed in Figure 8.19 are over the same voltage ranges as the plots in Figure 8.18, and are compared against a circle centered at the origin. Since all the points lie along a circle, the magnitude of the reflected power remains constant as a function of voltage. For determining the amount of power that is coupled into the RF measurement chain, only this magnitude is important, so when the measurement is centered around a special frequency like 511 MHz, it should be possible to eliminate the effect of the changing junction impedance on the noise coupling.

8.6 DC Measurements

In addition to all the RF noise measurements, it was necessary to measure the DC characteristics of the junctions used. This was generally done simultaneously with the RF measurements, by recording the current at the same time as the voltage and noise power. By averaging many curves, sufficient signal to noise ratio was achieved to detect the relevant physical phenomena. Numerical derivatives

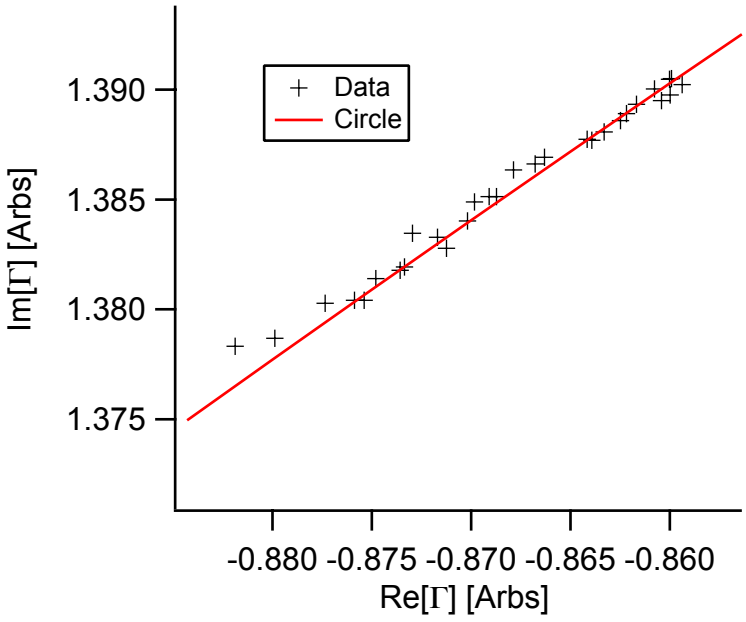

Figure 8.19: Comparison of 511 MHz data to a circle centered at the origin. This demonstrates how the changing impedance can change the phase but not the amplitude of the coupling.

were taken of the current with respect to voltage to get the conductance, from which resistance was found by taking the reciprocal. Also, the second derivative of current was computed numerically to measure the density of states and to see the IETS(inelastic electron tunneling spectroscopy) peaks described in Chapter 2.

Figure 8.20 shows resistance data taken over a range of temperatures for a typical SNT junction. Prominent features are that, overall, the conductance increases with voltage, that the IETS peaks manifest themselves as kinks in the resistance data, the zero bias anomaly and the fact that the overall conductance goes up with temperature, particularly at higher temperatures. All of these phenomena were discussed in Chapter 2. This last property, the overall change in resistance with temperature has been used as a secondary thermometer by Nanoway as a supplement to the coulomb blockade thermometer primary mode. That overall change in resistance has no effect on the operation of the SNT, however. Only voltage dependent effects affect the operation of the SNT.

Figure 8.21 shows the second derivative of current with respect to voltage, which both shows the zero bias anomaly form another perspective and shows the IETS peaks. These peaks are exactly where the OH bending modes are in energy, according to the IETS literature. The lack of other

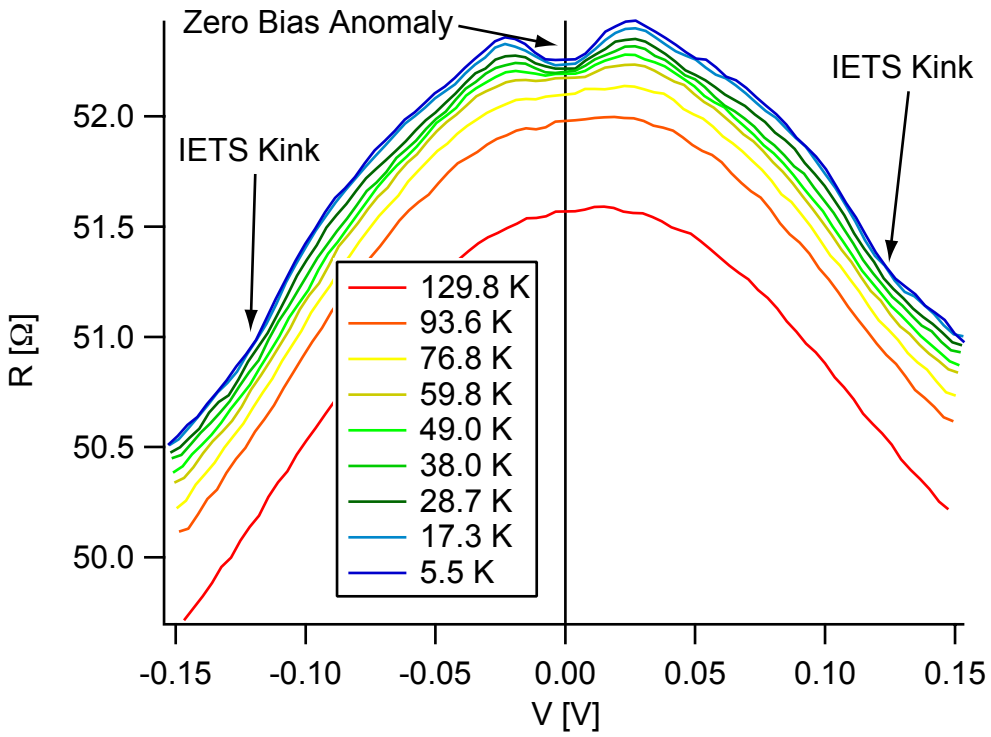

Figure 8.20: Differential resistance as a function of voltage at a range of temperatures, with important features indicated.

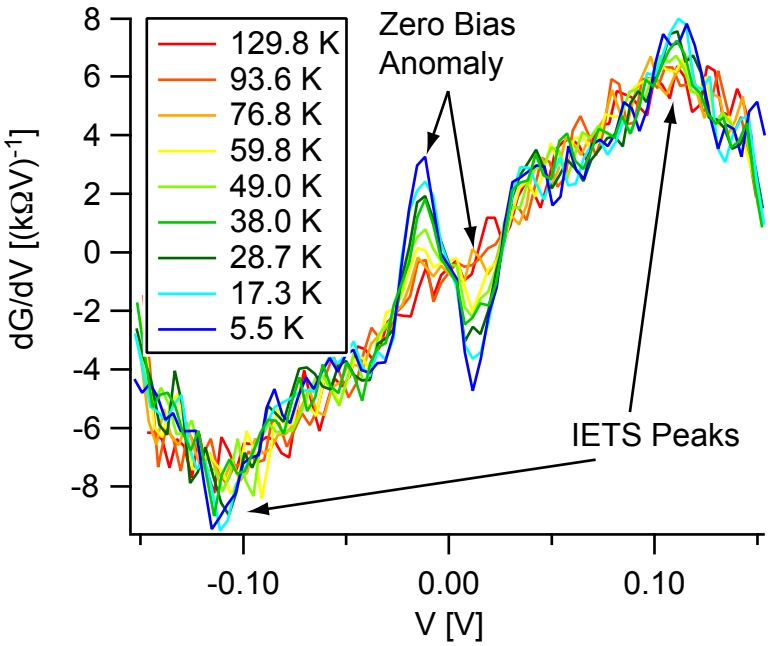

Figure 8.21: Derivative of differential conductance with respect to voltage. This shows the IETS peaks more clearly than the resistance data, and shows the zero bias anomaly form a different perspective.

IETS peaks indicates the lack of hydrocarbon contamination in the junction. A junction which has been contaminated with pump oil would have more peaks.

In addition to the measurements carried out on standard SNT junctions, I measured the DC characteristics of a manganese doped junction fabricated by Steven Ruggierro et al. [64] which does not show any signs of superconductivity, even at the 10 mK base temperature of the Cryoconcepts dilution refrigerator. Figure 8.22 shows the data from those measurements. These plots show both that there was no sign of superconductivity and that the resistance behavior was similar to that of the un-doped aluminum junctions I measured. In the future, it would be useful to use these for all SNT measurements in order to remove the need for a magnetic field at low temperatures.

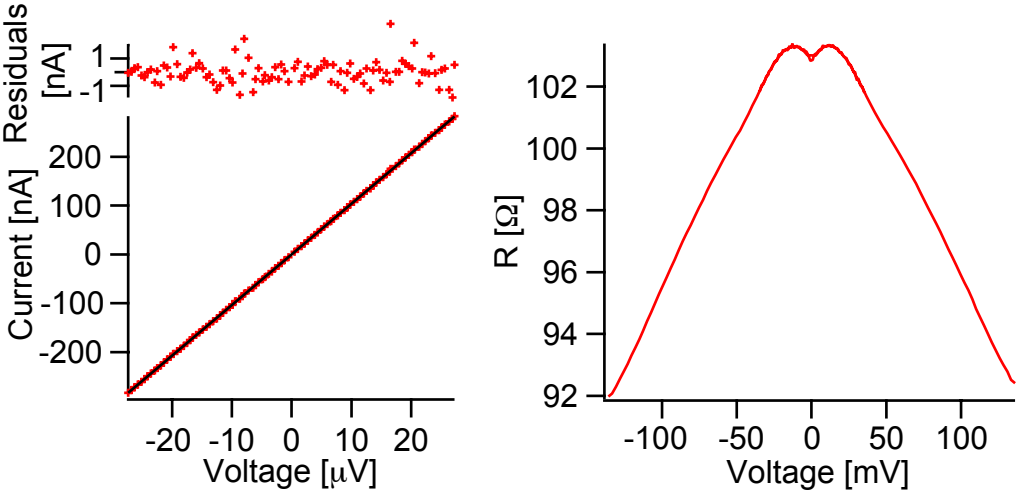

Figure 8.22: Current versus voltage and resistance measurements of a normal-insulator-normal junction at 10 mK.

Chapter 9

Applications

9.1 General Cryogenic Thermometry

The most near term application of the SNT is for general use as a cryogenic thermometer, particularly in dilution refrigerator systems. The SNT can read out temperature from below 10 mK up through room temperature. Although the accuracy is limited at room temperature, that is generally not critical for practical thermometry in a cryogenic system: as long as the thermometer tells the user when they are at around room temperature, around 77 K, and reads accurately below 4 K, having a range that extends to below 10 mK is excellent. With the optical lithography process described in Chapter 6, it is possible to create many hundreds or even thousands of devices in a day of fabrication, making the effective cost of each device very small. Also, given the large size of these junctions relative to typical single electron transistor junctions, they tend to be much more robust than the smaller tunnel junctions and so it is very practical to make large numbers of them and distribute them to people in the low temperature physics community as needed.

The room temperature electronics needed to read out the SNT is extremely simple, and could be easily incorporated into a small box for probably less than a thousand dollars worth of electronics. This box would consist of a chain of RF amplifiers, a diode detector, a digital to analog converter for the current bias, pair of analog to digital converters for measuring voltage and noise power, and a microcontroller to control the measurement. The code for the microcontroller would be very simple if the three point data taking method described in Chapter 8 were used and if temperature were extracted from a look-up table based on ratios of RF powers, which I have demonstrated using LabView code. The sample holder could be small and simple, as shown in Figure 7.2, which could be readily mass-produced and easily installed in cryostats. The tapeworm filter described in

Chapter 7 could either be mass produced or replaced with some other mass-producable filter. The main difficulties are finding a good first stage RF amplifier, of the possible need for a circulator, and installing RF lines in the cryostat of an experimenter who is not necessarily an RF expert and does not normally work with RF lines. The problem of the amplifier and the circulator are simply ones of cost. To get the low noise temperatures needed to have acceptable integration times at low temperatures, one needs high quality cryogenic amplifiers, which can be between 2,000 and 10,000 dollars. Circulators can also be as much as 2,000 dollars. The problem of installing RF lines in a dilution refrigerator would be solved if the SNT were pre packaged with new cryostat systems by the manufacturers, removing the need for the user to work with RF lines. In summary, the SNT is a very practical technology that could be deployed effectively in a variety of cryostat systems.

9.2 Temperature Metrology

Temperature metrology is another application the SNT could be useful for. While it has yet to demonstrate competitive accuracy in the range of the ITS-90, solutions to existing systematic effects should improve the accuracy into a competitive range, and the SNT may already be competitive in the range of the PLTS-2000. In the range from 10 mK to 100 mK, even accuracies of a few tenths of a percent, which have already been achieved with the SNT at higher temperatures, would be sufficient to provide a useful verification of the thermodynamic temperature of the PLTS-2000. Ultimately, if the SNT is able to successfully measure thermodynamic temperature to an absolute accuracy of 0.1 % over the whole range of the PLTS-2000 it might prove to be an attractive replacement for the melting pressure thermometer and superconducting fixed points because of its ease of use and because it measures thermodynamic temperature directly. If the SNT could ever be improved to the 1-2 ppm level, it would provide a method of measuring the Boltzmann constant independently of the gas constant R by performing the SNT measurement at the triple point of water, where the temperature is fixed by definition.

9.3 Amplifier Characterization

While temperature is usually the variable of interest in a SNT measurement, the gain and noise temperature of the RF measurement chain are also extracted as fit parameters, and can be useful for characterizing low noise amplifiers. The way this is done for amplifier characterization is that

bias voltage is stepped to three voltages, as with the rapid temperature readout described above, and noise data are recorded on a spectrum analyzer instead of in a broadband diode. Spectrum analyzer traces are then downloaded to a computer, which can quickly calculate and display the gain and noise temperature as a function of frequency. Alternatively, if frequency dependence is not as important as speed, the noise may be read out with a diode as usual, and displayed on an oscilloscope in xy mode as a function of voltage. What makes the SNT so useful for this application is that both gain and noise temperature can be measured in real time at any given temperature, making it possible to tune amplifier parameters and observe their effect on gain and noise temperature also in real time. This procedure may be repeated automatically at a series of temperatures, allowing for an amplifier to be totally characterized as a function of both frequency and temperature very rapidly.

9.4 Student Teaching Lab

Because of its reliance on elementary physics and its use of very basic lab equipment, the SNT could be very useful as a teaching lab or classroom demonstration. The subjects that could be taught or demonstrated with the SNT include the Fermi distribution in metals, shot noise, tunneling, temperature metrology and the concept of thermodynamic temperature measurement, RF measurement techniques, and cryogenics. As a classroom demonstration, it could be useful to be able to show students how the width of the Fermi function relates to temperature by showing the SNT curve on the oscilloscope at different temperatures and showing how the curve gets sharper at lower temperatures. The more hands-on aspects of setting up and operating the RF electronics could be useful for a radio astronomy lab course, since it would introduce students to low noise RF measurement, and to many of the measurement concepts that are useful in radio astronomy.

9.5 Calibrated Variable Noise Source for Radio Astronomy

Finally, it is possible that the SNT could be useful as a calibrated variable noise source. If the SNT junction is placed at a known temperature (the temperature could be determined with the SNT also), then noise power equivalent to many times the Johnson noise at that temperature can be accurately produced simply by applying voltage to the junction. Shot noise has been used as a calibrated noise source for a long time, however, the SNT could provide a shot noise source that could be calibrated in situ, which could be useful for space-based applications. One problem with

this idea, however, is that the natural RC time of the junction limits its bandwidth as a source to below a few tens of GHz. This rules out its use for most microwave background studies. Also, this idea requires that the coupling between the junction and the rest of the RF circuit is well calibrated, which could be difficult. Still, its potential simplicity as a solution if the right problem should arise makes this application worth mentioning.

Chapter 10

Conclusions

10.1 Future Work

There is quite a bit of work that still needs to be done on the SNT before it becomes mature technology, and there are several scientific research directions that could be of fundamental interest.

The work that remains to be done to make the SNT into practical thermometry for general use in cryostat systems is simply engineering, and is relatively straightforward. The sample holder and chip could be designed better, preferably replacing the wire bond with bump bonds that are easier to make quickly and reliably, the sample holder should be made hermetic and sealed with an overpressure of inert gas, as is the case with various resistance thermometer capsules. A single box could be constructed that would incorporate all the room temperature electronics, and the filtering could be improved to make construction easier to mass produce. All of this could be done easily by a properly motivated individual or company, and this project would prove to be very useful to the low temperature physics community.

In order for the SNT to become relevant to temperature metrology, it must be compared against temperature standards in the PLTS-2000 range and the accuracy must be improved in the higher temperature ranges. Because the United States is no longer involved in temperature metrology below the lower limit of the ITS-90 (0.65 K), this means that comparisons must be carried out in one of the few countries that does support such work. This means a comparison at NPL in the United Kingdom, BNM in France, PTB in Germany, or MIKES in Finland, or possibly some other national metrology lab. Several people from European labs have expressed interest in such a comparison, and I hope to be able to assist in that in the future, while I am a NIST employee. The improvement of the high temperature accuracy of the SNT is a much more difficult, but by no means impossible

task. The coupling between the junction and the RF measurement apparatus should be improved and the distance between the junction and the circulator should be reduced to as short as possible to simplify the problem of RF reflections. The theoretical questions about how nonlinear current affects shot noise will have to be conclusively and accurately answered, including in the regime where inelastic tunneling events are taking place. Answering these fundamental questions about the noise properties of inelastic tunneling events could lead to fundamentally interesting physics. Although noise of inelastic tunneling processes has been studied in other systems, trying to push the precision and accuracy down to the part per million level will almost certainly bring noise physics to light that would not otherwise have been observable in more typical noise measurements.

Finally, all of this work, from practical thermometry to temperature metrology over all temperature ranges to fundamental physics investigations and educational demonstrations would benefit from the SNT becoming a commercially available product. As a graduate student, I have not had the time or inclination to bring the SNT into the marketplace, but it is very likely worth doing, and is the subject of the following section.

10.2 Commercialization

Who would buy the SNT, and is it competitive with existing commercial products? The niche markets for the SNT are in cryostat systems that operate below one kelvin and in situations where it is important to have a primary thermometer. In the range where the platinum resistance thermometer can be used, the SNT is not competitive except as a primary thermometer, since the platinum thermometer is accurate, reliable, cheap, and easy to use. It is possible that the SNT could be relevant in the platinum range in aerospace applications, since having a self-calibrating thermometer could be very useful in space-based systems. There might also be a market for the SNT as a classroom demonstration or teaching lab. By far the majority of the market is for cryostats, however, and by far the best way to sell them would be to pre-package them with new cryostats when they are sold. Thus the size of the potential market is equivalent to the size of the market for dilution refrigerators and pumped helium-3 refrigerators. If the number of such systems sold worldwide is approximately 100, and each SNT system could be sold for several thousand dollars, the potential yearly market for the SNT could be several hundred thousand dollars, which might be worthwhile for a small company. The only company presently selling primary thermometers in this market is NanoWay Oy, the Finnish company that sells the Coulomb blockade thermometer described in Chapter 1. With the

advent of the cryogen-free dilution refrigerator and the development of industrially useful cryogenic detector, the cost of cryogenic systems could drop and the number sold could grow exponentially, drastically increasing the demand for good cryogenic thermometry.

10.3 Conclusions

In this thesis I have demonstrated that the SNT is both a practical thermometer for cryogenic systems and a potentially useful tool for temperature metrology. In conclusion, I will summarize the relative sizes of the most relevant systematic effects or corrections on the temperature measured by the SNT. This comparison is shown in Table 10.1. These effects are also discussed in Chapter 4, and a comparison at different temperatures is presented in Figure 4.1. Right now, the highest accuracy comparisons showed a deviation from the ITS-90 calibrated thermometer of approximately 0.4 %, which is the dominant source of error. This error is not fundamental, however, and should be able to be eliminated by improving device design with a trilayer design, thicker films, and a more careful choice of geometry. The next largest systematic effect is the changing impedance of the tunnel junction. This is presently estimated roughly to be 3×10^{-4} for 15 K, and much smaller at lower temperatures, but as large as 10 % for room temperature. This is also not a fundamental limitation, and in principle with further experimental work could both be brought to unmeasurable levels by selecting the right frequency band for measurements and corrected for using the theory discussed in Chapter 4. The effects of finite frequency are well-understood, and may be corrected for accurately without difficulty. Heating has not yet appeared as a distinguishable effect, and future experimentalists will need to both look for evidence of it in the data, and keep improving theoretical estimates based on new junction designs.

Based on the work described here, improvement of junction design should bring temperature errors into the range of hundreds of ppm, and further study of RF coupling corrections should be able to improve beyond that into the range of tens of ppm or single ppm, depending on whether unexpected physical phenomena limit uncertainty. These projected uncertainties make the SNT relevant for temperature metrology in the range of the PLTS-2000, and very likely in the range of the ITS-90. If corrections to the single ppm level at 273.16 K could be achieved, the SNT could also be relevant for a determination of the ratio e/k_B.

Table 10.1: Table of estimates of present sizes of various systematic effects and corrections, along with possible future improvements.

Systematic Effect or Correction	Present Work	Future Improvements
Statistics	5 mK/$\sqrt{\text{Hz}}$	0.05 mK/$\sqrt{\text{Hz}}$ with SQUIDs
DC voltage drops	0.4 %	Could improve with design
Frequency corrections	$\approx \frac{1}{12}\left(\frac{hf}{k_B T}\right)^2$	Correction already exact
Changing junction impedance	$\pm$ 3×10^{-4} to 10 %	Could be possible to Correct to Arbitrary Accuracy
Linearity of RF chain	<5×10^{-4}	Can be arbitrarily improved
Heating	Not yet observed	Unknown
Unknown deviations of noise from Theory	Not yet observed	Verify experimentally as other effects improve
Variable Substrate Leakage	$<$ 1 ppm	$<$ 1 ppm

Chapter 11

Fabrication Appendix

11.1 Electron Beam Lithography Process

This process is done on a single chip, typically 1cm on a side.

60 seconds sonicate in NMP

60 seconds sonicate in acetone

60 seconds sonicate in methanol

rinse in running DI water

blow off with dry nitrogen

bake on hotplate at 180 C for two minutes

cool on copper block for 2 minutes

spin on LOR 5A resist 1000 rpm 40 s

bake at 180 C for 2 minutes with a glass cover over the chip

on the hotplate

cool on copper plate for two minutes

spin 950k A6 PMMA at 1500 rpm for 40s

bake at 180 C for 10 minutes with cover

cool on copper block for two minutes

write e-beam pattern using NPGS on a JEOL 6400 SEM with the beam set to 40 kV and 12 pA.

small features: 400 $\mu C/cm^2$ area dose

large features: 30 nC/cm line dose

develop:

90 seconds MIBK:IPA 1:1

30 seconds IPA

45 seconds LDD26W developer

15 seconds DI

rinse in running DI

blow off with dry nitrogen

deposit aluminum in Varian:

aluminum pellets in tungsten boats(not alumina coated!)

pump to about 2×10^{-6} torr,

tilt to ±45 degrees

evaporate at 10 angstroms/second,

500 mTorr of oxygen from cleanroom oxygen line for 10 minutes

second evaporation: 8×10^{-7} torr

50 nm thickness each film.

liftoff:

60 C nanoremover, squirting with syringe for 30-60 minutes

11.2 Optical Lithography Process

60 seconds sonicate in acetone

60 seconds sonicate in methanol

rinse in running DI water

blow off with dry nitrogen

bake on hotplate for 2 minutes at 180 C

spin on LOR20B lift off resist at 3000 rpm for 45 seconds

bake on hotplate for 2 minutes at 150 C

spin on S1813 at 3000 rpm for 45 seconds

bake on hotplate for 1 minute at 115 C

expose for 27 seconds on hard contact mask HTG mask aligner, with 6.3 mW/cm^2 of power at 405 nm

develop for 1 minute and 45 seconds in a 2 to 1 solution of DI to MF312 developer

deposit 80 nm Al, +34 degrees at 1 nm/s

Chapter 12

Junction Noise Derivation Appendix

In Chapter 1, the noise power from a tunnel junction is shown to be proportional to the integral

$$\int_{-\infty}^{\infty} [f(E-eV)(1-f(E)) + f(E)(1-f(E-eV))]dE. \tag{12.1}$$

In this Appendix, I will show how this factor leads to the expression $eV\coth eV/2k_BT$. By recalling the property of the Fermi function that 1-f(E)=f(-E), this is re-written as

$$\int_{-\infty}^{\infty} [f(E-eV)f(-E) + f(E)f(eV-E)]dE. \tag{12.2}$$

Substituting in the values of the Fermi functions, this leads to

$$\int_{-\infty}^{\infty} \left[\frac{1}{(e^{(E-eV)/k_BT}+1)}\frac{1}{(e^{(-E)/k_BT}+1)} + \frac{1}{(e^{(E)/k_BT}+1)}\frac{1}{(e^{(eV-E)/k_BT}+1)}\right] dE. \tag{12.3}$$

Now, I define $y = e^{E/k_BT}$, and substitute y is to get

$$\int_{-\infty}^{\infty} \left[\frac{1}{ye^{-eV/k_BT}+1}\frac{1}{\frac{1}{y}+1} + \frac{1}{\frac{1}{y}e^{eV/k_BT}+1}\frac{1}{y+1}\right] dE, \tag{12.4}$$

which simplifies to

$$(1+e^{-eV/k_BT})\int_{-\infty}^{\infty} \left[\frac{y}{(ye^{-eV/k_BT}+1)(y+1)}\right] dE. \tag{12.5}$$

The integrand may now be simplified using the method of partial fractions as follows:

$$\frac{y}{(ye^{-eV/k_BT}+1)(y+1)} = \frac{A}{y+1} + \frac{B}{ye^{-eV/k_BT}+1}, \tag{12.6}$$

from which A and B are found to be

$$A = \frac{1}{e^{-eV/k_BT}-1} = -B. \tag{12.7}$$

Thus, the total expression may be re-written as

$$\frac{1+e^{-eV/k_BT}}{e^{-eV/k_BT}-1}\int_{-\infty}^{\infty}\left[\frac{1}{y+1}-\frac{1}{ye^{-eV/k_BT}+1}\right]dE, \tag{12.8}$$

or, substituting back in the definition of y and multiplying the pre-factor by $e^{eV/2k_BT}$,

$$\coth\left(\frac{eV}{2k_BT}\right)\int_{-\infty}^{\infty}\left[\frac{1}{e^{(E-eV)/k_BT}+1}-\frac{1}{e^{E/k_BT}+1}\right]dE. \tag{12.9}$$

Now, I note that the Fermi function may be re-written as follows:

$$\frac{1}{e^{E/k_BT}+1}=\frac{1}{2}\left(1-\tanh\left(\frac{E}{2k_BT}\right)\right). \tag{12.10}$$

Thus, the above integral may be written in terms of hyperbolic trigonometric functions as

$$\frac{1}{2}\coth\left(\frac{eV}{2k_BT}\right)\int_{-\infty}^{\infty}\left[\tanh\left(\frac{E}{2k_BT}\right)-\tanh\left(\frac{E-eV}{2k_BT}\right)\right]dE, \tag{12.11}$$

and since

$$\int\tanh(x)dx=\ln(\cosh(x)), \tag{12.12}$$

this is

$$-k_BT\coth\left(\frac{eV}{2k_BT}\right)\left[\ln\left(\frac{\cosh\left(\frac{E-eV}{2k_BT}\right)}{\cosh\left(\frac{E}{2k_BT}\right)}\right)\right]_{-\infty}^{\infty}. \tag{12.13}$$

Using the identity for the hyperbolic cosine of a sum, this may be reduced to

$$-k_BT\coth\left(\frac{eV}{2k_BT}\right)\left[\ln\left(\frac{\cosh\left(\frac{E}{2k_BT}\right)\cosh\left(\frac{eV}{2k_BT}\right)-\sinh\left(\frac{E}{2k_BT}\right)\sinh\left(\frac{eV}{2k_BT}\right)}{\cosh\left(\frac{E}{2k_BT}\right)}\right)\right]_{-\infty}^{\infty}, \tag{12.14}$$

which simplifies to

$$-k_BT\coth\left(\frac{eV}{2k_BT}\right)\left[\ln\left(\cosh\left(\frac{eV}{2k_BT}\right)-\tanh\left(\frac{E}{2k_BT}\right)\sinh\left(\frac{eV}{2k_BT}\right)\right)\right]_{-\infty}^{\infty}. \tag{12.15}$$

Now, finally, the limits for the hyperbolic tangent may be substituted into the equation to get

$$k_BT\coth\left(\frac{eV}{2k_BT}\right)\left[\ln\left(\frac{\cosh\left(\frac{eV}{2k_BT}\right)+\sinh\left(\frac{eV}{2k_BT}\right)}{\cosh\left(\frac{E}{2k_BT}\right)-\sinh\left(\frac{eV}{2k_BT}\right)}\right)\right], \tag{12.16}$$

which can be simplified by using the definitions of the hyperbolic sine and cosine to get

$$k_BT\coth\left(\frac{eV}{2k_BT}\right)\ln e^{eV/k_BT}=eV\coth\left(\frac{eV}{2k_BT}\right), \tag{12.17}$$

which is the desired result.

Bibliography

[1] Joel A. Appelbaum. Exchange model of zero-bias tunneling anomalies. *Physical Review*, 159:774–774, July 1967.

[2] Joel A. Appelbaum. Microscopic theory of tunneling anomalies. *Physical Review*, 160:554–561, August 1967.

[3] Philip Ball. Noise thermometer accurate at frigid extremes. *Nature*, 2003.

[4] Alan J. Bennett, C. B. Duke, and S. D. Silverstein. Theory of the tunneling spectroscopy of collective excitations. *Physical Review*, 176:969–992, December 1968.

[5] S.P. Benz, J.M. Martinis, P.D. Dresselhaus, and Sae Woo Nam. An ac josephson source for johnson noise thermometry. *IEEE Trans. Instrum. Meas. (USA)*, 52(2):545 – 9, 2003.

[6] S.P. Benz, J.M. Martinis, P.D. Dresselhaus, and S.W. Nam. An ac josephson source for johnson noise thermometry. *Conference Digest. 2002 Conference on Precision Electromagnetic Measurements (Cat. No.02CH37279)*, pages 436 – 7, 2002.

[7] Philip R. Bevington and D. Keith. *Data Reduction and Error Analysis for the Physical Sciences*. McGraw-Hill, 3rd edition, 2003.

[8] Ya.M. Blanter and M. Buttiker. Shot noise in mesoscopic conductors. *Phys. Rep. (Netherlands)*, 336(1-2):1 – 166, 2000.

[9] W.F. Brinkman, R.C. Dynes, and J.M. Rowell. Tunneling conductance of asymmetrical barriers. *J. Appl. Phys.*, 41(5):1915 – 21, 1970.

[10] Elias Burstein and Stig Lundqvist, editors. *Tunneling Phenomena in Solids*. Plenum Press, 1969.

[11] Herbert B. Callen and Theodore A. Welton. Irreversibility and generalized noise. *Physical Review*, 83(1):34–40, July 1951.

[12] Manfredo P. Do Carmo. *Differential Geometry of Curves and Surfaces*. Prentice-Hall, 1976.

[13] Kenneth Chang. Hot enough for you? scientists ask, fast enough for you? *New York Times*, July 8 2003.

[14] Adrian Cho Adrian Cho. A thermometer beyond compare? *Science*, 299:1641, 2003.

[15] M. J. M. de Jong and C. W. J. Beenakker. Shot noise in mesoscopic systems. *Arxiv preprint cond-mat/9611140*, 1996.

[16] M.H. Devoret, D. Esteve, H. Grabert, G.-L. Ingold, H. Pothier, and C. Urbina. Effect of the electromagnetic environment on the coulomb blockade in ultrasmall tunnel junctions. *Phys. Rev. Lett. (USA)*, 64(15):1824 – 7, 1990.

[17] Michel Devoret and Hermann Grabert, editors. *Single Charge Tunneling*. Plenum Press, 1991.

[18] R. H. Dicke. The measurement of thermal radiation at microwave frequencies. *Review of Scientific Instruments*, 17(7):268–275, July 1946.

[19] C.B. Duke, S.D. Silverstein, and A.J. Bennett. Zero-bias tunnel-conductance minima due to the excitation of collective modes in the barrier. *Physical Review Letters*, 19(6):315 – 318, 1967.

[20] L. Esaki. Long journey into tunneling. *Proc. IEEE*, 62(6):825 – 31, 1974. historical background;quantum theory;tunnel diode;negative resistance;periodic structures;resonant transmission;metal oxide semiconductor structures;tunnelling;review;.

[21] J.C. Fisher and I. Giaever. Tunneling through thin insulating layers. *Journal of Applied Physics*, 32(2):172 – 177, 1961.

[22] R.H. Fowler and L. Nordheim. Electron emission in intense electric fields. *Proceedings of the Royal Society of London*, 119:173 – 181, 1928.

[23] J. Frenkel. Electrical resistance of contacts between solid conductors. *Physical Review*, 36:1604 – 1618, 1930.

[24] T.A. Fulton and G.J. Dolan. Observation of single-electron charging effects in small tunnel junctions. *Phys. Rev. Lett. (USA)*, 59(1):109 – 12, 1987.

[25] G. Gamow. Quantum theory of the atomic nucleus. *Zeitschrift fur Physik*, 51(3-4):204 – 212, 1928.

[26] Dolan G.J. Offset masks for lift-off photoprocessing. *Applied Physics Letters*, 31(5):337–339, 1977.

[27] Sarah Graham. Thermometer reads temperature from noise. *Scientific American*, 2003.

[28] Preston-Thomas H, Bloembergen P, and Quinn T J. Supplementary information for the international temperature scale of 1990. Technical report, BIPM, 1990.

[29] R. Holm. The electric tunnel effect across thin insulator films in contacts. *Journal of Applied Physics*, 22:569 – 574, 1951.

[30] M. Imamura and A. Ohte. A new method of noise thermometry. In *Temperature: Its Measurement and Control in Science and Industry*, volume 5, pages 139–142, 1982.

[31] R.C. Jaklevic and J. Lambe. Molecular vibration spectra by electron tunneling. *Physical Review Letters*, 17(22):1139 – 1140, 1966.

[32] Marc Johan Martijn De Jong. *Shot Noise and Electrical Conduction in Mesoscopic Systems*. PhD thesis, Leiden University, 1995.

[33] B.D. Josephson. Possible new effects in superconductive tunnelling. *Physics Letters*, 1(7):251 – 253, 1962.

[34] B.D. Josephson. The discovery of tunnelling supercurrents. *Rev. Mod. Phys. (USA)*, 46(2):251 – 4, 1974.

[35] R.A. Kamper and J.E. Zimmerman. Noise thermometry with the josephson effect. *J. Appl. Phys. (USA)*, 42(1):132 – 6, 1971.

[36] J. P. Kauppinen, K. T. Loberg, A. J. Manninen, J. P. Pekola, and R. A. Voutilainen. Coulomb blockade thermometer: Tests and instrumentation. *Review of Scientific Instruments*, 69:4166–4175, 1998.

[37] J.P. Kauppinen and J.P. Pekola. Electron-phonon heat transport in arrays of al islands with submicrometer-sized tunnel junctions. *Phys. Rev. B*, 54(12):8353 – 6, 1996.

[38] S. K. Khanna and John Lambe. Inelastic electron tunneling spectroscopy. *Science*, 220(4604):1345–1351, June 1983.

[39] J. Lambe and R.C. Jaklevic. Molecular vibration spectra by inelastic electron tunneling. *Physical Review*, 165(3):821 – 832, 1968.

[40] R. Landauer. Spatial variation of currents and fields due to localized scatterers in metallic conduction. *IBM Journal of Research and Development*, 1(3):223 – 231, 1957.

[41] A.J. Manninen, J.P. Kauppinen, S. Farhangfar, L.J.T. Taskinen, and J.P. Pekola. Feasibility of coulomb blockade thermometry in metrology. *Physica B (Netherlands)*, 284-288:2010 – 11, 2000.

[42] Eugen Merzbacher. *Quantum Mechanics*. John Wiley and Sons, Inc., 1961.

[43] Ian M. Mills, Peter J. Mohr, Terry J. Quinn, Barry N. Taylor, and Ian M.; Mohr Peter J.; Quinn Terry J.; Taylor Barry N.; Williams Edwin R. Williams, Edwin R. Mills. Redefinition of the kilogram: a decision whose time has come. *Metrologia*, 42:71–80, 2005.

[44] S. Nam, S. Benz, P. Dresselhaus, W.L. Tew, D.R. White, and J.M. Martinis. A new approach to johnson noise thermometry using a quantum voltage noise source for calibration. *Conference Digest. 2002 Conference on Precision Electromagnetic Measurements (Cat. No.02CH37279)*, pages 438 – 9, 2002.

[45] Sae Woo Nam, S.P. Benz, P.D. Dresselhaus, W.L. Tew, D.R. White, and J.M. Martinis. Johnson noise thermometry measurements using a quantized voltage noise source for calibration. *IEEE Trans. Instrum. Meas. (USA)*, 52(2):550 – 4, 2003.

[46] S.W. Nam, S.P. Benz, J.M. Martinis, P. Dresselhaus, W.L. Tew, and D.R. White. A ratiometric method for johnson noise thermometry using a quantized voltage noise source. *AIP Conf. Proc. (USA)*, 684(pt.1):37 – 42, 2003.

[47] J. Niemeyer. *PTB-Mitt*, 84:251, 1974.

[48] S. Oberholzer, E.V. Sukhorukov, and C. Schonenberger. Crossover between classical and quantum shot noise in chaotic cavities. *Nature*, 415(6873):765 – 7, 2002.

[49] S. Oberholzer, E.V. Sukhorukov, C. Strunk, C. Schonenberger, T. Heinzel, and M. Holland. Shot noise by quantum scattering in chaotic cavities. *Phys. Rev. Lett.*, 86(10):2114 – 17, 2001.

[50] A. Ohte and M. Imamura. Thermal noise thermometer. Technical report, U.S. Patent Number 4,099,413, 1978.

[51] Dewitt G. Ong. *Modern MOS Technology: Processes, Devices, and Design*. McGraw-Hill, 1984.

[52] J.R. Oppenheimer. Quantum theory of aperiodic effects. *Physical Review*, 31:66 – 81, 1928.

[53] J. P. Pekola, K. P. Hirvi, J. P. Kauppinen, and M. A. Paalanen. Thermometry by arrays of tunnel junctions. *Phys. Rev. Lett.*, 73:2903–2906, November 1994.

[54] J.P. Pekola, J.K. Suoknuuti, J.P. Kauppinen, M. Weiss, P. vd Linden, and A.G.M. Jansen. Coulomb blockade thermometry in the milli-kelvin temperature range in high magnetic fields. *J. Low Temp. Phys. (USA)*, 128(5-6):263 – 9, Sept. 2002.

[55] F. Pierre, H. Pothier, P. Jpyez, N.O. Birge, D. Esteve, and M.H. Devoret. Electrodynamic dip in the local density of states of a metallic wire. *Phys. Rev. Lett. (USA)*, 86(8):1590 – 3, 2001.

[56] David M. Pozar. *Microwave Engineering*. John Wiley and Sons, second edition, 2003.

[57] H Preston-Thomas. The international temperature scale of 1990 (its-90). *Metrologia*, 27:3–10, 1990.

[58] R.A. Pucel. The equivalent noise current of esaki diodes. *Proceedings of the Institute of Radio Engineers*, 49(6):1080 – 1081, 1961.

[59] Jr R. J. Soulen, W. E. Fogle, and J. H. Colwell. Measurements of absolute temperature below 0.75 k using a josephson-junction noise thermometer. *Journal of Low Temperature Physics*, 94(5/6):385–450, 1994.

[60] B. Reulet, J. Senzier, and D.E. Prober. Environmental effects in the third moment of voltage fluctuations in a tunnel junction. *Phys. Rev. Lett.*, 91:196601, 2003.

[61] B. Reulet, L. Spietz, C.M. Wilson, J. Senzier, and D.E. Prober. Measurement of non-gaussian shot noise: influence of the environment.

[62] D. Rogovin and D.J. Scalapino. Fluctuation phenomena in tunnel junctions. *Ann. Phys. (USA)*, 86(1):1 – 90, 1974.

[63] J.M. Rowell and L.Y.L. Shen. Zero-bias anomalies in normal metal tunnel junctions. *Physical Review Letters*, 17(1):15 – 19, 1966.

[64] S.T. Ruggiero, A. Williams, W.H. Rippard, A. Clark, S.W. Deiker, L.R. Vale, and J.N. Ullom. Dilute al-mn alloys for low-temperature device applications. *Journal of Low Temperature Physics*, 134(3-4):973–84, 2004.

[65] R. L. Rusby, M. Durieux, A. L. Reesink, R. P. Hudson, G. Schuster, W. E. Fogle M. Kühne, R. J. Soulen, and E. D. Adams. The provisional low temperature scale from 0.9 mk to 1 k, plts-2000. *Journal of Low Temperature Physics*, 126(1):633–642, 2002.

[66] R.J. Schoelkopf, P.J. Burke, A.A. Kozhevnikov, D.E. Prober, and M.J. Rooks. Frequency dependence of shot noise in a diffusive mesoscopic conductor. *Phys. Rev. Lett. (USA)*, 78(17):3370 – 3, 1997.

[67] R.J. Schoelkopf, A.A. Kozhevnikov, D.E. Prober, and M.J. Rooks. Observation of "photon-assisted" shot noise in a phase-coherent conductor. *Phys. Rev. Lett.*, 80(11):2437 – 40, 1998.

[68] W. Schottky. Electric oscillations. *Annalen der Physik*, 57(7):541 – 567, 1918.

[69] L.Y.L. Shen and J.M. Rowell. Magnetic field and temperature dependence of the "zero bias tunneling anomaly". *Solid State Communications*, 5(3):189 – 192, 1967.

[70] L.Y.L. Shen and J.M. Rowell. Zero-bias tunneling anomalies-temperature, voltage and magnetic field dependence. *Physical Review*, 165(2):566 – 577, 1968.

[71] J.G. Simmons. Generalized formula for the electric tunnel effect between similar electrodes separated by a thin insulating film. *Journal of Applied Physics*, 34(6):1793 – 1803, 1963.

[72] Lafe Spietz, K. W. Lehnert, I. Siddiqi, and R. J. Schoelkopf. Primary electronic thermometry using the shot noise of a tunnel junction. *Science*, 300:1929–1932, 2003.

[73] Brian C. Wadell. *Transmission Line Design Handbook*. Artech House Publishers, 1991.

[74] D.P. Woody, S. Padin, H. LeDuc, and J. Stern. On using the shot noise in sis tunnel junctions for characterizing if amplifiers. In *Sixth International Symposium on Space Terahertz Technology*, pages 140–149, 1995.

[75] A.F.G. Wyatt. Anomalous densities of states in normal tantalum and niobium. *Physical Review Letters*, 13(13):401 – 404, 28 Sept. 1964.